цена свободная
price – not fixed

индекс 80568
80568 Index

https://journals.vsu.ru/kcmf/about

ISSN 1606-867X
eISSN 2687-0711

КОНДЕНСИРОВАННЫЕ СРЕДЫ И МЕЖФАЗНЫЕ ГРАНИЦЫ

CONDENSED MATTER AND INTERPHASES

Том Vol. 22, № No. 4
2020

Научный журнал по проблемам конденсированного состояния
и физико-химическим процессам
на границах раздела фаз и в их объеме

The scientific journal “Kondensirovannye sredy i mezhfaznye granitsy”
(CONDENSED MATTER AND INTERPHASES)
is the leading scientific publication in Russia on key problems
of condensed matter and physico-chemical processes
at the interfaces and in the volume.

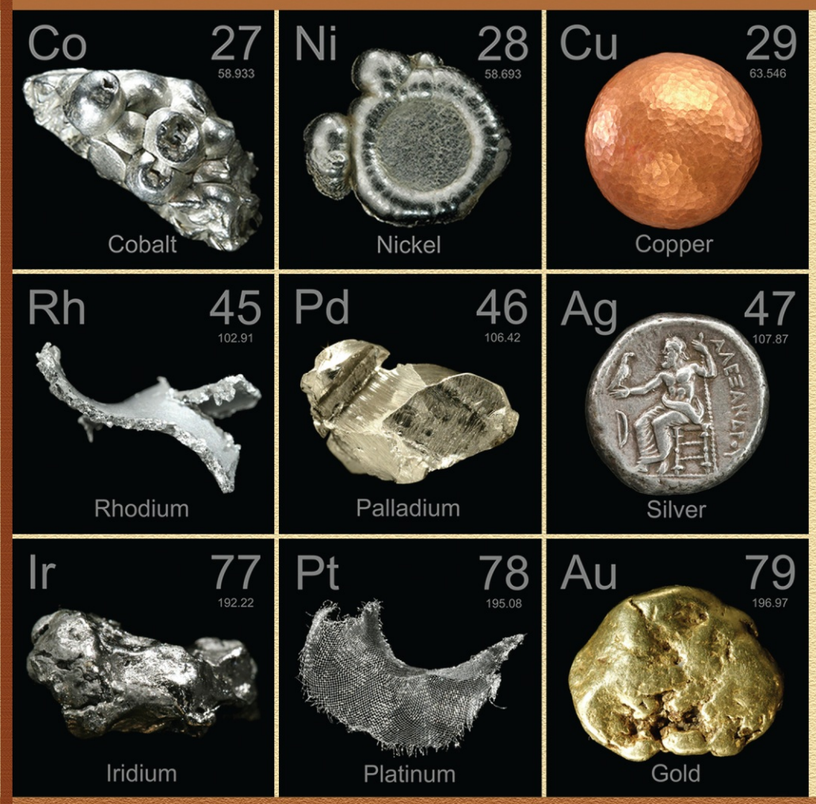

Condensed Matter and Interphases (Kondensirovannye sredy i mezhfaznye granitsy)

Peer-reviewed scientific journal
Issued 4 times a year

Volume 22, No. 4 (2020)

Full-text version is available in the Russian language
on the website: https://journals.vsu.ru/kcmf/about

ISSN 1606-867X
eISSN 2687-0711

FOUNDER AND PUBLISHER
Voronezh State University

The journal was founded in 1999 by Professor A. M. Khoviv, DSc in Chemistry, with the support of Kurnakov Institute of General and Inorganic Chemistry of the Russian Academy of Sciences

The journal is registered by the Russian Federal Supervision Service for Compliance with the Law in the Field of Mass Media and Cultural Heritage Protection, Certificate of Registration ПИ № ФС77-78771 date 20.07. 2020

The journal is included in the List of Leading Peer-reviewed Scientific Journals and Publications Recommended by the State Commission for Academic Degrees and Titles, where the main scientific results of dissertations for DSc and PhD degrees in Chemistry, Physics and Mathematics should be published. Specialities: 02.00.01 – Inorganic Chemistry, 02.00.04 – Physical Chemistry, 02.00.05 – Electrochemistry, 02.00.21 – Solid State Chemistry, 01.04.07 – Condensed Matter Physics

Indexed and archived by

the Russian Science Citation Index, RSCI, Scopus, Chemical Abstract, EBSCO, DOAJ, CrossRef

Editorial Board and Publisher Office
1 Universitetskaya pl., Voronezh 394018
Tel.: +7 (432) 2208445
https://journals.vsu.ru/kcmf/about
E-mail: kcmf@main.vsu.ru

Date of publication 25.12.2020

Price – not fixed

Subscription is available using the unified catalogue "Russian Press", subscription index 80568

CONTENTS

Condensed Matter and Interphases
(Kondensirovannye sredy i mezhfaznye granitsy)

Review

DOI: https://doi.org/10.17308/kcmf.2020.22/3113
Received 10 September 2020
Accepted 28 September 2020
Published online 25 December 2020

ISSN 1606-867X
eISSN 2687-0711

Modern Approaches to the Medical Use of pH- and Temperature-Sensitive Copolymer Hydrogels (Review)

© 2020 V. A. Kuznetsov[a, b], P. O. Kushchev✉[a, b, *] I. V. Ostankova[a, b], A. Yu. Pulver[a, c], N. A. Pulver[a, c], S. V. Pavlovich[a], R. A. Poltavtseva[a]

[a]*National Medical Research Center for Obstetrics, Gynecology, and Perinatology named after Academician V.I. Kulakov of the Ministry of Healthcare of the Russian Federation, ul. Academika Oparina 4, Moscow, 117997, Russian Federation*

[b]*Voronezh State University, 1 Universitetskaya pl., Voronezh, 394018, Russian Federation*

[c]*LLC Institute of Biology of Aging ul. Platonova 19, Voronezh, 394018, Russian Federation*

Abstract

This article provides the review of the medical use of pH- and temperature-sensitive polymer hydrogels. Such polymers are characterised by their thermal and pH sensitivity in aqueous solutions at the functioning temperature of living organisms and can react to the slightest changes in environmental conditions. Due to these properties, they are called stimuli-sensitive polymers. This response to an external stimulus occurs due to the amphiphilicity (diphilicity) of these (co)polymers. The term hydrogels includes several concepts of macrogels and microgels. Microgels, unlike macrogels, are polymer particles dispersed in a liquid and are nano- or micro-objects. The review presents studies reflecting the main methods of obtaining such polymeric materials, including precipitation polymerisation, as the main, simplest, and most accessible method for mini-emulsion polymerisation, microfluidics, and layer-by-layer adsorption of polyelectrolytes. Such systems will undoubtedly be promising for use in biotechnology and medicine due to the fact that they are liquid-swollen particles capable of binding and carrying various low to high molecular weight substances. It is also important that slight heating and cooling or a slight change in the pH of the medium shifts the system from a homogeneous to a heterogeneous state and vice versa. This provides the opportunity to use these polymers as a means of targeted drug delivery, thereby reducing the negative effect of toxic substances used for treatment on the entire body and directing the action to a specific point. In addition, such polymers can be used to create smart coatings of implanted materials, as well as an artificial matrix for cell and tissue regeneration, contributing to a significant increase in the survival rate and regeneration rate of cells and tissues.

Keywords: hydrogel, microgel, N-isopropylacrylamide, thermal sensitivity, pH sensitivity, heterophase polymerisation.

***Funding*:** The study was supported by the National Medical Research Center for Obstetrics, Gynecology, and Perinatology named after Academician V.I. Kulakov of the Ministry of Healthcare of the Russian Federation, within the financial support of the government order «Development and implementation of methods for restoring the endometrium based on liquid bioengineering tissue with a controlled phase transition temperature» in 2020.

For citation: Kuznetsov V. A., Kushchev P. O., Ostankova I. V., Pulver A. Yu., Pulver N. A., Pavlovich S. V., Poltavtseva R. A. Modern approaches to the medical use of copolymer pH- and temperature-sensitive hydrogels (review). *Kondensirovannye sredy i mezhfaznye granitsy = Condensed Matter and Interphases.* 2020; 22(4): 417–429. DOI: https://doi.org/10.17308/kcmf.2020.22/3113

Для цитирования: Кузнецов В. А., Кущев П. О., Останкова И. В., Пульвер А. Ю., Пульвер Н. А., Павлович С. В., Полтавцева Р. А. Современные подходы к медицинскому использованию сополимерных pH- и температурно-чувствительных гидрогелей (обзор). *Конденсированные среды и межфазные границы*. 2020; 22(4): 417–429. DOI: https://doi.org/10.17308/kcmf.2020.22/3113

✉ Kushchev Petr Olegovich, e-mail: peter.kuschev@gmail.com

1. Introduction

In recent decades, a new scientific direction has emerged at the intersection of polymer chemistry, nanotechnology, biology, pharmaceuticals, biotechnology, medicine, and it is constantly attracting increased attention, associated with the so-called «smart» or «intelligent» materials [1]. Smart materials based on water-soluble polymers attract significant scientific and practical interest. This is due to the fact that they have a number of unique properties: temperature-, pH-sensitivity, structure diphilicity, etc. In this regard, they are called stimuli-sensitive polymers, since they can respond to external environmental influences [2-5]. The reaction to external influence occurs due to the amphiphilicity (diphilicity) of the (co) polymers. Usually, monomers with a structure containing both hydrophilic and hydrophobic segments are used. Such substances are now being actively used as dispersants, emulsifiers, solubilisers, in cosmetology, for the isolation of drugs, etc. [6, 7].

Among smart polymers there are representatives that can respond to changes in temperature, pH, ionic strength, the content of inorganic, organic substances and high molecular weight compounds of various natures, light intensity, electric field strength, etc. Methods for the synthesis of such hydrogels (precipitation polymerisation, emulsion polymerisation) are often simple and extremely easy to scale up to pilot production, and the synthesized particles obtained by these methods will have a rather narrow size distribution.

These systems will undoubtedly be promising for their use in biotechnology and medicine. They are a very simple tools for managing systems. Slight heating and cooling or a slight change in the pH of the medium leads to a transition from a homogeneous system to a heterogeneous one and vice versa, significantly changing the swelling capacity of the hydrogels. Such polymers are already used for the concentration and purification of biologically active substances or for the fixation of biocatalysts.

Recently, methods have been developed for the preparation of such hydrogels from biodegradable and non-toxic polymers [8]. The term hydrogels includes both macro- and microgels. The latter differ in that the polymer particles are dispersed in a liquid and are nano- or micro-objects. Due to the fact that the microgel is a liquid-swollen particle, they can bind and transport inside various substances of low to high molecular weight. This fact suggests that such systems are ideal for the delivery of drugs. It is possible to create a system with precisely specified parameters at which it will operate effectively, achieving accurate drug delivery to the affected cells and tissues by adjusting the size of particles during synthesis or by the external action of the environment (temperature, pH), and by introducing various monomers, regulating the sensitivity and decomposition rate into the composition of the microgel. Additionally, hydrogels also offer great opportunities for regenerative medicine: surfaces coated with such polymers can be used for the growth of cells with the formation of tissues, which can be used either as external coatings for biomaterials for implantation, or for use in the regeneration of various parts of the body.

2. Drug delivery systems

Due to the cross-linked structure of hydrogels containing up to 90% liquid in their pores, they represent a new class of delivery systems for a wide range of different drugs [9]. The indisputable advantages of microgels include the ability to control their composition and properties during synthesis by using various approaches. Microgels with similar chemical compositions can often be obtained in a wide range of sizes from several tens of nanometres up to hundreds of micrometers (depending on the preparation method or the composition of the reaction mixture). By varying the degree of cross-linking of microgels, it is possible to change the pore size inside them, which can be used for the controlled release of the drug loaded into the microgel.

The use of numerous bioconjugation reactions allows the functionalisation of microgels, which is necessary for the transition from “passive” to “active” delivery [10].

The cross-linked structure of microgels provides opportunities for the creation of hybrid nanobiomaterials capable of combining such important biomedical applications as targeted delivery and visualization (the very popular «theranostics» principle [11], derived

from the combination of the words therapy and diagnostics) or targeted delivery and the possibility of local warming up (which is used for hyperthermia therapy with tumours).

In contrast to liposomes, which have been well studied over the past decades and are now widely used in targeted drug delivery therapy, microgels are a less studied and broader class of delivery containers. The most popular are microgels based on polysaccharides: chitosan, dextran, cellulose, and others. [12, 13]. The use of protein-based microgels for targeted delivery is less preferable, since they are more immunogenic; in turn, the use of microgels based on human (albumin) or non-immunogenic proteins (collagen, gelatin) opens up possibilities for the simple synthesis of biodegradable drug carriers [14]. Microgels based on natural polymers have high biocompatibility and extremely low toxicity, but they can be recognised by the components of the immune system and excreted from the body. In turn, synthetic polymers, especially those containing hydrophilic polyethylene glycol or polyglycerol macromonomers have extremely high stability in solution and reduced sorption of proteins, which makes them analogues of «*stealth*'-liposomes. Among synthetic polymers, the overwhelming majority of studies were devoted to microgels based on poly(N-isopropylacrylamide) PNIPAAm [15]. The reasons for this are the ease of preparation and monodispersity of microgels synthesized by the precipitation polymerisation mechanism in an aqueous solution. Among other polymers of targeted delivery using microgels, polymers based on 2- hydroxyethyl methacrylate (HEMA) and oligoethylene glycol methacrylate (OEGMA) are widely used [14].

The possibility to load significant amounts of drug into a microgel and the efficient and controlled release of the loaded drug is important for drug delivery. This requires the binding of the drug to the microgel. This is usually achieved due to hydrophobic interactions (low solubility of the drug in water), but it has been shown that hydrophobic interactions are not enough for the achievement of high (20% or more) degrees of loading with the drug and other types of interactions, hydrogen bonds or electrostatic attraction are required [16].

In most studies, microgels are used to deliver cytostatics: doxorubicin, daunorubicin, cisplatin, and methotrexate [9]. In these studies, microgels are analogues of the liposomal formulations of the mentioned drugs, and the effects observed during their use is often similar. However, the use of microgels open up a wider range of possibilities for the delivery of hydrophilic drugs with a significant number of charged groups. In this case, the binding between the drug and the microgel is carried out due to numerous ionic interactions between the opposite charges of the drug and the hydrogel. This approach was successfully applied in studies based on the delivery of nucleotide triphosphate analogues [17].

The use of ionic interactions for the production of drug-microgel complex is extremely important for biomolecules: nucleic acids and proteins. Microgels can very effectively act as containers for the delivery of biomolecules such as proteins and peptides [18], which makes their use a very promising direction for the delivery vector of drugs.

The use of microgels allows avoiding the side effects of cytostatics, reducing their general toxicity and nephrotoxicity, and contributing to the improvement of the condition of animals in *in vivo* models. Now, the study of targeted drug delivery is one of the most rapidly developing directions and obviously, other drugs will be used for introduction via microgels.

The release of the drug is also crucial for the effective action of the microgel. In many cases, the release of the drug occurs spontaneously, due to diffusion or ion exchange. The use of temperature-sensitive, photosensitive, pH-sensitive polymers allows the controlled release of the drug, providing the selectivity of action on tumours [19].

The environment of a tumour often has a more acidic pH, due to its high metabolic activity and poor development of its lymphatic vessels. pH-dependent swelling of microgels is a universal mechanism of drug release from a microgel, which has been widely investigated in numerous studies. An interesting approach is also pH-dependent swelling leading to the release of functional groups on the microgel surface, which are hidden at a normal pH of 7.4.

In this case, functional groups can be both ligands to receptors on the surface of cancer cells and viral peptides (TAT peptide, etc.), providing an effective pH-dependent penetration of microgels into cells [20].

There are several methods used for the production of biodegradable microgels (8). First, degradable polymers can be used. One example is certain natural biopolymers: polysaccharides and their derivatives, collagen cross-linked with glutaric dialdehyde and many others, as well as widely used polymers based on a copolymer of lactic and glycolic acid (PLGA) or their derivatives. On the other hand, the degradation of the microgel into monomers in the body is not necessary. The polymer itself may be indestructible, but contain crosslinks that can decompose in the body spontaneously (often contain bonds unstable in the acidic pH range, observed in cell lysosomes): β-thiopropionate bonds, methacrylic esters of PLGA, orthoesters, or under the action of certain enzymes. The latter can be based on derivatives of peptides specifically recognised by metalloproteinases.

One of the simplest and most well-studied methods for achieving the degradability of a polymer is the introduction of a crosslinking agent containing a disulphide bond. Often, the synthesis reaction is a radical polymerisation – RAFT polymerisation (*Reversible Addition-Fragmentation chain Transfer*) [21]. The use of RAFT allows more precise control over the composition and properties of synthesised microgels. Disulphide bonds can be easily reduced in a cell's cytoplasm due to the presence of a reduction system, using the glutathione reductase enzyme and the tripeptide glutathione substrate that is present in cells at a concentration of about 5 mM. This system effectively reduces -S-S- bonds due to the disulphide exchange.

Microgels in a swollen state in aqueous solutions are of particular interest. This group of microgels is also often referred to as hydrogels. Hydrogels attract great interest due to their unique physicochemical properties and the huge number of practical applications from photonic crystals and microlenses to containers for drug delivery [22]. Thus, microgels represent an extremely wide class of materials with various compositions, sizes, and morphologies.

According to their method of preparation and the nature of the crosslinking, microgels are often subdivided into physically and chemically crosslinked types [23]. The physical microgels include gels, represented by polymer networks interconnected due to the interlacing of individual macromolecules and/or numerous non-covalent interactions existing between polymer chains. The attractive forces, holding the chains together are hydrogen bonds, van der Waals, electrostatic, or hydrophobic interactions. Thus, such microgels can be reversibly dissolved under certain conditions that weaken these interactions (changes of pH, ionic strength, or the addition of chaotropic reagents).

Another class of hydrogels are chemically crosslinked gels. These microgels are highly stable due to the presence of covalent bonds connecting polymer chains in the microgel network. The main method for obtaining such microgels is polymerisation using polyfunctional crosslinking monomers. At the moment, microgels include a huge variety of polymer particles with different properties. The differences in properties lead to the possibility of classifying certain microgels by their type of sensitivity. Sensitivity is the ability to change physical and chemical properties under the influence of various external parameters.

The most common of these parameters are temperature, pH, ionic strength, light intensity, electromagnetic radiation, and even some simple organic molecules [24]. Most often, microgels undergo a change in their volume, which can be used in many fields of science, such as biotechnology and biomedicine [25].

In addition to the classification according to the sensitivity type, there is a classification according to the method of production. At the moment, there are many different methods with their own advantages and disadvantages. Mini-emulsion copolymerisation of water-soluble monomers in immiscible organic solvents in the presence of surfactants allowing strictly control the composition of the obtained microgels. Using this method it is easy to synthesize microgels with water-soluble macromolecules (proteins, etc.) included in them, as well as nanoparticles (Fe_3O_4, Pd, Ag, CdSe). The disadvantages of the mini-emulsion polymerisation method [26] include the need to use an external dispersing action, which

often leads to the destruction of biomolecules included in the microgel network.

Microfluidics is a unique method for the synthesis of microgels, which allows the synthesis of polymer particles from 1 to 200 μm, with the narrowest possible size distribution. This is achieved due to the controlled disintegration of the jet of one phase in the medium of the other phase. The special geometry of the channel and the ability to generate different types of drops allow obtaining particles of various shapes, and the channel cross-section diameter strictly determines the range of admissible particle sizes [27]. The particle size of such microgels also depends on the flow rate of the dispersion phase. The advantages of this method include control over the morphology and structure of the resulting particles. Microfluidics allows synthesizing Janus particles (a type of multifunctional micro- or nanosized particles consisting of two or more parts of different chemical composition and/or shape, with different properties) under very mild conditions [28], microgels with particles of various shapes, as well as layered structures by polymerisation of drop-in-drop structures [29], which, in turn, makes it possible to obtain hybrid particles, including those containing living cells inside [30]. The disadvantages of this method include very low productivity, high cost, and the size range of synthesized microgels from few to hundreds of micrometres.

A fundamentally different approach, similar to microfluidics, was developed by *De Simone*. This method is unique, since it allows obtaining polymer particles ranging in size from several tens of nanometres to several microns. This method [31], named "PRINT" (*Particle Replication In Non-wetting Templates*), is a variant of imprint lithography using elastomeric moulds coated with a hydrophobic perfluoropolymer. A solution of monomers or macromonomers in water is placed between two hydrophobic surfaces, a polymerisation or polycondensation process is carried out, after which the surfaces can be easily separated from each other, and the particles can be removed from the mould. This method has undeniable advantages such as strict control of particle size, shape, and composition, and surface functionality. The mild synthesis conditions allow the introduction of unstable compounds and biomolecules into the microgel system without losing their functionality.

Layer-by-layer adsorption of a polyelectrolyte is one of the most common methods for producing capsules and microgels. *Decher* created the generation of multilayer films on the surface by successive adsorption of cationic and anionic polyelectrolytes [32]. This approach can be used to coat microgels or nanoparticles with polyelectrolytes. For instance, *Sauzedde* [33, 34] described an interesting procedure in which anionic iron oxide nanoparticles (about 10 nm) were adsorbed by cationic microgels. Furthermore, the polymer containing carboxyl groups formed a coating on the surface of the initial microgels, surrounding them with its shell. The approach combining two processes: controlled self-assembly of polymer micelles with the subsequent covalent crosslinking, which provides tremendous opportunities for large-scale production of microgels with a controlled structure. This method allows obtaining a wide range of microgels with various structures by simple selection of solvents and counterions. Using this method spheres, ellipses, and even toroids were obtained [19]. The disadvantages of this method include the need to use monodisperse polymers with a strictly controlled structure and molecular weight, as well as the multi-stage synthesis from monomers to final products.

One of the most attractive approaches to the synthesis of microgels is the use of precipitation polymerisation [35]. The indisputable advantages of this method include the single-stage operation, ease of scaling, high productivity, and the use of water as a solvent («green chemistry»). The composition can be controlled by introducing various monomers capable of providing the desired properties to the microgels. A feature of this process is that during the polymerisation, using a monomer forming a temperature-sensitive polymer, nucleus particles are formed almost simultaneously throughout the volume.

This, in turn, leads to an unusually high monodispersity of microgels for free radical polymerisation. The disadvantages of this reaction include the need to carry out the reaction under heat (usually about 70 °C) and in the presence of free radicals, which excludes the possibility of the direct introduction of sensitive

reagents and biomolecules into the reaction; however, this can be effectively carried out after the synthesis and purification of microgels.

3. Functional biomaterials

The most obvious application of temperature-sensitive hydrogels is culture dishes with layers of PNIPAAm of various thickness and density on the bottom [36], allowing to the adhesion and detachment of cells to be controlled by changing the temperature, forming a cell monolayer detachable from the substrate. One of advantages is that the temperature-sensitive hydrogel remaining on its basal surface [37] acts as a cell glue at body temperature, and the cell layers can be easily transplanted by simply placing the cell layer on the affected area without sutures or other methods of fixation. In addition, cell layers remain in place after transplantation, while cells transplanted as part of an injectable cell suspension have a tendency to migrate [38].

Various types of culture dishes were investigated for the efficient production of cell layers, which led to the emergence of new biomedical technologies (Table 1).

In addition, the cellular activity of monolayers separated from the substrate by simply lowering the temperature can exceed that of cells mobilised by digestive enzymes (trypsin) and emulsifiers (EDTA/EGTA). Thus, the secretion of certain cytokines by the cells of the cell layer may be higher than that of the cell suspension, which can have therapeutic effects.

While exploring the potential use of microgels as coatings for biomaterials, *Gan* and *Lyon* investigated temperature-sensitive PNIPAAm nanoparticles grafted with polyethylene glycol (PEG), obtained by free radical precipitation copolymerisation with PEG monomethyl ether monomethacrylate (M_w = 1 kDa) [48]. The solution to the problems of a wide particle size distribution, expansion of the volumetric phase transition of microgels, and a shift in the phase transition temperature to a higher temperature range due to the presence of PEG, was determined to be a two-stage method of precipitation polymerisation. As a result, PEG chains were localised at the outer boundary of the particles. Consistent with numerous previous studies on PEG grafting on both macroscopic surfaces and particles/macromolecules [49, 50], it was found that protein adsorption on the microgel is suppressed by the incorporation of PEG into the particles, especially when these chains are located in the microgel shell.

Both protein adsorption studies and ^{1}H NMR showed that the PEG side chains stretch outward from the surface of the particles and that the particles break down at temperatures above the phase transition temperature. Interestingly, similar effects were observed for particles where PEG chains are localised in the particle core. This suggests that PEG grafts could penetrate through the PNIPAAm shell when it is in its phase-separated state.

Similarly, *Nolan* et al. investigated the phase transition and protein adsorption for PNIPAAm microgel particles cross-linked with PEG diacrylates with different ratios and different chain lengths [51]. Based on the method of light scattering, an increase in the temperature and the magnitude of the phase transition with an increase in the concentration of the PEG crosslinking agent included in the microgels was found. Qualitative differences in particle density using centrifugation showed that the obtained microgel networks are denser with a higher PEG concentration. Based on the studies of NMR spectroscopy, it was concluded that the longer cross-links of PEG protrude from the dense globular network, leading to a decrease in non-specific protein adsorption with increasing chain length and PEG content. Similarly, surface-bound microgels containing longer PEG chains showed the absence of fouling and resistance to cell adhesion in serum-containing media.

A similar suppression of protein adsorption and cell adhesion was observed by Scott et al. for microgel aggregates formed by octavinyl sulfone, modified by PEG and bovine serum albumin [52]. Considering the geometry-independent surface modification, PEGylated microgels are of potential interest in areas of science requiring antifouling coatings.

South et al. investigated the use of centrifugal aggregation of microgel films for further improvement of the performance of microgel-based coatings by increasing their surface density [53]. In this case, films formed from microgel particles were obtained either by centrifugation

Table 1. Typical threads of cell sheets in restorative therapy implementation

Therapeutic Uses	Cells	Method for creating cell layers	Sources
Corneal plastic	Oral mucosa epithelium	Using temperature-sensitive well plate inserts for culture plates and 3T3 feeder cells treated with mitomycin C.	[39]
Elimination of intraoperative air leak syndrome	Dermal fibroblasts	Using temperature-sensitive culture dishes, transplantation of bilayer cell layers.	[40]
Periodontal regeneration	Periodontal ligament derived cells	Using temperature-sensitive culture dishes, three-layer cell layers with the addition of woven polyglycolic material; bone defects are filled with porous β-tricalcium phosphate.	[41]
Treatment of dilated cardiomyopathy	Myoblasts of striped muscles	Using temperature-sensitive culture dishes, transplantation of cell multilayers	[42]
Prevention of stricture formation after endoscopic excision of the esophageal submucosa	Epithelial cells of the oral mucosa	Using temperature-sensitive well plate inserts for culture plates and endoscopic applications.	[43]
Cartilage restoration	Chondrocytes from knee joints	Using temperature-sensitive culture dishes, transplantation of cell multilayers.	[44, 45]
Prevention of intrauterine adhesions	Epithelial cells of the oral mucosa	Using temperature-sensitive well plate inserts for culture plates and NIH-3T3 feeder cells.	[46]
Postoperative reconstruction of the middle ear mucosa	Epithelial cells of the nasal mucosa	Using temperature-sensitive well plate inserts for culture plates.	[47]

("active" method) or by submerged adsorption ("passive" method). It was found that microgels actively deposited on the surface have smaller imprints and are more densely packed, compared to the reduced surface spread of globular proteins at strong deposition from the flow. Using this advantage, "active" deposition was demonstrated for the production of polyelectrolyte multilayer materials containing anionic microgels and a cationic linear polymer. Such multilayer microgels have been shown to effectively block the underlying substrate for the adhesion of macrophages, which is interesting, for example, for the modulation of the inflammatory response to implanted biomaterials.

Additionally, *Wang* et al. studied the use of self-assembling microgels for the suppression of bacterial colonisation of synthetic surfaces [54]. In this case, two antimicrobial mechanisms were investigated, namely: 1) modulation of cell surface adhesion; and 2) local storage/release of antimicrobial substances. For this, PEG-based microgels and a copolymer of PEG with acrylic acid (PEG-AA) were synthesized by the suspension photopolymerisation method, and the obtained microgels were deposited on silicon coated with poly-L-lysine, forming a submonolayer coating. After deposition, a cationic antimicrobial peptide (L5) was introduced into the microgel, and the peptide content was significantly higher in PEG-AA microgels than in pure PEG microgels due to the electrostatic factor. Coating a peptide-free silicon substrate with a PEG-AA microgel significantly reduced surface colonisation by *S. epidermidis* and the degree of inhibition increased with the decrease in the average distance between microgels and surface bonds. The introduction of an L5 peptide into microgels after deposition further reduced coating colonisation with *S. epidermidis* to the low value observed for the control macroscopic PEG gel.

Wang and *Libera* investigated the surface deposition of microgels formed by the suspension polymerisation of AA and PEG on silicon surfaces modified with polylysine and the effect of their granular nature on protein adsorption [55]. Surface-bound PEG-AA microgels effectively

prevented the adsorption of fibronectin. In contrast, unprotected polylysine between adhered microgel particles (subconfluent coating) readily adsorbed this protein, thereby creating a disordered array of submicron-sized non-adhesive regions on the adherent cell surface. It has been found that compared to completely adhered surfaces, microgel coatings lead to rapid distribution and proliferation of cells, while the direction of differentiation does not change. Scanning electron microscopy (SEM) studies demonstrated that osteoblasts grow above the surface of the microgel, adhering to the surface areas exposed to polylysine, while optical microscopy with temporalsm resolution demonstrates higher cell mobility on the surface covered with microgel. These findings correspond with numerous studies of biomaterial surfaces structured in different ways and are consistent with the concept of intercellular interactions on the surface, regulated by the spatial distribution of cell adhesion sites. In addition, they suggest that microgel adsorption may represent an interesting way to control cellular processes involved in healing after biomaterial implantation.

Similar *Tsai* et al. investigated PNIPAAm microgels deposited on polystyrene substrates by immersion [56]. As the substrate removal rates were changed, surface structures were formed. Stripes of densely packed PNIPAAm microgels separated by intervals containing sparsely distributed microgels were clearly visible on these surface structures. It was found that NIH-3T3 cells plated on such micropatterned substrates, are fixed predominantly in the spaces, forming cell agglomerates. The cells formed confluent cell layers three days after plating. The extraction of fibroblast cell layers from substrates was carried out by lowering the temperature due to the temperature-sensitivity of the underlying layer of PNIPAAm microgel, similar to other modified PNIPAAm layers or differently reacting surfaces for collecting cell layers.

Considering the problem of interaction of cells with various surface features of granular microgel films, *Lynch* et al. studied the production of polymer coatings with controlled surface topography on a micrometre scale using microgel particles [57]. By changing the interaction between the microgel particles, the particles were phase-separated into dense and particle-depleted domains, which remained on the surface after evaporation of the solvent. When the particle size changes, the size of the formed pores and their distribution in the film also change. It was shown that such systems can be formed into various structures, even obtained from microgel particles of the same size and the same composition. For *HeLa* cells grown on the surfaces of microgel based on 200 nm tert-butylacrylamide/isopropylacrylamide, cells could either grow in the pores of the microgel, where their distribution was limited by the pore size, or they could grow along dense domains between the pores, in this case, the cells had an elongated shape.

Li et al. focused on controlled surface heterogeneity, combining the assembly with control of surface wettability by microdroplets using embossing with polydimethyldisiloxane and subsequent fixation for the assemblage of thousands of heterogeneous three-dimensional microenvironments for cells with precise control of individual shapes, sizes, chemical concentrations, cell density, and three-dimensional spatial distribution of many components [58].

The biological reactions on surfaces coated with a microgel have been most fully described in the studies of *Bridges* et al. devoted to the biological response of thin films formed by PNIPAAm microgels crosslinked with polyethylene glycol diacrylate [59]. These particles were grafted onto a conformally coated PET substrate, which was found to significantly reduce fibrinogen adsorption as well as adhesion and proliferation of primary human monocytes/macrophages. It was also found that microgel coatings lead to a decrease in the adhesion of leukocytes, as well as anti-inflammatory cytokines (TNFa, IL-1b, MCP-1) after intraperitoneal implantation.

Evaluating the biological response of a microgel-coated surface *in vivo*, *Bridges* et al. investigated chronic inflammatory reactions to microgel coatings consisting of PNIPAAm microparticles crosslinked with polyethylene glycol diacrylate applied on PET [60]. At the same time, unmodified and microgel-coated PET discs were implanted subcutaneously in rats for 4 weeks, and the explants were analysed using histology and immunohistochemistry. Microgel

coatings have been found to reduce chronic inflammation and result in thinner fibrous capsules that contain 40% less cells compared to unmodified PET discs. In addition, the microgel coated samples contained significantly higher levels of macrophages (80%) than unmodified PET. These results demonstrate that microgel coatings reduce chronic inflammation caused by implanted biomaterials.

However, there are also reports that microgel coatings do not provide improved performance and biological response to biomaterials. Thus, considering that the effectiveness of neural electrodes implanted in the brain is often limited by host responses in the surrounding brain tissue, including astrocytic scar formation, neuronal cell death, and inflammation. *Gutowski* et al. investigated the host response to silicon neural electrodes with surface coatings formed by PNIPAAm-co-acrylic acid-PEG microgels and without them [61]. The adhesion of astrocytes and microglia for microgel-coated electrodes compared to uncoated controls was significantly reduced *in vitro*. In addition, the microgel coatings reduced the array of astrocytes around the implant for electrodes implanted in a rat's cerebral cortex. However, the microglia response indicated persistent inflammation, and the density of neurons around the implanted electrodes was lower for both groups of implants in comparison with the intact sample. Thus, it was concluded that microgel coatings did not significantly improve host response to implanted neural electrodes.

Although the main focus in the context of biomaterials has been on implant-related issues, the use of microgel coatings offers great opportunities, for example, for cell differentiation and growth, which can be used either as coatings for the surface of biomaterials or for applications in regenerative medicine.

Similarly with surfaces modified by grafting or adsorption of PNIPAAm or other temperature-sensitive polymers [62], cell adhesion improves at elevated temperatures (e.g. when bonds are broken due to deterioration of dissolution conditions), while cell detachment occurs when the temperature decreases or the solubility of PNIPAAm chains increases, causing the swelling of chains. By examining these effects, *Schmidt* and co-authors demonstrated that PNIPAAm microgel films can be used for the controlled separation of adsorbed cells using temperature-sensitivity [63]. In this case, the properties of the microgel in the adsorbed state, as well as their changes with a change in temperature, were studied using the atomic force microscopy (AFM) method. Analysis shows that water content, surface adhesion, and nanomechanical properties change dramatically when the polymer film reaches a critical temperature, thus creating the basis for the rapid response of cells to temperature changes, both in terms of the number of fixed cells and their morphology. Similar results were also presented by *Uhlig* et al. [64].

4. Conclusions

The study of pH- and temperature-sensitive copolymers for medical use is a very promising area. This conclusion can be made after the analysis of a significant number of studies devoted to the use of such materials both as containers for delivery of medicinal substances, and as functional biomaterials, using which it is possible to create coatings for implants, as well as an artificial matrix for cell and tissue regeneration. Such smart polymers allow the flexible adjustment of the properties required in each specific case under the conditions in which they will perform their functions as efficiently as possible. This can be done by varying the composition of the copolymer, the degree of crosslinking of macromolecules, the use of various stabilising and initiating systems, as well as different methods of synthesis. Thus, pH- and temperature-sensitive polymer and copolymer materials provide researchers with a powerful tool that can change the approach to the treatment of many serious diseases.

Conflict of interest

The authors declare that they have no known competing financial interests or personal relationships that could have influenced the work reported in this paper.

References

1. Gisser K. R. C., Geselbracht M. J., Cappellari A., Hunsberger L., Ellis A. B., Perepezko J., et al. Nickel-titanium memory metal: A «Smart» material exhibiting a solid-state phase change and superelasticity. *Journal*

of Chemical Education. 1994;71(4): 334. DOI: https://doi.org/10.1021/ed071p334

2. Erman B., Flory P.J. Critical phenomena and transitions in swollen polymer networks and in linear macromolecules. *Macromolecules*. 1986;19(9): 2342–2353. DOI: https://doi.org/10.1021/ma00163a003

3. Tanaka T., Fillmore D., Sun S.-T., Nishio I., Swislow G., Shah A. Phase transitions in ionic gels. *Physical Review Letters*. 1980;45(20): 1636–1639. DOI: https://doi.org/10.1103/physrevlett.45.1636

4. *Polymer Gels*. DeRossi D., Kajiwara K., Osada Y., Yamauchi A. (eds.). Boston, MA: Springer US; 1991. 354 p. DOI: https://doi.org/10.1007/978-1-4684-5892-3

5. Ilmain F., Tanaka T., Kokufuta E. Volume transition in a gel driven by hydrogen bonding. *Nature*. 1991;349(6308): 400–401. DOI: https://doi.org/10.1038/349400a0

6. Kuhn W., Hargitay B., Katchalsky A., Eisenberg H. Reversible dilation and contraction by changing the state of ionization of high-polymer acid networks. *Nature*. 1950;165(4196): 514–516. DOI: https://doi.org/10.1038/165514a0

7. Steinberg I. Z., Oplatka A., Katchalsky A. Mechanochemical engines. *Nature*. 1966;210(5036): 568–571. DOI: https://doi.org/10.1038/210568a0

8. Tian H., Tang Z., Zhuang X., Chen X., Jing X. Biodegradable synthetic polymers: Preparation, functionalization and biomedical application. *Progress in Polymer Science*. 2012;37(2): 237–280. DOI: https://doi.org/10.1016/j.progpolymsci.2011.06.004

9. Gonçalves C., Pereira P., Gama M. Self-Assembled hydrogel nanoparticles for drug delivery applications. *Materials*. 2010;3(2): 1420–1460. DOI: https://doi.org/10.3390/ma3021420

10. Pangburn T. O., Petersen M. A., Waybrant B., Adil M. M., Kokkoli E. Peptide- and Aptamer-functionalized nanovectors for targeted delivery of therapeutics. *Journal of Biomechanical Engineering*. 2009;131(7): 074005. DOI: https://doi.org/10.1115/1.3160763

11. Caldorera-Moore M. E., Liechty W. B., Peppas N. A. Responsive theranostic systems: integration of diagnostic imaging agents and responsive controlled release drug delivery carriers. *Accounts of Chemical Research*. 2011;44(10): 1061–1070. DOI: https://doi.org/10.1021/ar2001777

12. Das M., Sanson N., Fava D., Kumacheva E. Microgels loaded with gold nanorods: photothermally triggered volume transitions under physiological conditions†'. *Langmuir*. 2007;23(1): 196–201. DOI: https://doi.org/10.1021/la061596s

13. Oh J. K., Lee D. I., Park J. M. Biopolymer-based microgels/nanogels for drug delivery applications. *Progress in Polymer Science*. 2009;34(12): 1261–1282. DOI: https://doi.org/10.1016/j.progpolymsci.2009.08.001

14. Oh J. K., Drumright R., Siegwart D. J., Matyjaszewski K. The development of microgels/nanogels for drug delivery applications. *Progress in Polymer Science*. 2008;33(4): 448–477. DOI: https://doi.org/10.1016/j.progpolymsci.2008.01.002

15. Talelli M., Hennink W. E. Thermosensitive polymeric micelles for targeted drug delivery. *Nanomedicine*. 2011;6(7): 1245–1255. DOI: https://doi.org/10.2217/nnm.11.91

16. Bromberg L., Temchenko M., Hatton T. A. Smart microgel studies. Polyelectrolyte and drug-absorbing properties of microgels from polyether-modified poly(acrylic acid). *Langmuir*. 2003;19(21): 8675–8684. DOI: https://doi.org/10.1021/la030187i

17. Vinogradov S. V. Polymeric nanogel formulations of nucleoside analogs. *Expert Opinion on Drug Delivery*. 2007;4(1): 5–17. DOI: https://doi.org/10.1517/17425247.4.1.5

18. Vinogradov S. V. Colloidal microgels in drug delivery applications. *Current Pharmaceutical Design*. 2006;12(36): 4703–4712. DOI: https://doi.org/10.2174/138161206779026254

19. Kabanov A. V., Vinogradov S. V. Nanogels as pharmaceutical carriers: finite networks of infinite capabilities. *Angewandte Chemie International Edition*. 2009;48(30): 5418–5429. DOI: https://doi.org/10.1002/anie.200900441

20. Lee E. S., Gao Z., Bae Y. H. Recent progress in tumor pH targeting nanotechnology. *Journal of Controlled Release*. 2008;132(3): 164–170. DOI: https://doi.org/10.1016/j.jconrel.2008.05.003

21. Dong H., Mantha V., Matyjaszewski K. Thermally responsive PM(EO)2MA magnetic microgels via activators generated by electron transfer atom transfer radical polymerization in miniemulsion. *Chemistry of Materials*. 2009;21(17): 3965–3972. DOI: https://doi.org/10.1021/cm901143e

22. Nayak S., Lyon L. A. Soft nanotechnology with soft nanoparticles. *Angewandte Chemie International Edition*. 2005;44(47): 7686–7708. DOI: https://doi.org/10.1002/anie.200501321

23. Hennink W. E., van Nostrum C. F. Novel crosslinking methods to design hydrogels. *Advanced Drug Delivery Reviews*. 2012;64: 223–236. DOI: https://doi.org/10.1016/j.addr.2012.09.009

24. Motornov M., Roiter Y., Tokarev I., Minko S. Stimuli-responsive nanoparticles, nanogels and capsules for integrated multifunctional intelligent systems. *Progress in Polymer Science*. 2010;35(1-2): 174–211. DOI: https://doi.org/10.1016/j.progpolymsci.2009.10.004

25. Saunders B. R., Laajam N., Daly E., Teow S., Hu X., Stepto R. Microgels: From responsive polymer colloids to biomaterials. *Advances in Colloid and Interface Science*. 2009;147-148: 251–262. DOI: https://doi.org/10.1016/j.cis.2008.08.008

26. Landfester K. Miniemulsion polymerization and the structure of polymer and hybrid nanoparticles.

chemInform. 2009;40(33). DOI: https://doi.org/10.1002/chin.200933279

27. Seo M., Nie Z., Xu S., Mok M., Lewis P.C., Graham R., et al. Continuous microfluidic reactors for polymer particles. *Langmuir*. 2005;21(25): 11614–11622. DOI: https://doi.org/10.1021/la050519e

28. Nie Z., Li W., Seo M., Xu S., Kumacheva E. Janus and ternary particles generated by microfluidic synthesis: design, synthesis, and self-assembly. *Journal of the American Chemical Society*. 2006;128(29): 9408–9412. DOI: https://doi.org/10.1021/ja060882n

29. Seiffert S., Thiele J., Abate A. R., Weitz D. A. Smart microgel capsules from macromolecular precursors. *Journal of the American Chemical Society*. 2010;132(18): 6606–6609. DOI: https://doi.org/10.1021/ja102156h

30. Rossow T., Heyman J. A., Ehrlicher A. J., Langhoff A., Weitz D. A., Haag R., et al. Controlled synthesis of cell-Laden Microgels by Radical-Free Gelation in Droplet Microfluidics. *Journal of the American Chemical Society*. 2012;134(10): 4983–4989. DOI: https://doi.org/10.1021/ja300460p

31. Perry J. L., Herlihy K. P., Napier M. E., DeSimone J. M. PRINT: A novel platform toward shape and size specific nanoparticle theranostics. *Accounts of Chemical Research*. 2011;44(10): 990–998. DOI: https://doi.org/10.1021/ar2000315

32. Caruso F., Sukhorukov G. Coated Colloids: Preparation, characterization, assembly and utilization. In: Decher G., Schlenoff J. B., editors. *Multilayer Thin Films*. Weinheim, FRG: Wiley-VCH Verlag GmbH & Co. KGaA; 2002. 331–362 p.

33. Sauzedde F., Elaïssari A., Pichot C. Hydrophilic magnetic polymer latexes. 2. Encapsulation of adsorbed iron oxide nanoparticles. *Colloid & Polymer Science*. 1999;277(11): 1041–1050. DOI: https://doi.org/10.1007/s003960050488

34. Sauzedde F., Elaïssari A., Pichot C. Hydrophilic magnetic polymer latexes. 1. Adsorption of magnetic iron oxide nanoparticles onto various cationic latexes. *Colloid & Polymer Science*. 1999;277(9): 846–855. DOI: https://doi.org/10.1007/s003960050461

35. Pich A., Richtering W. Microgels by Precipitation Polymerization: Synthesis, Characterization, and Functionalization. In: Pich A., Richtering W. (eds.) *Chemical Design of Responsive Microgels*. Springer Heidelberg Dordrecht London New York; 2011. p. 1–37. DOI: https://doi.org/10.1007/978-3-642-16379-1

36. Yamada N., Okano T., Sakai H., Karikusa F., Sawasaki Y., Sakurai Y. Thermo-responsive polymeric surfaces; control of attachment and detachment of cultured cells. *Die Makromolekulare Chemie, Rapid Communications*. 1990;11(11): 571–576. DOI: https://doi.org/10.1002/marc.1990.030111109

37. Kushida A., Yamato M., Konno C., Kikuchi A., Sakurai Y., Okano T. Decrease in culture temperature releases monolayer endothelial cell sheets together with deposited fibronectin matrix from temperature-responsive culture surfaces. *Journal of Biomedical Materials Research*. 1999;45(4): 355–362. DOI: https://doi.org/10.1002/(sici)1097-4636(19990615)45:4<355::aid-jbm10>3.0.co;2-7

38. Sekine H., Shimizu T., Dobashi I., Matsuura K., Hagiwara N., Takahashi M., et al. Cardiac cell sheet transplantation improves damaged heart function via superior cell survival in comparison with dissociated cell injection. *Tissue Engineering Part A*. 2011;17(23-24): 2973–2980. DOI: https://doi.org/10.1089/ten.tea.2010.0659

39. Nishida K., Yamato M., Hayashida Y., Watanabe K., Yamamoto K., Adachi E., et al. Corneal reconstruction with tissue-engineered cell sheets composed of autologous oral mucosal epithelium. *The New England Journal of Medicine*. 2004;351(12): 1187–1196. DOI: https://doi.org/10.1056/nejmoa040455

40. Kanzaki M., Yamato M., Yang J., Sekine H., Kohno C., Takagi R., et al. Dynamic sealing of lung air leaks by the transplantation of tissue engineered cell sheets. *Biomaterials*. 2007;28(29): 4294–4302. DOI: https://doi.org/10.1016/j.biomaterials.2007.06.009

41. Iwata T., Yamato M., Tsuchioka H., Takagi R., Mukobata S., Washio K., et al. Periodontal regeneration with multi-layered periodontal ligament-derived cell sheets in a canine model. *Biomaterials*. 2009;30(14): 2716–2723. DOI: https://doi.org/10.1016/j.biomaterials.2009.01.032

42. Sawa Y., Miyagawa S., Sakaguchi T., Fujita T., Matsuyama A., Saito A., et al. Tissue engineered myoblast sheets improved cardiac function sufficiently to discontinue LVAS in a patient with DCM: report of a case. *Surgery Today*. 2012;42(2): 181–184. DOI: https://doi.org/10.1007/s00595-011-0106-4

43. Ohki T., Yamato M., Ota M., Takagi R., Murakami D., Kondo M., et al. Prevention of esophageal stricture after endoscopic submucosal dissection using tissue-engineered cell sheets. *Gastroenterology*. 2012;143(3): 582–588. DOI: https://doi.org/10.1053/j.gastro.2012.04.050

44. Ebihara G., Sato M., Yamato M., Mitani G., Kutsuna T., Nagai T., et al. Cartilage repair in transplanted scaffold-free chondrocyte sheets using a minipig model. *Biomaterials*. 2012;33(15): 3846–3851. DOI: https://doi.org/10.1016/j.biomaterials.2012.01.056

45. Sato M., Yamato M., Hamahashi K., Okano T., Mochida J. Articular cartilage regeneration using cell sheet technology. *The Anatomical Record*. 2014;297(1): 36–43. DOI: https://doi.org/10.1002/ar.22829

46. Kuramoto G., Takagi S., Ishitani K., Shimizu T., Okano T., Matsui H. Preventive effect of oral mucosal epithelial cell sheets on intrauterine adhesions. *Human Reproduction*. 2014;30(2): 406–416. DOI: https://doi.org/10.1093/humrep/deu326

47. Yamamoto K., Yamato M., Morino T., Sugiyama H., Takagi R., Yaguchi Y., et al. Middle ear

mucosal regeneration by tissue-engineered cell sheet transplantation. *NPJ Regenerative Medicine*. 2017;2(1): 6. DOI: https://doi.org/10.1038/s41536-017-0010-7

48. Gan D., Lyon L. A. Synthesis and Protein adsorption resistance of PEG-modified poly(N-isopropylacrylamide) core/shell microgels. *Macromolecules*. 2002;35(26): 9634–9639. DOI: https://doi.org/10.1021/ma021186k

49. Veronese F. M., Mero A. The impact of PEGylation on biological therapies. *BioDrugs*. 2008;22(5): 315-329. DOI: https://doi.org/10.2165/00063030-200822050-00004

50. Sahay G., Alakhova D. Y., Kabanov A. V. Endocytosis of nanomedicines. *Journal of Controlled Release*. 2010;145(3): 182–195. DOI: https://doi.org/10.1016/j.jconrel.2010.01.036

51. Nolan C. M., Reyes C. D., Debord J. D., García A. J., Lyon L. A. Phase transition behavior, protein adsorption, and cell adhesion resistance of poly(ethylene glycol) cross-linked microgel particles. *Biomacromolecules*. 2005;6(4): 2032–2039. DOI: https://doi.org/10.1021/bm0500087

52. Scott E. A., Nichols M. D., Cordova L. H., George B. J., Jun Y.-S., Elbert D. L. Protein adsorption and cell adhesion on nanoscale bioactive coatings formed from poly(ethylene glycol) and albumin microgels. *Biomaterials*. 2008;29(34): 4481–4493. DOI: https://doi.org/10.1016/j.biomaterials.2008.08.003

53. South A. B., Whitmire R. E., García A. J., Lyon L. A. Centrifugal deposition of microgels for the rapid assembly of nonfouling thin films. *ACS Applied Materials & Interfaces*. 2009;1(12): 2747–2754. DOI: https://doi.org/10.1021/am9005435

54. Wang Q., Uzunoglu E., Wu Y., Libera M. Self-assembled poly(ethylene glycol)-co-acrylic acid microgels to inhibit bacterial colonization of synthetic surfaces. *ACS Applied Materials & Interfaces*. 2012;4(5): 2498–2506. DOI: https://doi.org/10.1021/am300197m

55. Wang Q., Libera M. Microgel-modified surfaces enhance short-term osteoblast response. *Colloids and Surfaces B: Biointerfaces*. 2014;118: 202–209. DOI: https://doi.org/10.1016/j.colsurfb.2014.04.002

56. Tsai H.-Y., Vats K., Yates M. Z., Benoit D. S. W. Two-dimensional patterns of poly(N-isopropylacrylamide) microgels to spatially control fibroblast adhesion and temperature-responsive detachment. *Langmuir*. 2013;29(39): 12183–12193. DOI: https://doi.org/10.1021/la400971g

57. Lynch I., Miller I., Gallagher W. M., Dawson K. A. Novel method to prepare morphologically rich polymeric surfaces for biomedical applications via phase separation and arrest of microgel particles. *The Journal of Physical Chemistry B*. 2006;110(30): 14581–14589. DOI: https://doi.org/10.1021/jp061166a

58. Li Y., Chen P., Wang Y., Yan S., Feng X., Du W., et al. Rapid assembly of heterogeneous 3D cell microenvironments in a microgel array. *Advanced Materials*. 2016;28(18): 3543–3548. DOI: https://doi.org/10.1002/adma.201600247

59. Bridges A. W., Singh N., Burns K. L., Babensee J. E., Andrew Lyon L., García A. J. Reduced acute inflammatory responses to microgel conformal coatings. *Biomaterials*. 2008;29(35): 4605–4615. DOI: https://doi.org/10.1016/j.biomaterials.2008.08.015

60. Bridges A. W., Whitmire R. E., Singh N., Templeman K. L., Babensee J. E., Lyon L. A., et al. Chronic inflammatory responses to microgel-based implant coatings. *Journal of Biomedical Materials Research Part A*. 2010;94A(1): 252–258. DOI: https://doi.org/10.1002/jbm.a.32669

61. Gutowski S. M., Templeman K. L., South A. B., Gaulding J. C., Shoemaker J. T., LaPlaca M. C., et al. Host response to microgel coatings on neural electrodes implanted in the brain. *Journal of Biomedical Materials Research Part A*. 2014;102(5): 1486–1499. DOI: https://doi.org/10.1002/jbm.a.34799

62. da Silva R. M. P., Mano J. F., Reis R. L. Smart thermoresponsive coatings and surfaces for tissue engineering: switching cell-material boundaries. *Trends in Biotechnology*. 2007;25(12): 577–583. DOI: https://doi.org/10.1016/j.tibtech.2007.08.014

63. Schmidt S., Zeiser M., Hellweg T., Duschl C., Fery A., Möhwald H. Adhesion and mechanical properties of PNIPAM microgel films and their potential use as switchable cell culture substrates. *Advanced Functional Materials*. 2010;20(19): 3235–3243. DOI: https://doi.org/10.1002/adfm.201000730

64. Uhlig K., Wegener T., He J., Zeiser M., Bookhold J., Dewald I., et al. Patterned thermoresponsive microgel coatings for noninvasive processing of adherent cells. *Biomacromolecules*. 2016;17(3): 1110–1116. DOI: https://doi.org/10.1021/acs.biomac.5b01728

Information about the authors

Vyacheslav A. Kuznetsov, DSc in Chemistry, Professor of the Department of Chemistry of High-Molecular Compounds and Colloid Chemistry, Voronezh State University, Voronezh, Russian Federation, Senior Researcher at the clinical immunology laboratory of the National Medical Research Center for Obstetrics, Gynecology, and Perinatology named after V. I. Kulakov of the Ministry of Healthcare of the Russian Federation, Moscow, Russian Federation; ORCID iD: https://orcid.org/0000-0002-5508-6978.

Petr O. Kushchev, PhD in Chemistry, Associate Professor of the Department of Chemistry of High-Molecular Compounds and Colloid Chemistry, Voronezh State University, Voronezh, Russian Federation, Senior Researcher at the clinical immunology laboratory of the National Medical Research Center for Obstetrics, Gynecology, and Perinatology named after V. I. Kulakov of the Ministry

of Healthcare of the Russian Federation, Moscow, Russian Federation; e-mail: peter.kuschev@gmail.com. ORCID iD: https://orcid.org/0000-0002-9715-4756.

Irina V. Ostankova, Leading Engineer of the Department of High-Molecular Compounds and Colloid Chemistry, Voronezh State University, Senior Researcher at the clinical immunology laboratory of the National Medical Research Center for Obstetrics, Gynecology, and Perinatology named after V. I. Kulakov of the Ministry of Healthcare of the Russian Federation, Moscow, Russian Federation; e-mail: sharcky7819@mail.ru. ORCID iD: https://orcid.org/0000-0002-0314-1402.

Alexander Yu. Pulver, Senior Researcher at the clinical immunology laboratory of the National Medical Research Center for Obstetrics, Gynecology, and Perinatology named after V. I. Kulakov of the Ministry of Healthcare of the Russian Federation, Moscow, Russian Federation, General Director, Head of Laboratory, Institute of Biology of Aging LLC; e-mail: pulver.ibs@gmail.com. ORCID iD: https://orcid.org/0000-0001-6673-1859.

Natalia A. Pulver, PhD in Medical Science, Member of the Voronezh Regional Public Chamber, Associate Professor, Department of System Analysis and Management in Medical Systems, Voronezh State Technical University, Head of the Admission Department of the Voronezh Regional Public Healthcare Institution «Voronezh City Clinical Emergency Hospital no. 10» for the provision of medical care to COVID-19 patients, Voronezh, Russian Federation, Senior Researcher at the clinical immunology laboratory of the National Medical Research Center for Obstetrics, Gynecology, and Perinatology named after V. I. Kulakov of the Ministry of Healthcare of the Russian Federation, Moscow, Russian Federation; e-mail: elektronika10@yandex.ru. ORCID iD: https://orcid.org/0000-0003-4549-54764.

Stanislav V. Pavlovich, PhD in Medical Science, Professor of the Department of Obstetrics, Gynecology, Perinatology, and Reproductology of the I. M. Sechenov First Moscow State Medical University of the Ministry of Health of the Russian Federation (Sechenov University), Secretary of the Academic Council of the National Medical Research Center for Obstetrics, Gynecology, and Perinatology named after V. I. Kulakov of the Ministry of Healthcare of the Russian Federation, Moscow, Russian Federation; e-mail: st.pavlovich@mail.ru. ORCID iD: https://orcid.org/0000-0002-1313-7079.

Rimma A. Poltavtseva, PhD in Biology, Leading Research Scientist at the clinical immunology laboratory of the National Medical Research Center for Obstetrics, Gynecology, and Perinatology named after V. I. Kulakov of the Ministry of Healthcare of the Russian Federation, Moscow, Russian Federation; e-mail: rimpol@mail.ru. ORCID iD: https://orcid.org/0000-0001-8625-9205.

All authors have read and approved the final manuscript.

Translated by Valentina Mittova
Edited and proofread by Simon Cox

Condensed Matter and Interphases
(Kondensirovannye sredy i mezhfaznye granitsy)

Original articles

DOI: https://doi.org/10.17308/kcmf.2020.22/3058
Received 27 August 2020
Accepted 15 September 2020
Published online 25 December 2020

ISSN 1606-867X
eISSN 2687-0711

Reactive Interdiffusion of Components in a Non-Stoichiometric Two-Layer System of Polycrystalline Titanium and Cobalt Oxides

© 2020 N. N. Afonin[a] ✉, V. A. Logacheva[b]

[a]*Voronezh State Pedagogical University,*
86 ul. Lenina, Voronezh 394043, Russian Federation

[b]*Voronezh State University,*
1 Universitetskaya pl., Voronezh 394018, Russian Federation

Abstract

We demonstrated the possibility of using the mathematical form of Darken's theory, applied to the description of the Kirkendall effect in binary systems, to the description of reactive interdiffusion in non-stoichiometric polycrystalline film oxide systems with limited solubility. The aim of the study was the simulation of reactive interdiffusion under vacuum annealing of a thin film system consisting of two non-stoichiometric polycrystalline titanium and cobalt oxides. The non-stoichiometric nature of the system assumes the presence of mobile components, free interstitial cobalt and titanium cations in it. Phase formation occurs as a result of reactive interdiffusion and trapping of mobile components of the system on inter-grain traps. The proposed mechanism describes the formation of complex oxide phases distributed over the depth of the system.

A complex empirical research technique was used, involving Rutherford backscattering spectrometry, X-ray phase analysis and modelling methods. The values of the characteristic parameters of the process were determined by numerical analysis of the experimentally obtained distributions of the concentrations of the components within the developed model. During vacuum annealing of a thin film two-layer system of non-stoichiometric TiO_{2-x}–$Co_{1-y}O$ oxides in temperature range T = 773 – 1073 K, the values of the individual diffusion coefficients of cobalt $D_{Co} = 5.1 \cdot 10^{-8} \cdot \exp(-1.0 \text{ eV}/(kT))$ cm^2/s and titanium $D_{Ti} = 1.38 \cdot 10^{-13} \cdot \exp(-0.31 \text{ eV}/(kT))$ cm^2/s were determined.

It was shown that for T = 1073 K, the phase formation of $CoTiO_3$ with a rhombohedral structure occurs. The extension of the phase formation region of complex cobalt and titanium oxides increases with an increase in the vacuum annealing temperature and at 1073 K it is comparable with the total thickness of the film system.

The model allows predicting the distribution of the concentrations of the components over the depth of multilayer non-stoichiometric systems in which reactive interdiffusion is possible.

Keywords: modelling, interdiffusion reaction, Kirkendall effect, interphases, polycrystalline films, complex oxides.

For citation: Afonin N. N., Logacheva V. A. Reactive interdiffusion of components in a non-stoichiometric two-layer system of polycrystalline titanium and cobalt oxides. *Kondensirovannye sredy i mezhfaznye granitsy = Condensed Matter and Interphases.* 2020;22(4): 430–437. DOI: https://doi.org/10.17308/kcmf.2020.22/3058

Для цитирования: Афонин Н. Н., Логачева В. А. Реакционная взаимодиффузия компонентов в нестехиометрической двухслойной системе поликристаллических оксидов титана и кобальта. *Конденсированные среды и межфазные границы*. 2020; 22(4): 430–437. DOI: https://doi.org/10.17308/kcmf.2020.22/3058

✉ Nikolay Afonin, e-mail: nafonin@vspu.ac.ru

1. Introduction

Theoretical concepts for the chemical reactions of the formation of phases of reaction products (intermetallic compounds, oxides) inside the diffusion zone separating the phases of the initial reactants are the most developed in solid state chemistry [1, 2]. In this case, a common feature of the mechanisms explaining the phase formation is the diffusion of atoms to the interphase boundary between two materials and the reactions occurring in the boundary layer.

For the polycrystalline state of materials and limited solubility of components, a mechanism of phase formation at grain boundaries throughout the entire thickness of the contacting materials is possible instead of layer-by-layer growth at the interface boundary. This approach allowed describing the interdiffusion and phase formation in polycrystalline metal-oxide thin film systems: Fe–TiO_2 and Co–TiO_2 [3–5]. In the study [6], it was extended for the thin film two-layer system of non-stoichiometric TiO_{2-x}–$Co_{1-y}O$ oxides.

The mechanism of the phase formation distributed over the depth was implemented within the framework of numerical models of reactive interdiffusion [3–6], using the mathematical formalism of Darken's theory [7]. An advantage of the theory [7] is that the distribution of the concentrations of the components over the depth of a binary system are determined as a result of solving a boundary value problem for two differential diffusion equations. They contain one effective interdiffusion coefficient, which is a linear combination of the individual diffusion coefficients of the components.

The theory [7] was first proposed for the description of interdiffusion in a binary system with the unlimited solubility of components. In studies [8, 9], it was applied to the description of the formation and growth of boundary phases in the diffusion zone.

The initial assumption of the theory [7], and, consequently, the condition for the use of its mathematical formalism, was the position of the invariability of the molar volume of the system associated with a change in its composition as a result of chemical transformations.

In the study [10], the theory [7] was first developed for the bulk reactions of the formation of metal silicides during the interaction of a film of silicide-forming metal Ni with SiC. The simulation results [10] differ significantly from the experimentally determined distribution of the components inside the extended reaction zone. In our opinion, this is due to not taking into account the change in the molar volume of the system in the process of silicide formation.

In the case of Fe–TiO_2, Co–TiO_2 and TiO_{2-x}–$Co_{1-y}O$ systems [3-6] the position on the invariability of the molar volume of the system is justified by the fact that the formation of substitutional solid solutions based on cobalt and titanium oxides occurs at the grain boundaries in the presence of sufficient free volume. It is also justified by the fact that only grain boundary metal atoms, constituting an insignificant fraction of the total oxygen-bound metal in the corresponding oxide, are involved in the solid-phase reaction.

The aim of this study was determination of the values of the parameters characterizing the process of reactive interdiffusion and phase formation in a thin film two-layer system of TiO_{2-x}-$Co_{1-y}O$ oxides, based on the numerical analysis of the distribution of the concentrations of the metals within the model of reactive interdiffusion [6].

2. Experimental

A two-layer system of non-stoichiometric oxides was obtained by the method described in the study [6]. Magnetron-assisted sputtering of cobalt (UVN-75M unit) was carried out on single-crystalline silicon KEF 4.5 (100) wafers at the following modes: discharge voltage 420 V, current 0.5 A, rate 1.13 nm/s. The thickness of the Co films was set by the sputtering time and was ~ 100 nm. Subsequent thermal oxidation (in order to obtain cobalt oxide CoO films) was carried out in a quartz reactor of a resistive heating furnace in an oxygen flow with a flow rate of 30 l/h at T = 673 K for 30 min. Metallic titanium with the thickness of ~ 50 nm was deposited onto a layer of formed cobalt oxide by magnetron sputtering in the following modes: discharge voltage 380 V, current 0.3 A, rate 2.3 nm/s. Vacuum annealing was carried out at residual pressure of R_{res} = 2.7 10^{-3} Pa in the temperature range of 773–1073 K for 30 min. The distribution of the concentrations of the components over the depth of the system were determined by the Rutherford backscattering

spectrometry (RBS) method on proton and single-charged helium ion beams – 4 of electrostatic generator EG-5 in the Laboratory of Nuclear Physics of the Joint Institute for Nuclear Research.

The microstructure and thickness were determined by scanning electron microscopy (SEM) on cleavages of samples using a JSM-6510 LV scanning electron microscope with a resolution in a high vacuum of 4 nm. The phase composition of the two-layer film system was analysed by X-ray phase analysis (XRD) using a DRON 4-07 diffractometer in an automatic mode with an interval of 0.1° and a time of exposure at each point of 1 s (CoK_λ- radiation, λ = 1.79021 Å). The obtained diffraction patterns were interpreted using the diffraction files of the JCPDS.

3. Simulation results

As a result of vacuum annealing, non-stoichiometric titanium and cobalt oxides were formed. In titanium oxide, the main defects are interstitial titanium ions, in CoO at low oxygen pressures, the dominant defect is cobalt ions in interstices [11].

In the model [6], it is assumed that, under non-stoichiometric conditions, in each of the oxides of the thin film two-layer TiO_{2-x}–$Co_{1-y}O$ system, metal exists in two states. The first being partly in a stationary state bound to oxygen in the corresponding oxide state and the second being partly in a free state (in the form of interstitial Co^{2+} and Ti^{4+} metal cations) [11], capable of diffusion migration. With vacuum annealing of the system of TiO_{2-x}–$Co_{1-y}O$ oxides, titanium and cobalt are formed at the grain boundaries of oxides as a result of interdiffusion of interstitial cations of one metal into a film of another metal oxide with irreversible capture on intergrain traps. Cation-capture reactions ((1) and (2) in [6]) provide the replacement of one cation by another, and the released cation passes into a free state and can participate in the interdiffusion process. The total concentration of each of the metals is the sum of the concentration of free interstitial cations, metal bound to the oxygen in the composition of traps at the grain boundaries of its oxide and the concentration of the oxygen-bound metal in the traps in the oxide phase of another metal.

The modelling method as a part of the complex empirical research methodology allows determining the values of the characteristic parameters of the process by numerical analysis of the experimentally obtained distribution of concentrations of components within the model. The parameters of the model for reactive interdiffusion in a thin film system of TiO_{2-x}–$Co_{1-y}O$ oxides [6], using the mathematical form of Darken's theory [7], include:

– individual titanium D_{Ti} and cobalt D_{Co} diffusion coefficients,

– the proportion of free metal in each phase of the system: titanium r_1 (in TiO_{2-x}) and cobalt r_2 (in $Co_{1-y}O$), which is a quantitative measure of the non-stoichiometry of the oxide phases of the system, as well as

– reaction rate constants ((1) and (2) in [6]) k_1 and k_2 capture of titanium and cobalt on grain boundary traps in the $Co_{1-y}O$ and TiO_{2-x} phases, respectively.

The level of non-stoichiometry of oxides depends on the method of their preparation, temperature and composition of the annealing medium [11]. In the literature, there is a significant variation in the values of non-stoichiometry of TiO_2 and CoO oxides under conditions of low oxygen pressure and at high annealing temperatures from 0.001 to 0.5 at% [12].

For the studied oxides in the thin film state, there are no data on their non-stoichiometry; therefore, we will assume the same level of non-stoichiometry for both phases of the TiO_{2-x}–$Co_{1-y}O$ system: for titanium and cobalt $r = r_1 = r_2 = 0.01$.

The example of calculation of the distributions of relative concentrations C of titanium (*1–5*) and cobalt (*1′–5′*) along the depth of the TiO_{2-x}–$Co_{1-y}O$ system in the absence of chemical transformations, depending on its non-stoichiometry level r is shown in Fig. 1. As can be seen from Fig. 1, the intensity of mass transfer in the studied system depends significantly on the value r, determining the concentration level of mobile components. This dependence affects the values of the individual diffusion coefficients of titanium and cobalt, determined by numerical analysis of experimental distribution of concentrations within the model [6].

The values of the individual diffusion coefficients of titanium and cobalt in the TiO_{2-x}–$Co_{1-y}O$ system were determined by numerical analysis of the experimental distribution of concentrations of the components within the model.

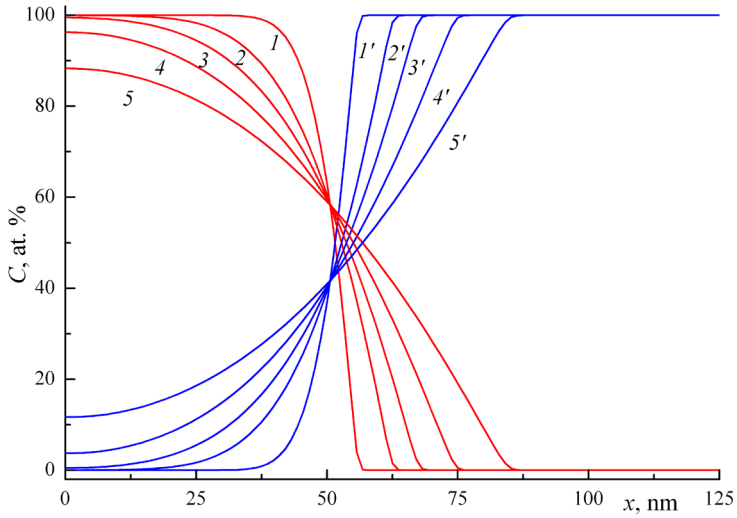

Fig. 1. Depth distribution of the relative concentrations of *C* of titanium (*1*–*5*) and cobalt (*1′*-*5′*) depending on the level of non-stoichiometry *r* of TiO_{2-x}–$Co_{1-y}O$ systems. Calculation at $r = r_1 = r_2$, $k_1 = k_2 = 0$, $D_{Co} = 1.0 \cdot 10^{-13}$ cm²/s; $D_{Ti} = 1.0 \cdot 10^{-15}$ cm²/s and with an annealing time of 30 min. Free metal fraction *r*: *1*, *1′* – 0.001; *2*, *2′* – 0.005; *3*, *3′* – 0.01; *4*, *4′* – 0.02; *5*, *5′* – 0.04

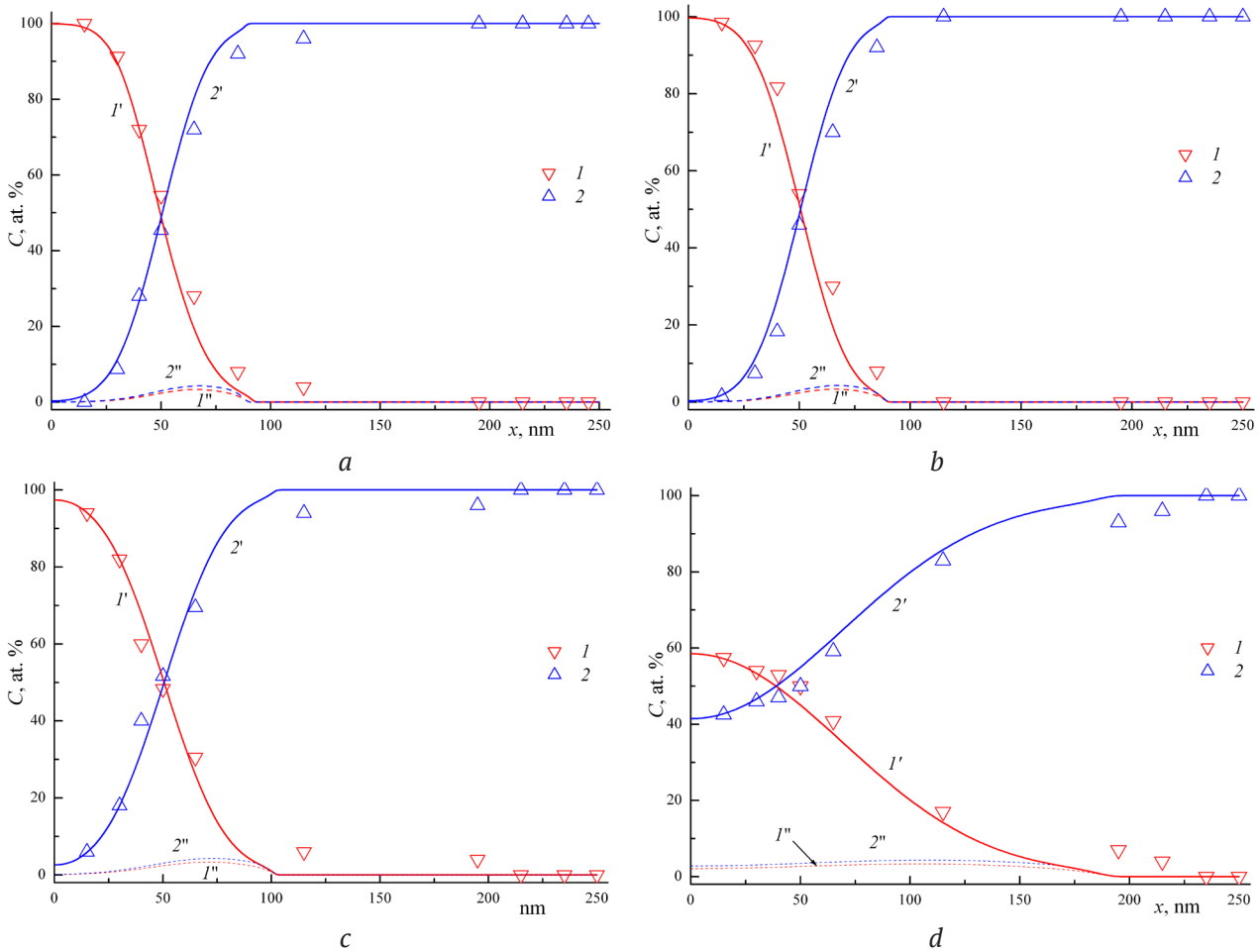

Fig. 2. Depth distributions of the relative total concentrations *C* (*1*, *1′*) and oxygen-bound metals (*2*, *2′*) in the TiO_{2-x}–$Co_{1-y}O$ system: titanium trapped in the cobalt oxide $Co_{1-y}O$ phase (*1′*) and cobalt trapped in the titanium oxide TiO_{2-x} phase (*2′*). Annealing time was 30 min, temperature: 773 K (*a*); 873 K (*b*); 973 K (c); 1073 K (*d*). Points – experiment (RBS method), curves – calculation at D_{Co} and D_{Ti} values from Fig. 4 (points 1, 2)

The distribution of concentrations of titanium and cobalt over the depth of the TiO_{2-x}–$Co_{1-y}O$ system obtained by the RBS method in comparison with the results of modelling of the total concentration of metals and its part captured by traps in the phases of titanium and cobalt oxides are shown in Fig. 2 a-d. The distributions of the latter characterize the region of phase formation of cobalt and titanium complex oxides. As can be seen from Fig. 2, the extension of this region increases with an increase in the vacuum annealing temperature and at 1073 K it becomes comparable with the total thickness of the film system (Fig. 2d). Thus, the process of phase formation does not occur at the interface, but has a character distributed over depth.

The evolution of the phase composition of the studied system during vacuum annealing, determined by the XRD method is shown in Fig. 3. After magnetron sputtering of titanium metal on the cobalt oxide layer (Fig. 3, curve *1*), cobalt oxides phases were revealed in the film: cubic CoO modification with lattice parameters: $a = 4.240$ Å (space group *Fm3m*) [JCPDS Cardno. 01-075-0418] and Co_3O_4 with a face-centred cubic lattice of a spinel structure (space group *Fd3m*) with lattice parameters: $a = 8.065$ Å. The diffraction pattern contains low-intensity reflections of titanium oxide TiO_2 in the tetragonal structure of rutile (space group *P42/mnm*), lattice parameters: $a = b = 4.5890$ Å, $c = 2.9540$ Å [JCPDS Cardno. 01-073-1765]. The micrograph of the cleavage of the film system shows

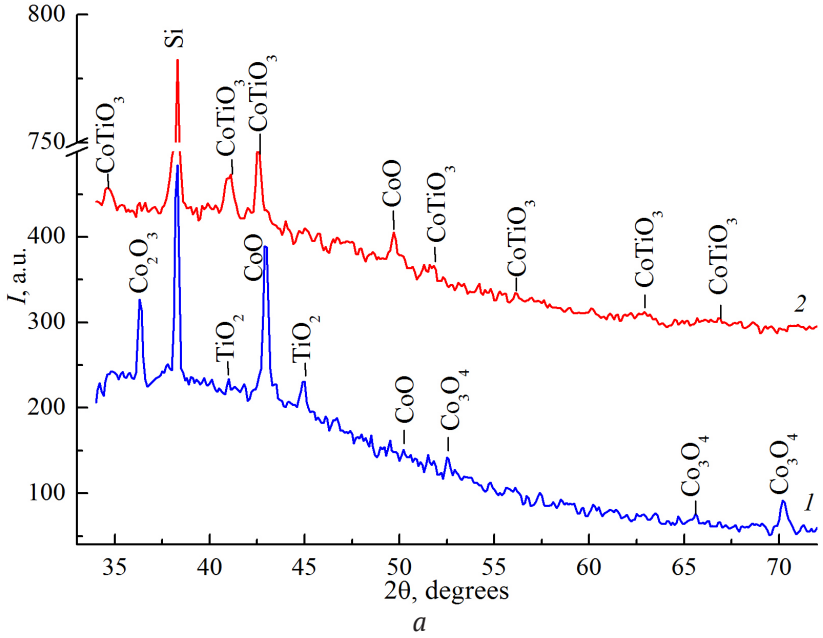

a

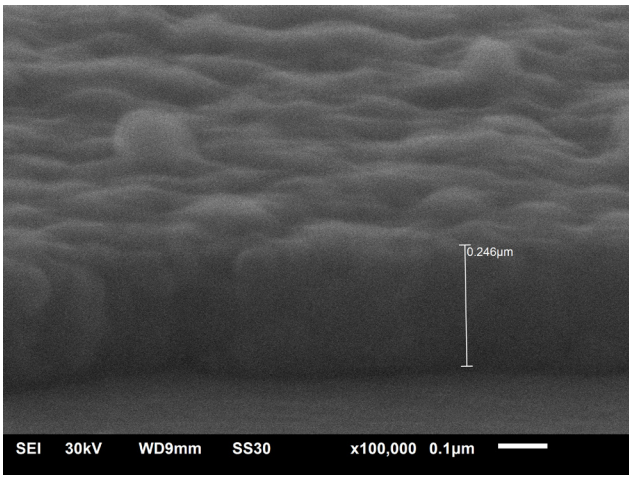

b

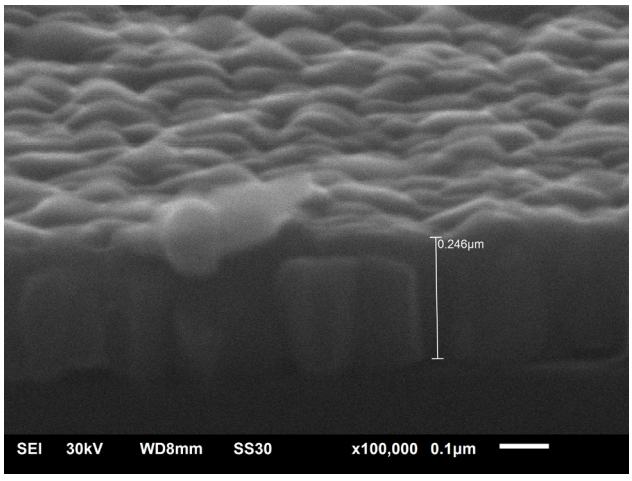

c

Fig. 3. Diffraction patterns (a) and micrographs of the TiO_{2-x}–$Co_{1-y}O$ film cleavage after magnetron sputtering (b) and vacuum annealing at $T = 1073$ K (c)

two layers: the lower cobalt oxide layer with a thickness of ~ 200 nm and the upper titanium oxide layer with a thickness of ~ 40 nm (Fig. 3 a). After vacuum annealing at T = 1073 K (Fig. 3, curve *2*) as a result of the interaction of CoO and TiO_2 the complex oxide $CoTiO_3$ is formed rhombohedral modification (space group *R-3 (148)*, with lattice parameters: $a = b$ = 5.044 Å, c = 13.961 Å [JCPDS Cardno. 00-001-1040]. A homogeneous film with a thickness of ~ 246 nm, which remained unchanged during annealing, can be seen on a micrograph of the cleavage of the film in Fig. 3 b.

The temperature dependence of the individual diffusion coefficients of cobalt and titanium is shown in Fig. 4 (points *1* and *2* for cobalt and titanium, respectively). In the temperature range of 773–1073 K, they vary within $D_{Co} = 1.75 \cdot 10^{-14} \div 1.04 \cdot 10^{-12}$ cm^2/s, $D_{Ti} = 1.25 \cdot 10^{-15} \div 4.5 \cdot 10^{-15}$ cm^2/s. At these values of the parameters, a good correspondence was obtained between the experimental distributions (points) to the calculated ones for the total titanium (curves *1*) and cobalt (curves *2′*) concentrations (Fig. 2 *a-d*) with unchanged values of $k_1 = 1.10^{-21}$ cm^3/s $k_2 = 1.10^{-25}$ cm^3/s, $r_1 = r_2 = 0.01$.

The approximation of the temperature dependences in Fig. 3 by the Arrhenius equation provides the individual diffusion coefficient of cobalt in the TiO_{2-x}–$Co_{1-y}O$ film system:

$$D_{Co} = 5.1\ 10^{-8}\mathrm{Exp}(-1.0\ \mathrm{eV}/(kT))\ \mathrm{cm}^2/\mathrm{s} \quad (1)$$

and titanium

$$D_{Ti} = 1.38\ 10^{-13}\mathrm{Exp}(-0.31\ \mathrm{eV}/(kT))\ \mathrm{cm}^2/\mathrm{s} \quad (2)$$

As can be seen from Fig. 4, values of D_{Co} and D_{Ti} are close to the values of the individual diffusion coefficients of titanium and cobalt in the Co–TiO_2 metal-oxide system obtained by numerically analysing the distributions of the concentrations (the secondary-ion mass spectrometry method) using the deep reactive interdiffusion model, implementing the same approach [4]. The higher values of the individual diffusion coefficient determined for cobalt in comparison with the results of the study [4] are explained by different methods for determining the distribution of the concentrations, formation methods, and the difference in the level of non-stoichiometry of the studied Co–TiO_2 and TiO_{2-x}–$Co_{1-y}O$ systems.

4. Conclusions

We showed the possibility of using the mathematical form of Darken's theory [7] for the description of reactive interdiffusion in non-stoichiometric polycrystalline film oxide systems with limited solubility.

The reactive interdiffusion model [6] provides a good description of the experimental distribution of the concentrations of titanium and

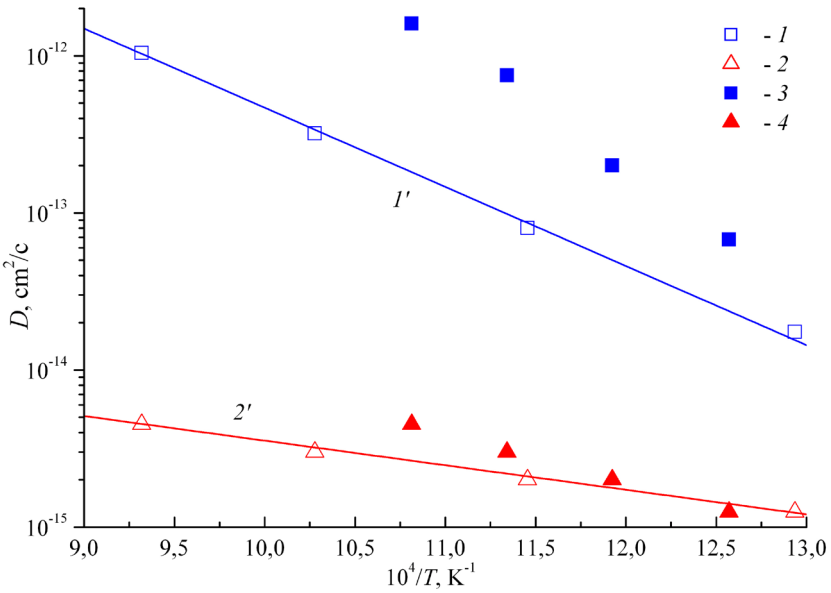

Fig. 4. Temperature dependence of individual diffusion coefficients of metals in TiO_{2-x}–$Co_{1-y}O$ and Co–TiO_2 film systems. The points are the results of numerical analysis for cobalt (*1, 3*) and titanium (*2, 4*); curves *1′, 2′* – approximation by the Arrhenius equation for cobalt (1) and titanium (2), (*3, 4*) – results of the study [4]

cobalt over the depth of a two-layer film system of non-stoichiometric TiO_{2-x}–$Co_{1-y}O$ oxides during vacuum annealing in the temperature range of 773–1073 K.

The values of individual diffusion coefficients (temperature dependences (1) and (2)), characterizing the process of reactive interdiffusion and phase formation in a thin-film two-layer system of TiO_{2-x}–$Co_{1-y}O$ oxides have been determined.

The extension of the region of phase formation of complex cobalt and titanium oxides increases with an increase in the vacuum annealing temperature and at 1073 K it becomes comparable to the total thickness of the film system.

Individual diffusion coefficients of cobalt and titanium in the TiO_{2-x}–$Co_{1-y}O$ system determined by numerical analysis and the level of non-stoichiometry are in good agreement with the literature data [13–15]. In the study [16], for the annealing of nanocrystalline TiO_2 films in an Ar atmosphere, the grain boundary diffusion coefficient was $1.04\ 10^{-13}$ cm^2/s at T = 673 K. The scatter in the values of the grain boundary diffusion coefficient is assumed to be associated with structural changes at the grain boundaries and the formation of an amorphous grain boundary phase [17, 18]. Grain boundary complexes were observed in the WO_3 and TiO_2 system, doped with CuO [19, 20]. These grain boundary phases are not numerous, have a nanometer width, and therefore are not visible in microscopes with a low resolution. As a result, the determined coefficients of grain boundary diffusion at different temperatures did not correspond to the values determined for single crystals.

The model allows predicting the distribution of concentrations of components over the depth of multilayer non-stoichiometric systems, in which reactive interdiffusion is possible.

Conflict of interests

The authors declare that they have no known competing financial interests or personal relationships that could have influenced the work reported in this paper.

References

1. Chebotin V. N. *Fizicheskaya khimiya tverdogo tela* [Physical chemistry of a solid state]. Moscow: Khimiya Publ.; 1982. 320 p. (in Russ.)

2. Tretyakov Yu. D. *Tverdofaznye reaktsii* [Solid phase reactions]. Moscow: Khimiya Publ.; 1978. 360 p. (in Russ.)

3. Afonin N. N., Logacheva V. A. Interdiffusion and phase formation in the Fe–TiO_2 thin-film system. *Semiconductors*. 2017;51(10): 1300–1305. DOI: https://doi.org/10.1134/S1063782617100025

4. Afonin N. N., Logacheva V. A. Cobalt modification of thin rutile films magnetron-sputtered in vacuum technical. *Technical Physics*, 2018;63(4): 605–611. DOI: https://doi.org/10.1134/S1063784218040023

5. Afonin N. N., Logacheva V. A. Modeling of the reaction interdiffusion in the polycrystalline systems with limited component solubility. *Industrial Laboratory. Diagnostics of Materials*. 2019;85(9): 35–41. DOI: https://doi.org/10.26896/1028-6861-2019-85-9-35-41diffusion (In Russ., abstract in Eng.)

6. Afonin N. N., Logacheva V. A. Modeling of interdiffusion and phase formation in the thin-film two-layer system of polycrystalline oxides titanium and cobalt. *Kondensirovannye sredy i mezhfaznye granitsy = Condensed Matter and Interphases*. 2019;21(3): 358–365. DOI: https://doi.org/10.17308/kcmf.2019.21/1157 (In Russ., abstract in Eng.)

7. Darken L. S. Diffusion, mobility and their interrelation through free energy in binary metallic systems. *Trans. AMIE*.1948;175: 184–190.

8. Gurov K. P., Kartashkin B. A., Ugaste Yu. E. *Vzaimnaya diffuziya v mnogofaznykh metallicheskikh sistemakh* [Interdiffusion in multiphase metallic systems]. Moscow: Nauka Publ.; 1981. 350 p. (In Russ.)

9. Kulkarni N. S., Bruce Warmack R. J., Radhakrishnan B., Hunter J. L., Sohn Y., Coffey K. R., … Belova I. V. Overview of SIMS-based experimental studies of tracer diffusion in solids and application to Mg self-diffusion. *Journal of Phase Equilibria and Diffusion*. 2014;35(6): 762–778. DOI: https://doi.org/10.1007/s11669-014-0344-4

10. Aleksandrov O. V., Kozlovski V. V. Simulation of interaction between nickel and silicon carbide during the formation of ohmic contacts. *Semiconductors*. 2009;43(7): 885–891. DOI: https://doi.org/10.1134/S1063782609070100

11. Kofstad P. *Nonstoichiometry, diffusion, and electrical conductivity in binary metal oxides*. Wiley-Interscience; 1972. 382 p.

12. Bak T., Nowotny J., Rekas M., Sorrell C. C. Defect chemistry and semiconducting properties of titanium dioxide: II. Defect diagrams. *Journal of Physics and Chemistry of Solids*. 2003;64(7): 1057–1067. DOI: https://doi.org/10.1016/s0022-3697(02)00480-8

13. Iddir H., Öğüt,S., Zapol P., Browning N. D. Diffusion mechanisms of native point defects in rutile TiO_2: *Ab initio* total-energy calculations. *Physical Review B*. 2007;75(7): DOI: https://doi.org/10.1103/physrevb.75.073203

14. Hoshino K., Peterson N. L., Wiley C. L. Diffusion and point defects in TiO_{2-x}. *Journal of Physics and*

Chemistry of Solids. 1985;46(12): 1397-1411. DOI: https://doi.org/10.1016/0022-3697(85)90079-4

15. Fiebig J., Divinski S., Rösner H., Estrin Y., Wilde G. Diffusion of Ag and Co in ultrafine-grained α-Ti deformed by equal channel angular pressing. *Journal of Applied Physics*. 2011;110(8): 083514. DOI: https://doi.org/10.1063/1.3650230

16. Straumal P. B. Stakhanova S. V., Wilde G., Divinski S. V. ^{44}Ti self-diffusion in nanocrystalline thin TiO_2 films produced by a low temperature wet chemical process. *Scripta Materialia.* 2018;149: 31–35. DOI: https://doi.org/10.1016/j.scriptamat.2018.01.022

17. Patrick R. Cantwell, Ming Tang, Shen J. Dillon, Jian Luo, Gregory S. Rohrer, Martin P. Harmer. Grain boundary complexions. *Acta Materialia*. 2014;62: 1–48. DOI: https://doi.org/10.1016/j.actamat.2013.07.037

18. Dillon S. J., Tang M., Carter W. C., Harmer M. P. Complexion: A new concept for kinetic engineering in materials science. *Acta Materialia*, 2007;55(18): 6208–6218. DOI: https://doi.org/10.1016/j.actamat.2007.07.029

19. Grain boundary complexion transitions in WO_3- and CuO-doped TiO_2 bicrystals. *Acta Materialia*. 2013;61(5); 1691–1704. DOI: https://doi.org/10.1016/j.actamat.2012.11.044

20. Nie J., Chan J. M., Qin M., Zhou N., Luo J. Liquid-like grain boundary complexion and sub-eutectic activated sintering in CuO-doped TiO_2. *Acta Materialia*. 2017;130: 329–338. DOI: https://doi.org/10.1016/j.actamat.2017.03.037

Information about the authors

Nikolay N. Afonin, DSc in Chemistry, Research Fellow, Professor at the Department of Science and Technology Studies, Voronezh State Pedagogical University, Voronezh, Russian Federation; e-mail**:** nafonin@vspu.ac.ru. ORCID iD: https://orcid.org/0000-0002-9163-744X.

Vera A. Logachova, PhD in Chemistry, Research Fellow at the Department of General and Inorganic Chemistry, Voronezh State University, Voronezh, Russian Federation; e-mail: kcmf@main.vsu.ru. ORCID iD: https://orcid.org/0000-0002-2296-8069.

All authors have read and approved the final manuscript.

Translated by Valentina Mittova
Edited and proofread by Simon Cox

Condensed Matter and Interphases
(Kondensirovannye sredy i mezhfaznye granitsy)

Original articles

DOI: https://doi.org/10.17308/kcmf.2020.22/3114
Received 20 November 2020
Accepted 15 December 2020
Published online 25 December 2020

ISSN 1606-867X
eISSN 2687-0711

Investigation of the Magnetic Properties of Amorphous Multilayer Nanostructures $[(CoFeB)_{60}C_{40}/SiO_2]_{200}$ and $[(CoFeB)_{34}(SiO_2)_{66}/C]_{46}$ by the Transversal Kerr Effect

©2020 E. A. Ganshina[a], V. V. Garshin[a], N. S. Builov[b], N. N. Zubar[a], A. V. Sitnikov[c], E. P. Domashevskaya[b*]

[a]*Lomonosov Moscow State University,*
GSP-1, Leninskie Gory, Moscow 119991, Russian Federation

[b]*Voronezh State University,*
1 Universitetskaya pl., Voronezh 394018, Russian Federation

[c]*Voronezh State Technical University,*
Moskovsky pr., 14, Voronezh 394026, Russian Federation

Abstract

Magnetic properties in amorphous multilayer nanostructures $[(CoFeB)_{60}C_{40}/SiO_2]_{200}$ and $[(CoFeB)_{34}(SiO_2)_{66}/C]_{46}$ with different content of the CoFeB magnetic alloy in metal-composite layers and inverse location of non-metallic phases C and SiO_2 in composite layers or in interlayers, were investigated by magneto-optical methods in the transversal Kerr effect (TKE) geometry.

Using the spectral and field dependences of the transversal Kerr effect TKE, it has been established that in the samples of both magnetic multilayer nanostructures (MLNS) the magneto-optical response and magnetic order are determined by the phase composition of the composite layers.

In samples of MLNS $[(CoFeB)_{60}C_{40}/SiO_2]_{200}$ with a post-percolation content of metal clusters in metal-composite layers, the maximum of absolute TKE values decrease by about 2.5 times compared with the initial amorphous $Co_{40}Fe_{40}B_{20}$ alloy, while the field dependences of TKE in samples of this MLNS has features that are characteristic of soft ferromagnets.

In samples of MLNS $[(CoFeB)_{34}(SiO_2)_{66}/C]_{46}$ with a pre-percolation content of metal clusters in the oxide SiO_{2-x} matrix of metal-composite layers, the TKE spectral dependences fundamentally differed from the TKE of the initial amorphous $Co_{40}Fe_{40}B_{20}$ alloy both in shape and sign. The field dependences of the TKE in the samples of this MLN were linear, characteristic of superparamagnets.

Keywords: amorphous magnetic multilayer nanostructures, metal-composite layers, nonmagnetic interlayers, magnetic clusters of CoFeB, transversal Kerr effect TKE, spectral dependences of TKE, field dependences of TKE, soft ferromagnets, superparamagnets.

Funding: This study was partially financially supported by the Ministry of Science and Higher Education of the Russian Federation in the framework of the state order to higher education institutions in the sphere of scientific research for years 2020-2022, project No. FZGU-2020-0036.

For citation: Gan'shina E. A., Garshin V. V., Builov N. S., Zubar N. N., Sitnikov A. V., Domashevskaya E. P. Investigation of magnetic properties of amorphous multilayer nanostructures $[(CoFeB)_{60}C_{40}/SiO_2]_{200}$ and $[(CoFeB)_{34}(SiO_2)_{66}/C]_{46}$ by the transversal Kerr effect. *Kondensirovannye sredy i mezhfaznye granitsy = Condensed Matter and Interphases*. 2020;22(4): 438–445. DOI: https://doi.org/10.17308/kcmf.2020.22/3114

Для цитирования: Ганьшина Е. А., Гаршин В. В., Буйло Н. С., Зубарь Н. Н., Ситников А. В., Домашевская Э. П. Исследование магнитных свойств аморфных многослойных наноструктур $[(CoFeB)_{60}C_{40}/SiO_2]_{200}$ и$[(CoFeB)_{34}(SiO_2)_{66}/C]_{46}$ с помощью экваториального эффекта Керра. *Конденсированные среды и межфазные границы*. 2020; 22(4): 438–445. DOI: https://doi.org/10.17308/kcmf.2020.22/3114

✉ Evelina P. Domashevskaya e-mail: ftt@phys.vsu.ru

1. Introduction

Currently, one of the most dynamically developing areas of modern solid-state physics is the study of fundamental properties and practical application of artificially created nanomedia with a heterogeneity scale of 1–10 nm.

From a fundamental point of view, nanogranular media turned out to be interesting objects with tunnelling electron transport, expressed size effects and complex magnetic properties due to the single-domain nature of ferromagnetic nanogranules isolated from each other by a dielectric [1-5]. It is possible to obtain magnetic structures with excellent prospects for use in the field of high frequency and microwave frequencies of electromagnetic radiation when transition metals (Fe, Co, Ni) or their alloys are used as one of the phases.

The object of intensive experimental and theoretical studies is the question of the effect of the composition and microstructure of nanomaterials formed in the process of self-organization of atoms during their production on the magnetic, magneto-optical, and magnetotransport properties of nanoheterostructures. Despite the large number of studies in this area, there is still no clarity in understanding the processes accompanying the structural rearrangement of matter, since it is difficult to predict the properties of films, in which the interaction of nanoparticles with each other, with the matrix, and with the substrate plays a significant role, with a huge influence of the size and surface effects inherent in nanoparticles/clusters, their boundaries and surfaces.

In our previous studies for the investigation of the atomic structure of amorphous multilayer nanostructures (MLNS) $[(CoFeB)_{60}C_{40}/SiO_2]_{200}$ and $[(CoFeB)_{34}(SiO_2)_{66}/C]_{46}$ with a different number of bilayers, a different content of metal, dielectric SiO_2 and the carbon component and the inverce location of the last two in metal-composite layers or in interlayers, we used non-destructive methods for analysing interfaces, short-range order, and electronic structure [6–9]. Among them are X-ray diffractometry (XRD), X-ray reflectivity (XRR), ultrasoft X-ray emission spectroscopy (USXES), X-ray absorption near edges structure (XANES) and extending X-ray absorption fine structure (EXAFS) [6–9].

According to the results of these studies in the MLNS $[(CoFeB)_{60}C_{40}/SiO_2]_{200}$ with SiO_2 interlayers a better preservation of the planarity of the interface boundaries between metal-composite layers and SiO_2 interlayers, than in the MLNS $[(CoFeB)_{34}(SiO_2)_{66}/C]_{46}$ with carbon interlayers, was found. Also, a better preservation of the integrity of the magnetic granules of the original CoFeB alloy with the Me-C and B-C bonds at the interphase boundaries inside the metal-composite layers was revealed. As a result, in these MLNS a noticeable mixing of metal-composite layers and SiO_2 interlayers did not occur, and the interfaces remain planar [6–8].

In the another MLNS $[(CoFeB)_{34}(SiO_2)_{66}/C]_{46}$ with silicon dioxide in metal-composite layers and carbon interlayers a different situation was observed. The significant smearing of interface boundaries of metal-composite layer/carbon interlayer detected in it was due to the significant interaction of all components of the complex nanostructure with the formation of Me-O (first of all, Fe-O) and B-O bonds with oxygen of SiO_2 matrix at the interphase boundaries inside the metal-composite layers. As a result, the size of the granules of the initial alloy significantly decreased to clusters with lower coordination numbers, and the whole MLNS was more homogeneous [6–9].

It is well known that magneto-optical (MO) methods provide unique information about magnetic and electronic structure of new complex nanomaterials, and that is why they are effective and informative [10]. The MO properties of amorphous metal-dielectric nanocomposites depend on the phase composition and structure of the metal and dielectric phases, on the volumetric content of the magnetic component and on the shape and size of magnetic granules [11–14].

In amorphous metal-dielectric nanocomposites with oxide matrices, an increase in the MO response was observed for concentrations in the percolation region [13, 14].

For pre-percolation systems ($x < x_{per}$) a superparamagnetic state is characteristic, due to the presence of nanoscale magnetic inclusions located in a nonmagnetic medium [15–19]. In this case, a prerequisite for the existence of superparamagnetism is the absence of interaction between ferromagnetic nanogranules. With an increase in the relative volume of the

ferromagnetic phase, the distances between the granules decrease up to their contact, and as a result of the exchange interaction between the magnetic moments of the atoms of different granules a correlation of the magnetic moments of the structure as a whole arises. This determines the ferromagnetic nature of the heterogeneous object.

The form of the spectral TKE dependences significantly changed upon transition to layer-by-layer deposited nanocomposites [20]. The change in the field dependences of the TKE of the samples deposited layer-by-layer had the same tendency as in the bulk granular nanocomposite – the evolution of the magnetization curves from superparamagnetic to ferromagnetic occurred with an increase in the concentration of *x*. The percolation threshold in layer-by-layer deposited composites shifts to the region of lower concentrations of the ferromagnetic phase.

The MO properties of nanostructures were significantly affected not only by the concentration of the metal phase, but also by the thickness of the composite layers. The thickness of the films is set by the rotation rate of the substrate around the sputtered targets [20, 21]. Studies of the effect of nanocomposite manufacturing technology on their MO properties showed that the system with the thinnest layers should have a percolation threshold at the lowest value of *x* of all the systems studied, which was observed experimentally [20].

A comparison of the MO properties of nanocomposites in oxide matrices and a carbon matrix showed that the form of the spectral and field TKE dependences depends on the type of matrix and strongly differs for SiO_2 and C matrices. This was due to the peculiarities of the formation of nanocomposites with a carbon matrix [22].

The aim of this study was to obtain information about the magnetic properties in amorphous MLNS $[(CoFeB)_{60}C_{40}/SiO_2]_{200}$ and $[(CoFeB)_{34}(SiO_2)_{66}/C]_{46}$ with a different content of metal, dielectric SiO_2 and/or C components and the inverse location of the last two in metal-composite layers or in interlayers by studying the transversal Kerr effect TKE, as well as the influence of the structural features of the MLNS on these properties.

2. Experimental

MLNS with different composition of metal-composite layers and different interlayers $[(CoFeB)_{60}C_{40}/SiO_2]_{200}$ and $[(CoFeB)_{34}(SiO_2)_{66}/C]_{46}$ were obtained by the ion-beam sputtering method (with a layer/interlayer thickness gradient) onto a sitall substrate from two different targets, one of which consisted of a plate of an amorphous metal alloy $Co_{40}Fe_{40}B_{20}$ with carbon or quartz inserts, located at different distances from each other. For the production of the thickness gradient of the metal-composite layers and non-metallic interlayers between the target and the substrates, a *V*-shaped screen was placed. The deposition was carried out in an Ar atmosphere at a pressure of $5 \cdot 10^{-4}$ Torr [17–20].

The transversal Kerr effect which consists in changing the intensity of linearly p-polarized light reflected by a sample magnetized perpendicular to the plane of light incidence was used for the investigation of the magneto-optical properties of the MLNS $[(CoFeB)_{60}C_{40}/SiO_2]_{200}$ and $[(CoFeB)_{34}(SiO_2)_{66}/C]_{46}$ [22–24].

The ratio (δ) of the difference in the intensities of the light reflected by the sample in the presence (I) and absence of a magnetic field (I_0), respectively, measured in the experiment, to the intensity of light I_0 determines the value and sign of the TKE:

$$\delta = (I - I_0) / I_0 = \Delta I / I_0. \quad (1)$$

The spectral and field dependences of the transversal Kerr effect were measured using an automated MO spectrometer in the energy range of incident light quanta E from 0.5 to 4 eV. The amplitude of the applied alternating magnetic field reached 3 kOe. For the registration of the signal, a dynamic method was applied, which allows measuring the relative change in light intensity up to 10^{-5}. In this case, the measurement error did not exceed 5%. The measurements were carried out at room temperature.

3. Results and discussion

Table 1 shows the thicknesses (in nanometres) of bilayers equal to the sum of the thicknesses of metal-composite layers and interlayers, nominal (calculated based on the geometry and deposition rate) and experimental (according to reflectometry data [7, 8]) for MLNS samples, obtained by ion-beam sputtering, in which the magneto-optical

Table 1. Nominal and experimental bilayer thicknesses (metal-composite layer + interlayer) for MLNS samples of two types (nm)

	$[(CoFeB)_{60}C_{40}/SiO_2]_{200}$			$[(CoFeB)_{34}(SiO_2)_{66}/C]_{46}$		
Sample numbers	1	2	3	23	33	43
Metal-composite layer	3.3	4.0	4.6	5.9	6.4	6.5
Interlayer	1.7	2.0	2.4	1.2	1.4	1.6
Nominal bilayer thickness	5.0	6.0	7.0	7.1	7.8	8.1
Bilayer thickness according to reflectometry data [7, 8]	5.44	6.44	6.57	7.35	8.15	8.43

properties were studied. The studied samples were numbered in accordance with the increase in bilayer thicknesses and overall thicknesses: *1, 2, 3* for MLNS $[(CoFeB)_{60}C_{40}/SiO_2]_{200}$ and *23, 33, 43* for MLNS $[(CoFeB)_{34}(SiO_2)_{66}/C]_{46}$.

Figure 1 shows the obtained dependences of transversal the Kerr effect TKE on the energy of light quanta for samples of two MLNS $[(CoFeB)_{60}C_{40}/SiO_2]_{200}$ and $[(CoFeB)_{34}(SiO_2)_{66}/C]_{46}$ with similar average values of bilayer thicknesses of about 6–8 nm, but with different numbers of bilayers 200 and 46 and, therefore, different total MLNS thicknesses.

Spectral dependences of two MLNS $[(CoFeB)_{60}C_{40}/SiO_2]_{200}$ and $[(CoFeB)_{34}(SiO_2)_{66}/C]_{46}$ shown in Fig.1, demonstrated that the TKE in them is fundamentally different by sign. The maximum absolute values of TKE in the samples of both MLNS were approximately 2.5 times lower than in the film of the initial amorphous $Co_{40}Fe_{40}B_{20}$ alloy, to which corresponds the upper curve in Fig. 1. It should be noted that the general form and signs of the TKE spectral dependences in both MLNS corresponded to the TKE spectral curves from film composites of the same compositions $(CoFeB)_x(SiO_2)_{1-x}$ and $(CoFeB)_xC_{1-x}$ [23], obtained using the same unit as the studied MLNS.

As we stated above, using non-destructive X-ray analysis methods such as XRR, USXES, XANES and EXAFS, it was found [6–9] that in MLNS $[(CoFeB)_{60}C_{40}/SiO_2]_{200}$ with a high content of magnetic alloy (after the percolation threshold) and carbon in the metal-composite layers, but with oxide interlayers, not only the interfaces, but also the clusters of the initial amorphous CoFeB alloy (with the Me-C and B-C boundary bonds) were preserved, which correlates with the data of spectral TKE dependences and explains the similarity of the shapes and positive values of MLNS spectra and the initial alloy. However,

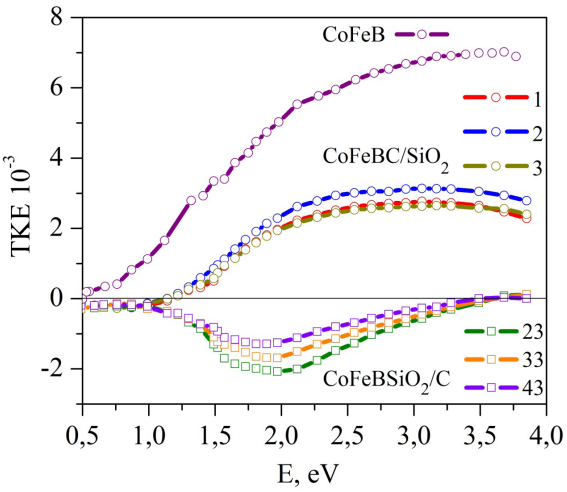

Fig. 1. Spectral dependences of TKE in amorphous samples with different thicknesses for MLNS $[(CoFeB)_{60}C_{40}/SiO_2]_{200}$ – *1*, *2* and *3*; for MLNS $[(CoFeB)_{34}(SiO_2)_{66}/C]_{46}$ – *23*, *33* and *43* and in the film of the amorphous alloy $Co_{40}Fe_{40}B_{20}$ (upper curve)

the influence of dielectric SiO_{2-x} interlayers and the carbon matrix surrounding metal clusters led to a decrease in the relative content of the metal phase in the total volume of the MLNS structure and, accordingly, to a decrease in the TKE modulus by almost 2.5 times (Fig. 1).

Using the same diagnostic methods in the MLNS $[(CoFeB)_{34}(SiO_2)_{66}/C]_{46}$ with significantly lower magnetic alloy content x = 34 at. % (up to the percolation threshold) and oxide matrix in the composite layers, a significant smearing of the planarity of the interfaces with the formation of oxides of 3*d*-metals, mostly iron oxides was revealed [7–9]. All this leads to a higher mixing of atoms of the metal-composite layers and interlayers, a decrease in the size of metal clusters, and a higher homogeneity of the entire MLNS as compared to the previous one. These circumstances can explain the negative spectral dependences of TKE in MLNS $[(CoFeB)_{34}(SiO_2)_{66}/C]_{46}$ in Fig. 1.

Moreover, it should be taken into account, that the same negative spectral TKE dependences were observed in all thin-film samples of composites of variable composition $(CoFeB)_x(SiO_2)_{1-x}$ [23], including the composition of composite layers of studied by us MLNS $[(CoFeB)_{34}(SiO_2)_{66}/C]_{46}$.

The fact that CoFeB composites with different nonmagnetic phases and MLNSs with the corresponding metal-composite layers have spectral dependences similar in general form and TKE of the same sign allows us to conclude that in both MLNSs the MO response and magnetic order are determined by the phase composition and electronic structure of the metal-composite layers.

Since the value of the TKE is proportional to the magnetization of the sample, based on the analysis of the TKE dependence on the magnitude of the applied magnetic field, the magnetic order realized in the sample can be determined.

Fig. 2 shows the field dependences of the TKE on the strength of the applied magnetic field for samples of two types MLNS with different thicknesses of bilayers, metal-composite layers and interlayers presented in Table 1.

Comparison of the results for MLNS of two types in Fig. 2 shows that the form of the field dependences of the TKE in MLNS $[(CoFeB)_{60}C_{40}/SiO_2]_{200}$ has features characteristic of ferromagnets. A sharp increase in the magnetization of all studied samples (*1, 2, 3*) to saturation magnetization indicates that the samples of this MLNS are magnetically soft materials with a coercive force not exceeding several Oe. A slight difference in the magnitude of the effect for samples (*1*, *2*, *3*) was revealed. These differences correlated with the thickness of the samples in a regular way; the effect increased with an increase in the thickness of the composite layers, i.e., with an increase in the volume of the ferromagnetic phase.

As can be seen in Fig. 2, TKE dependence on the magnitude of the field is linear, characteristic for materials with a superparamagnetic magnetization in MLNS $[(CoFeB)_{34}(SiO_2)_{66}/C]_{46}$ samples with SiO_2 in metal-composite layers and impaired interfaces [7-9]. Such a magnetic order is characteristic of nanostructures in the pre-percolation state with a low content of the ferromagnetic phase and small sizes of magnetic particles [11–13], which are the samples of this MLNS, containing along with metal clusters of small sizes, metal-oxide and oxy-boride clusters of transition metals. Decrease in the slope angle of the linear TKE(H) dependences (Fig. 2a) with increasing thickness of *23, 33, 43* MNS samples $[(CoFeB)_{34}(SiO_2)_{66}/C]_{46}$ was most probably associated with a change in the morphology (shape and size) and density of magnetic granules in the general structure of the MLNS.

For these MNLS, we observed that with an increase in the thickness of the metal-composite layers, the modulus of the TKE value decreases, and the highest negative effect of TKE was observed

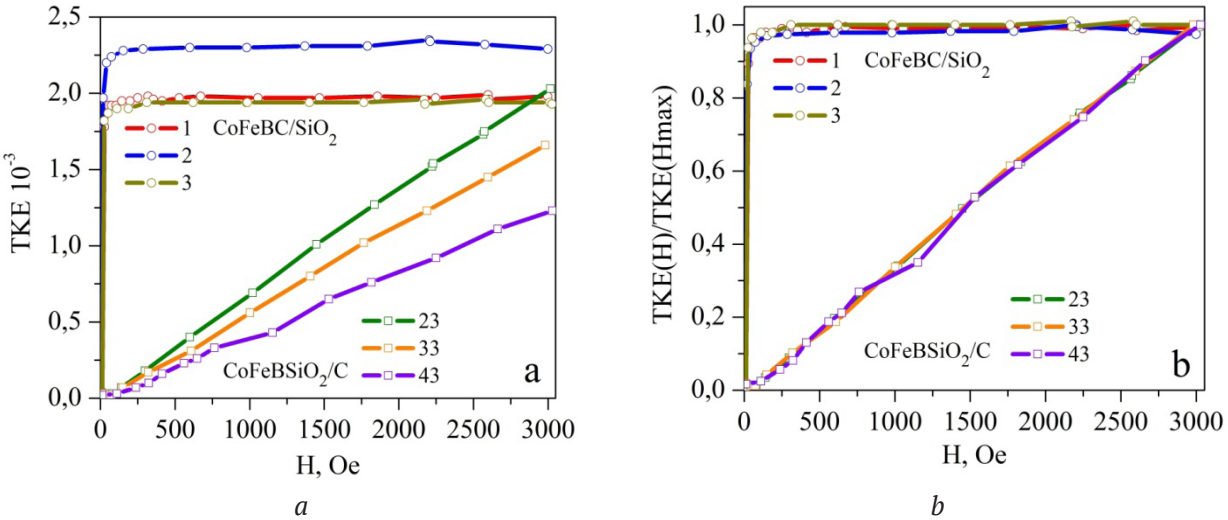

a *b*

Fig. 2. Field dependences of TKE (H) on the magnetic field strength for amorphous MLNS with different sample thicknesses: $[(CoFeB)_{60}C_{40}/SiO_2]_{200}$ – *1, 2, 3* and $[(CoFeB)_{34}(SiO_2)_{66}/C]_{46}$ – *23, 33, 43:* experimental (a) and normalized by the magnitude of the effect in the maximum field TKE(H)/TKE(H_{max}) (b)

for the MLNS with the smallest thickness of the metal-composite layers (curve *23* in Fig. 1). The thickness of the metal-composite layers affected the size and shape of the ferromagnetic granules, which, in turn, affected the MO properties.

As was shown in the study [20], the size of granules in layer-by-layer sprayed samples is smaller than the characteristic size in a bulk composite, and the probability of contact of granules with each other is higher at smaller sizes of the granules. For a system with thinner layers, the percolation threshold shifts to the region of lower concentrations of *x*, which should lead to an increase in the TKE in the region of a negative maximum, which was observed in our experiment for an MLNS with a SiO_2 matrix in composite layers.

TKE(H)/TKE(H_{max}) dependences normalized by the magnitude of the effect in the maximum field of the in Fig. 2b demonstrate complete coincidence of curves for samples with different thicknesses in each of the two MLNS $[(CoFeB)_{60}C_{40}/SiO_2]_{200}$ and $[(CoFeB)_{34}(SiO_2)_{66}/C]_{46}$. This fact indicates that a small change in thickness of metal-composite layers, interlayers and general thicknesses of MLNS does not affect the magnetic order realized in structures, ferromagnetic in MLNS $[(CoFeB)_{60}C_{40}/SiO_2]_{200}$ samples and superparamagnetic in MLNS $[(CoFeB)_{34}(SiO_2)_{66}/C]_{46}$ samples.

4. **Conclusion**

Comparative studies of magneto-optical effects in two MLNS $[(CoFeB)_{60}C_{40}/SiO_2]_{200}$ and $[(CoFeB)_{34}(SiO_2)_{66}/C]_{46}$ with different content of metal granules/clusters in metal-composite layers and inverse arrangement of non-metallic C and SiO_2 phases in metal-composite layers or interlayers were performed.

It was found that in both MLNS the magneto-optical response and magnetic order are determined by the phase composition of the metal-composite layers. The general form of the TKE spectral curves obtained from the MLNS corresponds to the dependences obtained for film composites deposited on a similar sitall substrate with a composition identical to the composite metal-containing layers of a multilayer structures.

The difference in the behaviour of the magneto-optical properties of two MLNS with different phase ratios: magnetic metal CoFeB, dielectric SiO_2 and carbon phases and inverse location of non-metallic phases in metal-composite layers or interlayers correlates with the data of studies of short-range order in amorphous MLNS [9].

Spectral dependences of the TKE of three studied MLNS $[(CoFeB)_{60}C_{40}/SiO_2]_{200}$ samples with different thicknesses of bilayers and post-percolation content of metal clusters x = 60 at. % were similar to the spectral dependence of the TKE of the initial amorphous $Co_{40}Fe_{40}B_{20}$ alloy both in form and in sign, at the energy of light quanta higher than 1.3 eV. This fact correlates with the results of structural studies of this MLNS, in which the preservation of interfaces and magnetic clusters of CoFeB was confirmed [6-9]. The relative fraction of the metallic phase in the total volume of this MLNS is lower than in the initial alloy, and therefore the maximum absolute TKE values decreased by about 2.5 times in comparison with the amorphous CoFeB alloy. In this case, the form of the field dependences of TKE of MLNS $[(CoFeB)_{60}C_{40}/SiO_2]_{200}$ had features characteristic of soft ferromagnets.

In another MLNS $[(CoFeB)_{34}(SiO_2)_{66}/C]_{46}$ with a pre-percolation content of metal clusters at x = 34 at. % in a SiO_{2-x} oxide matrix, the spectral dependences of TKE had a fundamentally different form, differing from the spectral dependence of TKE of the initial amorphous $Co_{40}Fe_{40}B_{20}$ both by form and sign.

This is due to the predominant interactions of metal clusters with the SiO_{2-x} dielectric matrix, which significantly reduced their size and coordination numbers, and, ultimately, determine the nature and sign of the spectral dependences of TKE. The TKE field dependences of this MLNS samples were linear, which characteristic of superparamagnets. This is primarily associated with a significantly lower relative content of CoFeB clusters with metal-boron-oxide shells immersed in a dielectric SiO_{2-x} layer of metal-composite layers. As a result, the exchange interaction between the atoms of metal clusters becomes impossible, and a complex heterophase system turns out to be in a superparamagnetic state.

Conflict of interests

The authors declare that they have no known competing financial interests or personal

relationships that could have influenced the work reported in this paper.

References

1. Neugebauer C. A. Resistivity of cermet films containing oxides of silicon. *Thin Solid Films*. 1970;6(6): 443–447. DOI: https://doi.org/10.1016/0040-6090(70)90005-2

2. Gittleman J. L., Goldstain Y., Bozowski S. Magnetic roperties of granular nikel films. *Physical Review B*. 1972;5(9): 3609–3621. DOI: https://doi.org/10.1103/physrevb.5.3609

3. Abeles B., Sheng P., Coutts M. D., Arie Y. Structural and electrical properties of granular metal films. *Advances in Physics*. 1975;24(3): 407–461. DOI: https://doi.org/10.1080/00018737500101431

4. Helman J. S., Abeles B. Tunneling of spin-polarized electrons and magnetoresistance in granular Ni films. *Physical Review Letters*. 1976;37(21): 1429–1433. DOI: https://doi.org/10.1103/physrevlett.37.1429

5. Sheng P., Abeles B., Arie Y. Hopping conductivity in granular Metals. *Physical Review Letters,* 1973;31(1): 44–47. DOI: https://doi.org/10.1103/physrevlett.31.44

6. Domashevskaya E. P., Builov N. S., Terekhov V. A., Barkov K. A., Sitnikov V. G. Electronic structure and phase composition of dielectric interlayers in multilayer amorphous nanostructure $[(CoFeB)_{60}C_{40}/SiO_2]_{200}$. *Physics of the Solid State*. 2017;59(1): 168–173. DOI: https://doi.org/10.1134/S1063783417010061

7. Domashevskaya E. P., Builov N. S., Terekhov V. A., Barkov K. I., Sitnikov V. G., Kalinin Y. E. Electronic structure and phase composition of silicon oxide in the metal-containing composite layers of a $[(Co_{40}Fe_{40}B_{20})_{34}(SiO_2)_{66}/C]_{46}$ multilayer amorphous nanostructure with carbon interlayers. *Inorganic Materials*. 2017;53(9): 930–936. DOI: https://doi.org/10.1134/S0020168517090060

8. Domashevskaya E. P., Builov N. S., Lukin A. N., Sitnikov V. G. Investigation of interatomic interaction in multilayer nanostructures $[(CoFeB)_{60}C_{40}/SiO_2]_{200}$ and $[(Co_{40}Fe_{40}B_{20})_{34}(SiO_2)_{66}/C]_{46}$ with composite metal-containing layers by IR spectroscopy. *Inorganic Materials*. 2018;54(2): 153–159. DOI: https://doi.org/10.7868/s0002337x18020069

9. Domashevskaya E. P., Builov N. S., Ivkov S. A., Guda A. A., Trigub A. L., Chukavin A. I. XPS and XAS investigations of multilayer nanostructures based on the amorphous CoFeB alloy. *Journal of Electron Spectroscopy and Related Phenomena*. 2020;243: 146979–146989. DOI: https://doi.org/10.1016/j.elspec.2020.146979

10. Vonsovskii S. V. Magnetizm [Magnetism]. Moscow: Nauka Publ.; 1971. 1032 p.

11. Gan'shina E., Granovsky A., Gushin V., Kuzmichev M., Podrugin P., Kravetz A., Shipil E. Optical and magneto-optical spectra of magnetic granular alloys. *Physica A: Statistical Mechanics and its Applications*. 1997;241(1-2): 45–51. DOI: https://doi.org/10.1016/s0378-4371(97)00057-5

12. Gan'shina E. A., Kim C. G., Kim C. O., Kochneva M. Yu., Perov N. S., Sheverdyaeva P. M. Magnetostatic and magneto-optical properties of Co-based amorphous ribbons. *Journal of Magnetism and Magnetic Materials*. 2002;239(1-3): 484–486. DOI: https://doi.org/10.1016/s0304-8853(01)00665-5

13. Gan'shina E. A., Vashuk M. V. Evolution of the optical and magnetooptical properties of amorphous metal-insulator nanocomposites. *Journal of Experimental and Theoretical Physics*. 2004;98:1027–1036. DOI: https://doi.org/10.1134/1.1767571

14. Shalygina E. E., Kharlamova A. M., Kurlyandskaya G. V., Svalov A. V. Exchange interaction in Co/Bi/Co thin-film systems with Bi interlayer. *Journal of Magnetism and Magnetic Materials*. 2017;440: 136–139. DOI: https://doi.org/10.1016/j.jmmm.2016.12.144

15. Gan'shina E., Garshin V., Perova N., Zykov G., Aleshnikov A., Kalinin Yu., Sitnikov A. Magneto-optical properties of nanocomposites ferromagnetic-carbon. *Journal of Magnetism and Magnetic Materials*. 2019;470:135–138. DOI: https://doi.org/10.1016/j.jmmm.2017.11.038

16. Buravtsova V. E., Ganshina E. A., Kirov S. A., et. al. Magnetooptical properties of layer-by-layer deposited ferromagnet – dielectric nanocomposites. *Materials Sciences and Applications*. 2013;4(4): 16–23. DOI: http://dx.doi.org/10.4236/msa.2013.44A003

17. Stognei O. V., Kalinin Yu. E., Zolotukhin I. V., Sitnikov A. V., Wagner V., Ahlers F. J. Low temperature behaviour of the giant magnetoresistivity in CoFeB – SiOn granular composites. *Journal of Physics: Condensed Matter*. 2003;15(24): 4267–4772. DOI: https://doi.org/10.1088/0953-8984/15/24/320

18. Stognei O. V., Sitnikov A. V. Anisotropy of amorphous nanogranular composites CoNbTa-SiO n and CoFeB-SiOn. *Physics Solid State*. 2010;52: 2518–2526. DOI: https://doi.org/10.1134/S1063783410120127

19. Dunets O. V., Kalinin Y. E., Kashirin M. A. et al. Electrical and magnetic performance of multilayer structures based on $(Co_{40}Fe4_0B_{20})_{33.9}(SiO_2)_{66.1}$ composite. *Technical Physics*. 2013;58: 1352–1357. DOI: https://doi.org/10.1134/S1063784213090132

20. Gridnev S. A., Kalinin Yu. E., Sitnikov A. V., Stognei O. V. *Nelineinye yavleniya v nano i mikrogeterogennykh sistemakh* [Nonlinear phenomena in nano and microheterogeneous systems]. Moscow: BINOM, Laboratoriya znanii Publ.; 2012. 352 p.

21. Mørup S., Tronc E. Superparamagnetic relaxation of weakly interacting particles. *Physical Review Letters*. 1994;72(20): 3278–3285. DOI: doi.org/10.1103/PhysRevLett.72.3278

22. Coey J. M. D., Khalafalla D. Superparamagnetic γ-Fe_2O_3. *Physica Status Solidi (a)* 1972;11(1): 229–241. DOI: https://doi.org/10.1002/pssa.2210110125

23. Brown W. F. Thermal fluctuations of a single-domain particle. *Physical Review.* 1963;130(5): 1677–1685. DOI: https://doi.org/10.1103/physrev.130.1677

Information about the authors

Elena A. Gan'shina, DSc in Physics and Mathematics, Full Professor, Leading Researcher, Department of Magnetism, Faculty of Physics, Lomonosov Moscow State University, Moscow, Russian Federation; e-mail: eagan@mail.ru. ORCID iD: https://orcid.org/0000-0002-6709-158X.

Vladimir V. Garshin, Postgraduate Student, Department of Magnetism, Faculty of Physics, Lomonosov Moscow State University, Moscow, Russian Federation; e-mail: irving. lambert@mail.ru.

Nikita S. Builov, Postgraduate Student of the Department of Solid State Physics and Nanostructures, Voronezh State University, Voronezh, Russian Federation; e-mail: nik-bujlov@yandex.ru.

Nikolay N. Zubar, Master of Science, Department of Magnetism, Faculty of Physics, Lomonosov Moscow State University, Moscow, Russian Federation; e-mail: zubar.nn16@physics.msu.ru.

Alexandr V. Sitnikov, DSc in Physics and Mathematics, Full Professor, Professor of the Department of Solid State Physics, Voronezh State Technical University, Voronezh, Russian Federation; e-mail: sitnikov04@mail.ru. ORCID iD: https://orcid.org/0000-0002-9438-9234.

Evelina P. Domashevskaya, DSc in Physics and Mathematics, Full Professor, Chief Researcher of the Department of Solid State Physics and Nanostructures, Voronezh State University, Voronezh, Russian Federation; e-mail: ftt@phys.vsu.ru. ORCID iD: https://orcid.org/0000-0002-6354-4799.

All authors have read and approved the final manuscript.

Translated by Valentina Mittova
Edited and proofread by Simon Cox

Condensed Matter and Interphases
(Kondensirovannye sredy i mezhfaznye granitsy)

Original articles

DOI: https://doi.org/10.17308/kcmf.2020.22/3115
Received 20 August 2020
Accepted 07 October 2020
Published online 25 December 2020

ISSN 1606-867X
eISSN 2687-0711

Synthesis, Microstructural and Electromagnetic Characteristics of Cobalt-Zinc Ferrite

© 2020 A. I. Goryachko✉, S. N. Ivanin, V. Yu. Buz'ko

Kuban State University,
14, Stavropolskaya str., Krasnodar 350040, Russian Federation

Abstract

In this study, cobalt-zinc ferrite ($Co_{0.5}Zn_{0.5}Fe_2O_4$) was obtained by the glycine-nitrate method followed by annealing in a high-temperature furnace at a temperature of 1300 °C. The qualitative composition and its microstructural characteristics were determined using energy-dispersive X-ray spectroscopy, X-ray diffraction analysis, and scanning electron microscopy.

The analysis of the micrographs demonstrated that the cobalt-zinc ferrite micropowder obtained after thermal annealing has an average particle size of 1.7±1 μm. The analysis of XRD data showed that the annealed cobalt-zinc ferrite micropowder has a cubic crystal structure with a lattice parameter of a = 8.415 Å. Using the Scherrer and Williamson-Hall equations we calculated the average sizes of the coherent scattering regions, which were commensurate with the size of crystallites: according to the Scherrer equation D = 28.26 nm and according to the Williamson-Hall equation D = 33.59 nm and the microstress value $\varepsilon = 5.62\times10^{-4}$ in the ferrite structure.

Using a vector network analyser, the electromagnetic properties of a composite material based on synthesized cobalt-zinc ferrite were determined. The frequency dependences of the magnetic and dielectric permeability values from the measured S-parameters of the composite material (50% ferrite filler by weight and 50% paraffin) were determined using the Nicolson-Ross-Weir method and were in the range of 0.015–7 GHz. The analysis of the graphs of the dependence of the magnetic permeability on the frequency of electromagnetic radiation revealed a resonance frequency of $f_r \approx 2.3$ GHz. The discovered magnetic resonance in the UHF range allows the obtained material to be considered as being promising for use as an effective absorber of electromagnetic radiation in the range of 2–2.5 GHz.

Keywords: glycine-nitrate synthesis, cobalt-zinc ferrite, ferrimagnetic, microstructure, composite materials, magnetic permeability, dielectric permittivity.

For citation: Goryachko A.I., Ivanin S.N., Buz'ko V. Yu. Synthesis, microstructural and electromagnetic characteristics of cobalt-zinc ferrite. *Kondensirovannye sredy i mezhfaznye granitsy = Condensed Matter and Interphases*. 2020; 22(4): 446–452. DOI: https://doi.org/10.17308/kcmf.2020.22/3115

Для цитирования: Горячко А. И., Иванин С. Н., Бузько В. Ю. Синтез, микроструктурные и электромагнитные характеристики кобальт-цинкового феррита. *Конденсированные среды и межфазные границы*. 2020; 22(4): 446–452. DOI: https://doi.org/10.17308/kcmf.2020.22/3115

✉ Goryachko Alexander Ivanovich, e-mail: Alexandr_g_i@mail.ru

1. Introduction

The development of methods for obtaining powder metal-oxide magnetic materials is currently considered an urgent task. Such materials are ferrites, which are solid solutions based on iron (III) oxide [1–3]. It is known, that zinc-based ferrite spinels are often used in the industry. The main ones are manganese-zinc and nickel-zinc ferrites with a cubic crystal lattice. However, the disadvantage of these ferrites is their rather low resonance frequency. The substitution of cobalt or nickel by manganese allows the magnetic properties to be changed significantly, namely, to shift the resonance to higher frequencies and, consequently, to increase Snoek's limit [4].

Now, there are various methods for obtaining both nano-sized and micro-sized ferrite powders using ceramic technologies and from salt solutions [5–7]. The production method significantly affects the shape and size of the particles, which determines the microstructural and electromagnetic properties of the material [8–10]. For example, one of the most widespread methods of obtaining ferrite powder is ceramic synthesis [11–14]. However, the disadvantage of this method is the long-term high-temperature annealing, which leads to an inhomogeneity of particles, the manifestation of anisotropy, and the poor reproducibility of electromagnetic properties; therefore, chemical syntheses are promising methods for obtaining ferrite materials. When ferrite is obtained by chemical synthesis, energy consumption can be reduced and the uniformity of particles can be significantly improved [15]. The main chemical methods for producing ferrites from metal nitrates include: nitrate-urea [16, 17], nitrate-citrate [18, 19], as well as the glycine-nitrate method used in this study [20–22], etc. The advantage of the glycine-nitrate method is that the required temperature of the mixture at which the pyrochemical reaction occurs is about 150 °C, which is significant lower than that of nitrate-urea and nitrate-citrate syntheses.

The purpose of this study was the synthesis of cobalt-zinc ferrite by the glycine-nitrate method, high-temperature annealing at a temperature of 1300 °C, and research into its microstructural and electromagnetic characteristics.

2. Experimental

The following reagents were used for the synthesis of $Co_{0.5}Zn_{0.5}Fe_2O_4$ ferrite: $Co(NO_3)_2 \cdot 6H_2O$ (chemically pure, RF), $Zn(NO_3)_2 \cdot 6H_2O$ (chemically pure, RF), $Fe(NO_3)_3 \cdot 9H_2O$ (analytical grade, RF), glycine acid ($C_2H_5NO_2$, chemically pure, RF). The metal nitrates and glycine that were used were taken in the required stoichiometric quantities and then dissolved in bi-distilled water. Then the resulting mixture was gradually heated for 1 h to a temperature of 150 °C with constant stirring. After a certain amount of time, after the evaporation of the excess volume of bi-distilled water, the solution was a viscous gel-like product. With further heating, the resulting viscous gel ignited spontaneously, followed by combustion for 5–6 seconds. In the course of thermolysis, a highly porous, weakly magnetic, light brown foamy substance was formed. The equation for the pyrochemical reaction that took place can be represented as follows:

$$0.5Co(NO_3)_2 \cdot 6H_2O + 0.5Zn(NO_3)_2 \cdot 6H_2O + 2Fe(NO_3)_3 \cdot 9H_2O + 3C_2H_5NO_2 \rightarrow Co_{0.5}Zn_{0.5}Fe_2O_4 + 5.5N_2\uparrow + 6CO_2\uparrow + 37.5H_2O\uparrow + 0.25O_2\uparrow$$

After the completion of the reaction and subsequent cooling, the ferrite sample was ground in a ceramic mortar for 30 minutes. Then, for the removal of the residual impurities, the resulting synthesized powder was heat treated in a "Nabertherm Top 16/R + B400" high-temperature furnace at a temperature of 1300 °C for 1 hour. Additionally, after cooling, the calcined ferrite powder was ground in a ceramic mortar for 10 minutes in order to obtain a homogeneous micropowder.

Photos of the microstructure of the investigated $Co_{0.5}Zn_{0.5}Fe_2O_4$ ferrite were obtained using a "JEOL JSM-7500F" scanning electron microscope and energy dispersive analysis was performed using the "INCA X-Sight" attachment.

X-ray diffraction analysis of the cobalt-zinc ferrite sample was carried out using a "Shimadzu XRD-7000" powder diffractometer. The sample was investigated at room temperature in the angle range of 2θ from 3° up to 70° with a scanning step of 0.02°.

For the study of the electromagnetic properties of cobalt-zinc ferrite, a composite material based on paraffin with a ferrite filler concentration of 50% by weight was made.

The sample was made in the form of a toroid with a thickness of 4 mm, an outer diameter of 7 mm, and an inner diameter of 3.05 mm. Electromagnetic characteristics (magnetic and dielectric constants) were calculated based on experimentally measured S-parameters using a "Deepace KC901V" vector network analyser in the range of 0.015-7 GHz.

3. Results and discussion

The spectrum of energy dispersive X-ray spectroscopy (EDS) with the selected analysis area for the studied $Co_{0.5}Zn_{0.5}Fe_2O_4$ ferrite micropowder, annealed for 1 hour at a temperature of 1300 °C is shown in Fig. 1. The obtained results of the EDA analysis show the presence of the main elements: Co (12.68%), Zn (12.24%), Fe (45.21%) and O (29.86%) in the composition of the studied micropowder.

The photograph of an annealed $Co_{0.5}Zn_{0.5}Fe_2O_4$. micropowder is presented in Fig. 2a. Based on the analysis of the obtained photograph, it can be noted that after thermal annealing at a temperature of 1300 °C the studies sample consisted of spherical microparticles. The detailed examination of the microstructure of the powder revealed both individual and fused ferrite particles. Based on the analysis of the micrographs of the studied $Co_{0.5}Zn_{0.5}Fe_2O_4$, the histogram of the particle size distribution depending on their number was calculated (Fig. 4b). The histogram of the particle size distribution was obtained based on the analysis of 2700 particles using the "ImageJ" program. For each individual particle, the equivalent diameter was determined based on the results of measurements of its length and width according to the procedure from the study [23]. Based on the data obtained from the histogram of annealed $Co_{0.5}Zn_{0.5}Fe_2O$ ferrite a relatively narrow particle size distribution was revealed. The calculated average particle size of the synthesized cobalt-zinc ferrite is 1.7 ± 1 μm, which indicates a high degree of particle homogeneity in the studied sample.

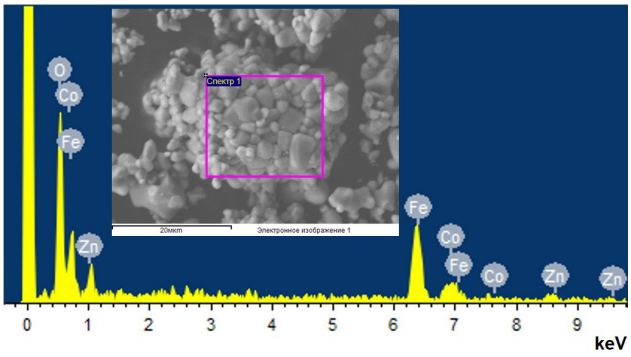

Fig. 1. EDX spectrum of the studied $Co_{0.5}Zn_{0.5}Fe_2O_4$ ferrite annealed at a temperature of 1300 °C

The XRD pattern for the investigated $Co_{0.5}Zn_{0.5}Fe_2O_4$ ferrite micropowder is presented in Fig. 3, and the processed data of XRD pattern are presented in Table 1.

Analysis of the obtained data demonstrates that the characteristic peaks on the XRD pattern correspond to the pure cubic spinel phase [24]. Using equation (1), it was determined that the annealed ferrite micropowder has a cubic structure with a crystal lattice parameter of a = 8.415 Å. The calculated parameter of the

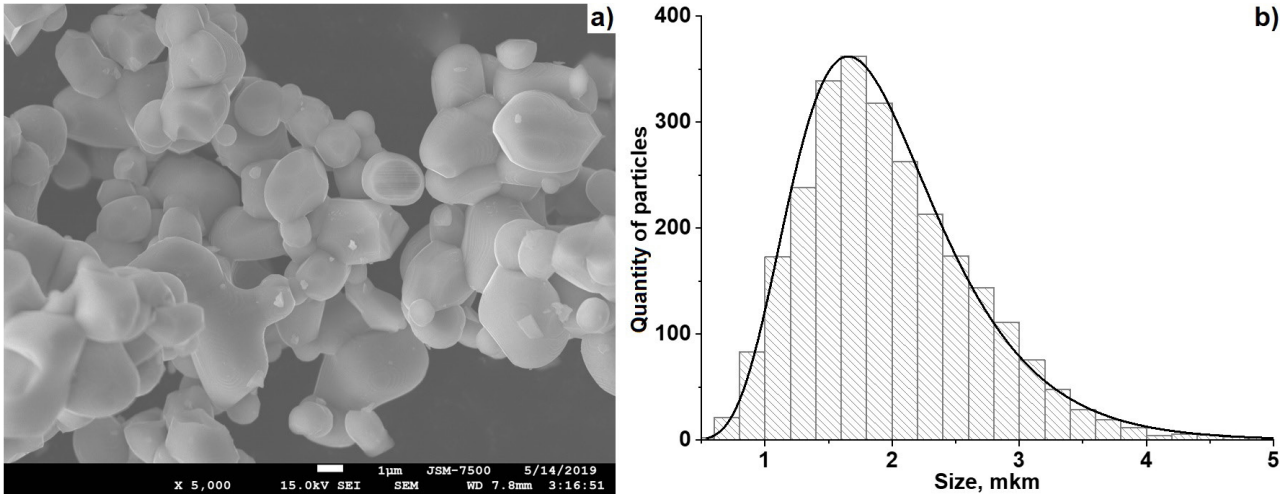

Fig. 2. SEM micrograph of the studied powder at a magnification of ×5000 (a) and a histogram of the particle size (b), for $Co_{0.5}Zn_{0.5}Fe_2O_4$ after annealing for 1 hour at a temperature of 1300 °C

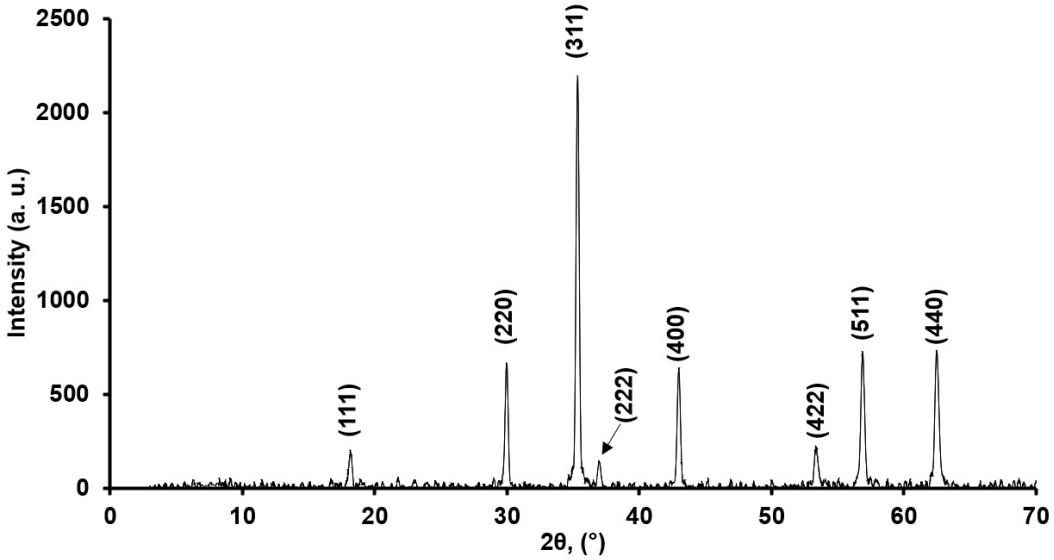

Fig. 3. XRD pattern of the investigated $Co_{0.5}Zn_{0.5}Fe_2O_4$ micropowder after annealing for 1 hour at a temperature of 1300 °C

Table 1. XRD data for the investigated $Co_{0.5}Zn_{0.5}Fe_2O_4$ ferrite

no. of peak	angle, 2θ	Intensity, [%]	d-spacing, [Å]	FWHM, rad
1	18.18	9.6	4.876	0.00489
2	29.98	29.6	2.978	0.00471
3	35.36	100	2.536	0.00488
4	36.96	7.6	2.430	0.00488
5	43.00	20.3	2.102	0.00506
6	53.34	8.1	1.716	0.00617
7	56.90	26	1.617	0.00610
8	62.48	34.3	1.485	0.00612

crystal lattice for the investigated ferrite agrees well to the data of the study [25] demonstrating that a = 8.418 Å, for $Co_{0.5}Zn_{0.5}Fe_2O_4$ ferrite after 6-hour annealing at 1000 °C [25].

$$\frac{1}{d_{hkl}^2} = \frac{(h^2 + l^2 + k^2)}{a^2}. \quad (1)$$

Average size of coherent scattering regions (CSR) – D, comparable with the crystallite size, was calculated for the sample based on the data of X-ray diffraction analysis (XRD) using the Scherrer equation (2) [19]:

$$D = \frac{k\lambda}{\beta\cos\theta}. \quad (2)$$

Where k = 0.9 for spherical particles; λ = 0.154 – wavelength of CuK_α radiation, nm; β – half-width at half-heights of integral peaks, rad, θ –Bragg angle, rad.

The CSR value calculated according to Scherrer for the investigated ferrite is: D = 28.26 nm.

Additionally for the investigated ferrite, the CSR values and microstresses were calculated using Williamson-Hall method (Fig. 3) according to equation (3):

$$\text{FWHM}\cdot\cos\theta = \frac{\lambda}{D} + 4\varepsilon\cdot\sin\theta, \quad (3)$$

where FWHM is the half-width at half-height of the integral peaks, rad; θ — Bragg angle, rad; λ = 0.154 – wavelength of CuK_a radiation, nm; D – the required size of the CSR, nm; ε – microstress value.

Calculation of CSR sizes and microstresses for $Co_{0.5}Zn_{0.5}Fe_2O_4$ micropowder by Williamson–Hall method provided the following results: CSR size – 33.59 nm, which insignificantly differs from the data obtained by the Scherrer method; microstress value $\varepsilon = 5.62\times10^{-4}$.

The values of the magnetic ($\mu = \mu' + i\mu''$) and dielectric ($\varepsilon = \varepsilon' + i\varepsilon''$) permittivity in complex form for a composite material based on the

investigated $Co_{0.5}Zn_{0.5}Fe_2O_4$ were calculated from the experimentally measured values of S_{11} and S_{21} according to the Nicholson–Ross–Weir algorithm [26–29]. The tangents of the angles of magnetic and dielectric losses were calculated using the following formulas (4):

$$\mathrm{tg}\,\delta_\mu = \frac{\mu''}{\mu'},\ \mathrm{tg}\,\delta_\varepsilon = \frac{\varepsilon''}{\varepsilon'} \quad (4)$$

Fig. 4a shows the graphs of the dependence of μ′ and μ″ for the investigated composite material ($Co_{0.5}Zn_{0.5}Fe_2O_4$/paraffin = 1/1 by weight) in the frequency range of 0.015–7 GHz. A slight decrease in μ′ from 1.85 to 1.69 was observed in the low frequency range (0.015–0.5 GHz). However, with an increase in the frequency of electromagnetic radiation (> 0.5 GHz), the significant sharp decrease in μ′ value up to 1.041 at frequency of 7 GHz can be seen on the graph. The analysis of μ″ data revealed that the maximum value of the magnetic loss was observed at the frequency of f_r ≈ 2.3 GHz, which is in good agreement with the data of [30], where the maximum value of magnetic losses is observed in the range of 2.2–2.4 GHz [30]. Maximal detected μ″, which was 0.323, corresponded to the resonance frequency for the produced composite material. Based on the obtained μ′ and μ″ data, tangent of the angle of magnetic losses at the resonant frequency was calculated and it was tg δ_μ ≈ 0.252.

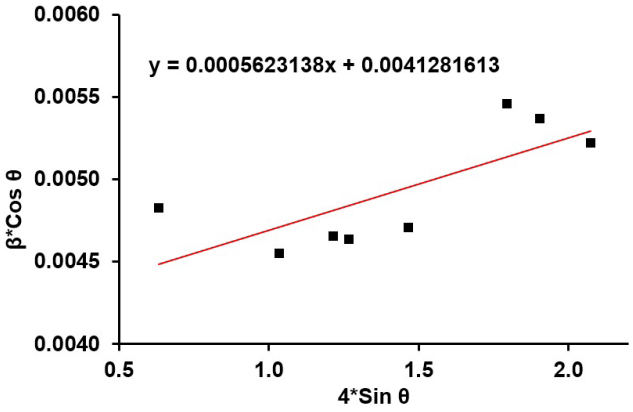

Fig. 4. Williamson-Hall plot for the investigated $Co_{0.5}Zn_{0.5}Fe_2O_4$

Dependency graphs of ε′ and ε″ for the manufactured composite material based on $Co_{0.5}Zn_{0.5}Fe_2O_4$ are shown in Fig. 4b. According to the experimental data, it can be seen that the value for both ε′ and ε″ for the investigated composite sample practically does not change in the entire investigated frequency range, on the basis of which it can be concluded that the average value of the dielectric constant for cobalt-zinc ferrite in the investigated frequency range is ε′ ≈ 3.12 and ε″ ≈ 0.014. From the calculated date for ε′ and ε″ it follows that the tangent of the angle of dielectric losses in the entire measured range was tg δ_ε ≈ 0.0045.

Since the values obtained for ε′, ε″ and tg δ_ε were low and practically did not change in the entire investigated frequency range, it can be concluded that the dielectric parameters insignificantly affect the radio-absorbing (except for the resonance frequency shift) or radio-shielding characteristics of the investigated composite material.

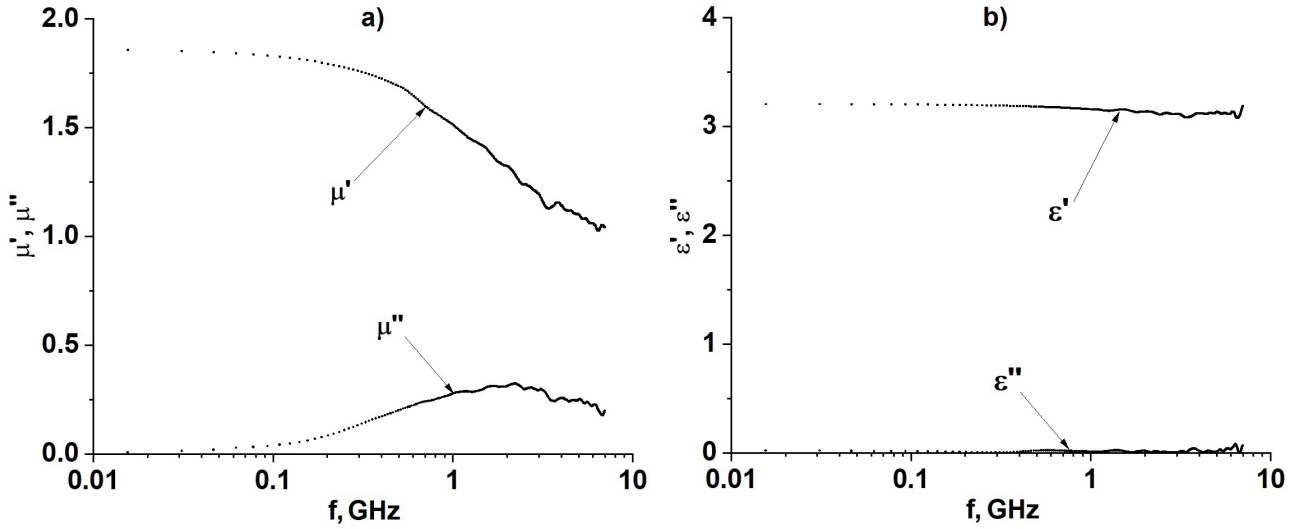

Fig. 5. Frequency dependence of complex magnetic permeability (a) and complex dielectric permittivity (b) for the fabricated composite material based on $Co_{0.5}Zn_{0.5}Fe_2O_4$

4. Conclusions

The granular ferrite $Co_{0.5}Zn_{0.5}Fe_2O_4$ with micron-sized granules consisting (according to XRD data) of nanocrystals with average sizes of ~25–35 nm was obtained by glycine-nitrate synthesis after one-hour thermal annealing at 1300 °C and subsequent grinding. The synthesized ferrite after thermal annealing did not contain impurities of other elements or side phases as was confirmed by EDS and XRD methods. Analysis of XRD data showed that investigated $Co_{0.5}Zn_{0.5}Fe_2O_4$ ferrite has a cubic crystal lattice. The resulting ferrite powder after high-temperature annealing of $Co_{0.5}Zn_{0.5}Fe_2O_4$ at 1300 °C within 1 hour has a fairly high uniformity in shape and particle size as was established based on the obtained micrographs and histograms of the particle size distribution. The analysis of the graphs of the dependence of magnetic permeability on the frequency of electromagnetic radiation revealed the magnetic resonance at frequency 2.3 GHz. The discovered magnetic resonance in the UHF range allows the obtained material to be considered as being promising for use as an effective absorber of electromagnetic radiation in the range of 2–2.5 GHz.

Acknowledgements

The work was carried out based on the REC Centre for Collective Use "Diagnostics of the structure and properties of nanomaterials" of the Kuban State University.

Conflict of interests

The authors declare that they have no known competing financial interests or personal relationships that could have influenced the work reported in this paper.

References

1. Thakur P., Chahar D., Taneja S., Bhalla N. and Thakur A. A review on MnZn ferrites: Synthesis, characterization and applications. *Ceramics International*. 2020;46(10): 15740–15763. DOI: https://doi.org/10.1016/j.ceramint.2020.03.287

2. Pullar R. C. Hexagonal ferrites: A review of the synthesis, properties and applications of hexaferrite ceramics. *Progress in Materials Science*. 2012;57(7): 1191–1334. DOI: https://doi.org/10.1016/j.pmatsci.2012.04.001

3. Kharisov B. I., Dias H. V. R., Kharissova O. V. Mini-review: Ferrite nanoparticles in the catalysis. *Arabian Journal of Chemistry*. 2019;12(7): 1234–1246. DOI: https://doi.org/10.1016/j.arabjc.2014.10.049

4. Stergiou C. Microstructure and electromagnetic properties of Ni-Zn-Co ferrite up to 20 GHz. *Advances in Materials Science and Engineering*. 2016;2016: 1–7. DOI: https://doi.org/10.1155/2016/1934783

5. Economos G. Magnetic ceramics: I, General methods of magnetic ferrite preparation. *Journal of the American Ceramic Society*. 1955;38(7): 241–244. DOI: https://doi.org/10.1111/j.1151-2916.1955.tb14938.x

6. Yurkov G. Y., Shashkeev K. A., Kondrashov S. V., Popkov O. V., Shcherbakova G. I., Zhigalov D. V., Pankratov D. A., Ovchenkov E. A., Koksharov Y. A. Synthesis and magnetic properties of cobalt ferrite nanoparticles in polycarbosilane ceramic matrix. *Journal of Alloys and Compounds*. 2016;686: 421–430. DOI: https://doi.org/10.1016/j.jallcom.2016.06.025

7. Karakaş Z. K., Boncukçuoğlu R., Karakaş İ. H. The effects of fuel type in synthesis of $NiFe_2O_4$ nanoparticles by microwave assisted combustion method. *Journal of Physics: Conference Series*. 2016; 707: 012046. DOI: https://doi.org/10.1088/1742-6596/707/1/012046

8. Shirsath S. E., Jadhav S. S., Mane M. L., Li S. *Handbook of sol-gel science and technology*. Springer, Cham.; 2016. p. 1–41. DOI: https://doi.org/10.1007/978-3-319-19454-7_125-1

9. Vyzulin S. A., Kalikintseva D. A., Miroshnichenko E. L., Buz'ko V. Y., Goryachko A. I. Microwave absorption properties of nickel–zinc ferrites synthesized by different means. *Bulletin of the Russian Academy of Sciences: Physics*. 2018;82(8): 943–945. DOI: https://doi.org/10.3103/s1062873818080439

10. Janasi S. R., Emura M., Landgraf F. J. G., Rodrigues D. The effects of synthesis variables on the magnetic properties of coprecipitated barium ferrite powders. *Journal of Magnetism and Magnetic Materials*. 2002;238(2-3): 168–172. DOI: https://doi.org/10.1016/s0304-8853(01)00857-5

11. Ahmed Y. M. Z. Synthesis of manganese ferrite from non-standard raw materials using ceramic technique. *Ceramics International*. 2010;36(3): 969–977. DOI: https://doi.org/10.1016/j.ceramint.2009.11.020

12. Mahadule R. K., Arjunwadkar P. R., Mahabole M. P. Synthesis and characterization of $Ca_xSr_yBa_{1-x-y}Fe_{12-z}La_zO_{19}$ by standard ceramic method. *International Journal of Metals*. 2013;2013: 1–7. DOI: https://doi.org/10.1155/2013/198970

13. Tarţa V. F., Chicinaş I., Marinca T. F., Neamţu B. V., Popa F., Prica C. V. Synthesis of the nanocrystalline/nnosized $NiFe_2O_4$ powder by ceramic method and mechanical milling. *Solid State Phenomena*. 2012;188: 27–30. DOI: https://doi.org/10.4028/www.scientific.net/ssp.188.27

14. Pradhan A. K., Saha S., Nath T. K. AC and DC electrical conductivity, dielectric and magnetic properties of $Co_{0.65}Zn_{0.35}Fe_{2-x}Mo_xO_4$ (x = 0.0, 0.1 and 0.2) ferrites. *Applied Physics A*. 2017;123(11): 715. DOI: https://doi.org/10.1007/s00339-017-1329-z

15. Low Z. H., Ismail I., Tan K. S. Sintering processing of complex magnetic ceramic oxides: A comparison between sintering of bottom-up approach synthesis and mechanochemical process of top-down approach synthesis. *Sintering Technology - Method and Application*. Malin Liu (ed.). 2018: 25–43. DOI: https://doi.org/10.5772/intechopen.78654

16. Costa A. C. F. M., Morelli M. R., Kiminami R. H. G. A. Combustion synthesis: Effect of urea on the reaction and characteristics of Ni–Zn ferrite powders. *Journal of Materials Synthesis and Processing*. 2001;9(6): 347–352. DOI: https://doi.org/10.1023/A:1016356623401

17. Maleknejad Z., Gheisari K., Raouf A. H. Structure, microstructure, magnetic, electromagnetic, and dielectric properties of nanostructured Mn–Zn ferrite synthesized by microwave-induced urea–nitrate process. *Journal of Superconductivity and Novel Magnetism*. 2016;29(10): 2523–2534. DOI: https://doi.org/10.1007/s10948-016-3572-5

18. Jalaiah K., Chandra Mouli K., Vijaya Babu K., Krishnaiah R.V. The structural, DC resistivity and magnetic properties of Mg and Zr Co-substituted $Ni_{0.5}Zn_{0.5}Fe_2O_4$. *Journal of Science: Advanced Materials and Devices*. 2018;4(2): 310–318. DOI: https://doi.org/10.1016/j.jsamd.2018.12.004

19. Yue Z., Zhou J., Li L., Zhang H., Gui Z. Synthesis of nanocrystalline NiCuZn ferrite powders by sol–gel auto-combustion method. *Journal of Magnetism and Magnetic Materials*. 2000;208(1-2): 55–60. DOI: https://doi.org/10.1016/s0304-8853(99)00566-1

20. Chick L. A., Pederson L. R., Maupin G. D., Bates J. L., Thomas L. E., Exarhos G. J. Glycine-nitrate combustion synthesis of oxide ceramic powders. *Materials Letters*. 1990;10(1-2): 6–12. DOI: https://doi.org/10.1016/0167-577x(90)90003-5

21. Salunkhe A. B., Khot V. M., Phadatare M. R., Pawar S. H. Combustion synthesis of cobalt ferrite nanoparticles—Influence of fuel to oxidizer ratio. *Journal of Alloys and Compounds*. 2012;514: 91–96. DOI: https://doi.org/10.1016/j.jallcom.2011.10.094

22. Martinson K. D., Cherepkova I. A., Sokolov V. V. Formation of cobalt ferrite nanoparticles via glycine-nitrate combustion and their magnetic properties. *Glass Physics and Chemistry*. 2018;44(1): 21–25. DOI: https://doi.org/10.1134/s1087659618010091

23. Kuzmin V. A., Zagrai I. A. A comprehensive study of combustion products generated from pulverized peat combustion in the furnace of BKZ-210-140F steam boiler. *Journal of Physics: Conference Series*. 2017;891: 012226. DOI: https://doi.org/10.1088/1742-6596/891/1/012226

24. Maleki A., Hosseini N., Taherizadeh A. Synthesis and characterization of cobalt ferrite nanoparticles prepared by the glycine-nitrate process. *Ceramics International*. 2018;44(7): 8576–8581. DOI: https://doi.org/10.1016/j.ceramint.2018.02.063

25. Waje S. B., Hashim M., Wan Yusoff W. D., Abbas Z. Sintering temperature dependence of room temperature magnetic and dielectric properties of $Co_{0.5}Zn_{0.5}Fe_2O_4$ prepared using mechanically alloyed nanoparticles. *Journal of Magnetism and Magnetic Materials*. 2010;322(6): 686–691. DOI: https://doi.org/10.1016/j.jmmm.2009.10.041

26. Nicolson A. M., Ross G. F. Measurement of the intrinsic properties of materials by time-domain techniques. *IEEE Transactions on Instrumentation and Measurement*. 1970;19(4): 377–382. DOI: https://doi.org/10.1109/tim.1970.4313932

27. Rothwell E. J., Frasch J. L., Ellison S. M., Chahal P., Ouedraogo R.O. Analysis of the Nicolson-Ross-Weir method for characterizing the electromagnetic properties of engineered materials. *Progress In Electromagnetics Research*. 2016;157: 31–47. DOI: https://doi.org/10.2528/pier16071706

28. Vicente A. N., Dip G. M., Junqueira C. The step by step development of NRW method. Proceedings Article in: *2011 SBMO/IEEE MTT-S International Microwave and Optoelectronics Conference (IMOC 2011). 29 Oct. – 1 Nov.* 2011. 738–742. DOI: https://doi.org/10.1109/imoc.2011.6169318

29. Ivanin S. N., Buz'ko V. Yu., Goryachko A. I., Panyushkin V. T. Electromagnetic characteristics of heteroligand complexes of gadolinium stearate. *Russian Journal of Physical Chemistry*. 2020;94(8): 1623–1627. DOI: https://doi.org/10.1134/S0036024420080130

30. Liu Y. W., Zhang J., Gu L. S., Wang L. X., Zhang Q. T. Preparation and electromagnetic properties of nanosized $Co_{0.5}Zn_{0.5}Fe_2O_4$ ferrite. *Rare Metals*. 2016. DOI: https://doi.org/10.1007/s12598-015-0670-7

Information about the authors

Goryachko Alexander Ivanovich, PhD student, Department of Theoretical Physics and Computer Technologies, Faculty of Physics and Technology, Kuban State University, Krasnodar, Russian Federation; e-mail: Alexandr_g_i@mail.ru. ORCID iD: https://orcid.org/0000-0001-6480-353X.

Ivanin Sergey Nikolaevich, PhD student, Kuban State University, Krasnodar, Russian Federation; e-mail: Ivanin18071993@mail.ru. ORCID iD: https://orcid.org/0000-0001-9352-5970.

Buzko Vladimir Yurievich, PhD in Chemistry, Associate Professor, Department of Radiophysics and Nanotechnology, Faculty of Physics and Technology, Kuban State University, Krasnodar, Russian Federation; e-mail: Buzkonmr@maul.ru. ORCID iD: https://orcid.org/0000-0002-6335-0230.

All authors read and approved the final manuscript.

Translated by Valentina Mittova
Edited and proofread by Simon Cox

Condensed Matter and Interphases
(Kondensirovannye sredy i mezhfaznye granitsy)

Original articles

DOI: https://doi.org/10.17308/kcmf.2020.22/3116
Received 09 October 2020
Accepted 15 November 2020
Published online 25 December 2020

ISSN 1606-867X
eISSN 2687-0711

Thermodynamic Properties of Terbium Tellurides

© 2020 S. Z. Imamaliyeva[a]✉, D. M. Babanly[a,b], V. P. Zlomanov[c], D. B. Taghiyev[a], M. B. Babanly[a,d]

[a]*Institute of Catalysis and Inorganic Chemistry, Azerbaijan National Academy of Sciences, 113 H. Javid ave., Baku AZ-1143, Azerbaijan*

[b]*Azerbaijan State Oil and Industry University, 6/21 Azadlıq ave., Baku AZ-1143, Azerbaijan*

[c]*Lomonosov Moscow State University, GSP-1, Leninskie Gory, Moscow 119991, Russian Federation*

[d]*Baku State University, 23, Academic Zahid Khalilov str., Baku AZ-1073/1, Azerbaijan*

Abstract

The paper presents the results of a study of solid-phase equilibria in the Tb–Te system and the thermodynamic properties of terbium tellurides obtained by the methods of electromotive forces and X-ray diffraction analysis. Based on the experimental data, it was established that the TbTe, Tb_2Te_3, $TbTe_2$ и $TbTe_3$ compounds are formed in the system. For the investigations of the alloys from the two-phase regions $TbTe_3$+Te, $TbTe_2$+$TbTe_3$, and Tb_2Te_3+$TbTe_2$, the EMF of concentration cells relative to the TbTe electrode was measured. The EMF of concentration cells relative to the terbium electrode was measured for the TbTe+Tb_2T_3 region. The partial thermodynamic functions of TbTe and Tb in alloys were determined by combining the EMF measurements of both types in the 300–450 K temperature range, based on which the standard thermodynamic functions of formation and standard entropies of the indicated terbium tellurides were calculated.

Keywords: terbium tellurides, electromotive forces method, thermodynamic functions

Funding: The work has been carried out within the framework of the international joint research laboratory "Advanced Materials for Spintronics and Quantum Computing" (AMSQC) established between the Institute of Catalysis and Inorganic Chemistry of ANAS (Azerbaijan) and Donostia International Physics Center (Basque Country, Spain) and partially supported by the Science Development Foundation under the President of the Republic of Azerbaijan, grant EİF/MQM/Elm-Tehsil-1-2016-1(26)-71/01/4-M-33.

For citation: Imamaliyeva S. Z., Babanly D. M., Zlomanov V. P., Taghiyev D. B., Babanly M. B. Thermodynamic properties of terbium tellurides. *Kondensirovannye sredy i mezhfaznye granitsy = Condensed Matter and Interphases.* 2020;22(4): 453–459. DOI: https://doi.org/10.17308/kcmf.2020.22/3116

Для цитирования: Имамалиева С. З., Бабанлы Д. М., Зломанов В. П., Тагиев Д. Б., Бабанлы М. Б. Термодинамические свойства теллуридов тербия. *Конденсированные среды и межфазные границы*. 2020; 22(4): 453–459. DOI: https://doi.org/10.17308/kcmf.2020.22/3116

✉ Samira Zakir Imamaliyeva, e-mail: samira9597a@gmail.com

1. Introduction

Rare earth element (REE) compounds are among the promising functional materials widely used in aerospace system applications, high-power radiofrequency sources, computer hard drives, battery electrodes for high-power batteries, etc. [1, 2]. Among them, REE chalcogenides, possessing high thermal stability, resistance to changes in environmental conditions, unique magnetic, optical, and thermoelectric properties, which are used in modern electronic technology [3–10].

The development and optimization of methods for the directed synthesis of new phases are based on data about phase equilibria in the corresponding systems and the thermodynamic properties of intermediate phases [11–13].

Although the phase diagrams of most Ln-Te type binary systems have been studied in detail and presented in a number of monographs and handbooks [3, 10, 14] phase diagram of the Tb-Te system has not yet been constructed. According to [3], terbium with tellurium forms following compounds: TbTe, Tb_2Te_3, $TbTe_{1.8}$, Tb_2Te_5, and $TbTe_3$. In later studies [15, 16], the tellurides TbTe, Tb_2Te_3, $TbTe_2$, and $TbTe_3$ were confirmed. However, we have not found any information on the crystal structure and properties of Tb_2Te_5.

In the literature, the experimental data on the thermodynamic properties of terbium tellurides are very limited. The handbook [17] contains the estimated data on the standard enthalpy of formation and entropy of TbTe and Tb_2Te_3. In the recently published studies [18, 19], the thermodynamic functions of formation and the entropy of the Tb_2Te_3 compound were estimated by the "tetrad effect" method.

This study presents the results of an investigation of solid-phase equilibria in the Tb-Te system and the thermodynamic properties of terbium tellurides.

2. Experimental

For research, alloys of the Tb-Te system with compositions > 50 at% Te (each weighing 0.5 g) were synthesized. The elements and reagents purchased from Alfa Aesar were used. The synthesis was carried out by direct interaction of elemental terbium (CAS No. 7440-27-9) and tellurium (CAS No. 13494-80-9) in evacuated (10^{-2} Pa) quartz ampoules. In order to prevent the interaction of terbium with the inner walls of quartz ampoules, the synthesis of alloys was performed in graphitized ampoules. The ampoules were graphitized by the thermal decomposition of toluene.

After keeping the ampoules at 1000 K for 24 h, the alloys were ground into a powder, mixed, pressed into tablets, and annealed at 800 K (alloys with compositions 50–75 at% Te) or 700 K (alloys with compositions > 75 at% Te) for 1000 hours. Then the alloys were cooled in the switched-off furnace and were investigated by XRD (Bruker D8 diffractometer, $CuK\alpha_1$ radiation). The XRD results confirmed the existence of the TbTe, Tb_2Te_3, $TbTe_2$, and $TbTe_3$ compounds.

For the investigation of the thermodynamic properties of phases of the Tb-Te system by EMF method, the following concentration cells of types (1) and (2) were assembled and their EMF were measured in the temperature range of 300–450 K.

$$(-)\,Tb\,(s.)\,|\,glycerol + KCl + TbCl_3\,|\,(TbTe1_{+x})\,(s.)\,(+)\quad (1)$$

$$(-)TbTe(s.)|glycerol+KCl+TbCl_3|(TbTe1_{+x})(s.)(+)\quad (2)$$

Terbium was used as the left electrode in a type (1) cell, and terbium monotelluride with a slight excess of tellurium (composition $TbTe_{1.01}$) was used in a type (2) cell. Synthesized equilibrium alloys with different compositions from the two-phase regions TbTe+Tb_2Te_3 (50.3 and 55 at% Te), Tb_2Te_3+$TbTe_2$ (61 and 65 at% Te), $TbTe_2$+$TbTe_3$ (68 and 72 at% Te) and $TbTe_3$+Te (77 and 90 at% Te) were used as the right electrodes. A sample with the composition 50.3 at% Te ($TbTe_{1.01}$) was used in a type (1) cell as the right electrode and reproducible results were obtained.

The phase compositions of all the indicated alloys were confirmed by XRD analysis. As an example, powder X-ray diffraction patterns of an alloy with a composition of 55 at% Te are shown in Fig. 1. As can be seen, this sample is two-phase and consists of a mixture of TbTe+Tb_2Te_3 compounds.

The terbium electrode was prepared by fixing a piece of metallic terbium on a molybdenum wire (down conductor), and all other samples were prepared by pressing the corresponding powder alloys on down conductors in the form of cylindrical tablets (diameter ~7 mm and thickness 2–3 mm)

In both electrochemical cells, a glycerol (CAS No. 56-81-5) solution of KCl (CAS No. 7447-40-7) with a small addition (0.1%) amount of $TbCl_3$ (CAS No. 10042-88-3) served as the electrolyte.

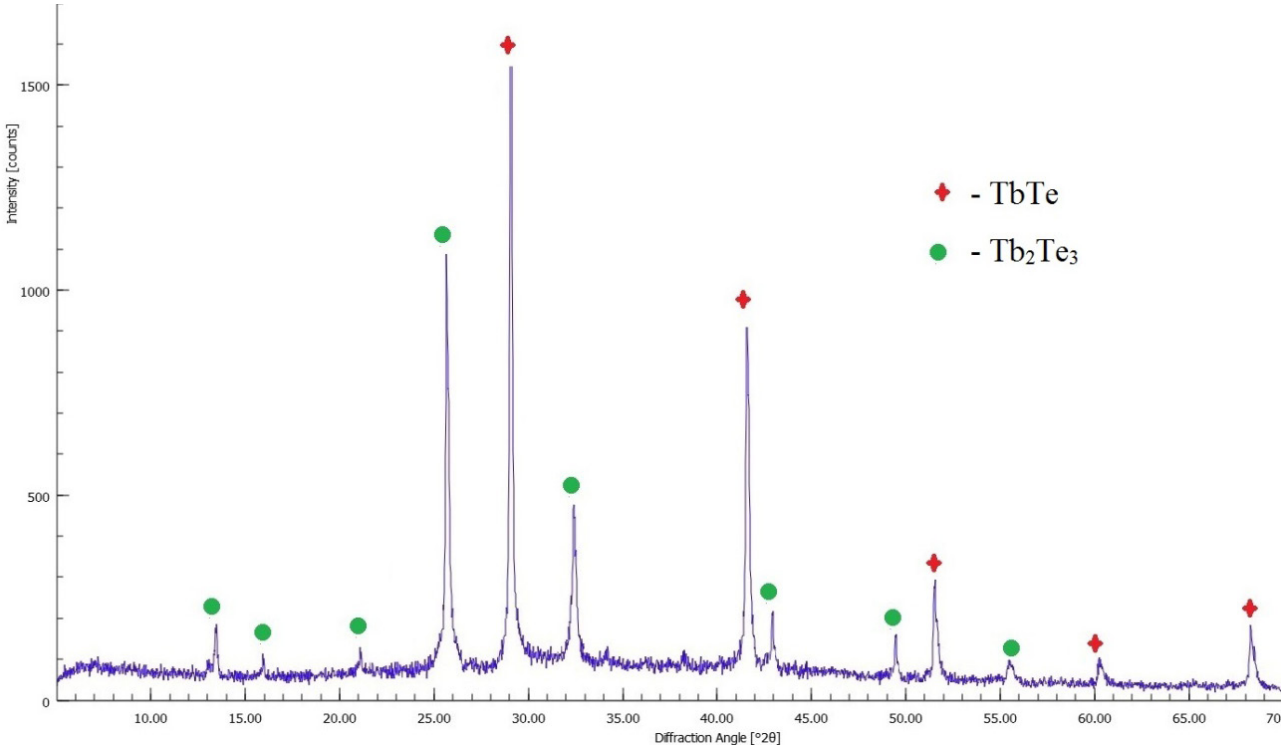

Fig. 1. The powder X-ray diffraction pattern of an alloy from $TbTe_3$+Tb_2Te_3 two-phase regions

Since the electrolyte should not contain moisture and oxygen, the glycerol was thoroughly dried and degassed by evacuation at ~450 K.

The EMF method with glycerol electrolyte has been successfully used for many years for the thermodynamic study of a number of binary and ternary chalcogenide systems [20–26].

The detailed descriptions of the methods for the preparation of the electrodes and electrolyte and assembly of the electrochemical cell were described in studies [20, 21, 25].

The EMF measurements were carried out using a Keithley Model 193 high-resistance digital voltmeter. The temperature of the electrochemical cells was measured with chromel-alumel thermocouples and a mercury thermometer with an accuracy of 0.5 K.

The first equilibrium EMF values were obtained after keeping the cell at ~400 K for 40–60 h, while the subsequent EMF values were obtained after 3–4 h when reaching the desired temperature. The EMF values were considered equilibrium values if they did not differ from each other at repeated measurements at a given temperature by more than 0.2 mV, regardless of the direction of the temperature change. During the experiments, the EMF of each sample was measured 2–3 times at two selective temperatures in order to control the reversibility of the cell.

Taking into account the results of our previous studies of Ln-Te systems by the EMF method [22, 26], we used the cell of type (1) only for study alloys from the TbTe + Tb_2Te_3 region, and reproducible results for both electrode-alloys were obtained. For other phase regions, type (2) cells were used and the reproducible results were obtained. From each heterogeneous region, two alloys were examined. The EMF measurements for two alloys from the same heterogeneous region coincided with an accuracy of 0.5 mV.

3. Results and discussion

The obtained temperature dependences of the EMF for all studied alloys of the Tb-Te system were linear (Fig. 2), which allowed performing thermodynamic calculations using the least-squares method. Calculations were performed using the Microsoft Office Excel 2003 computer program. The obtained linear equations are presented in Table 1 in the form:

$$E = a + bT \pm t\left[\frac{S_E^2}{n} + \frac{S_E^2(T-\overline{T})^2}{\sum(T_i-\overline{T})^2}\right]^{\frac{1}{2}}, \quad (3)$$

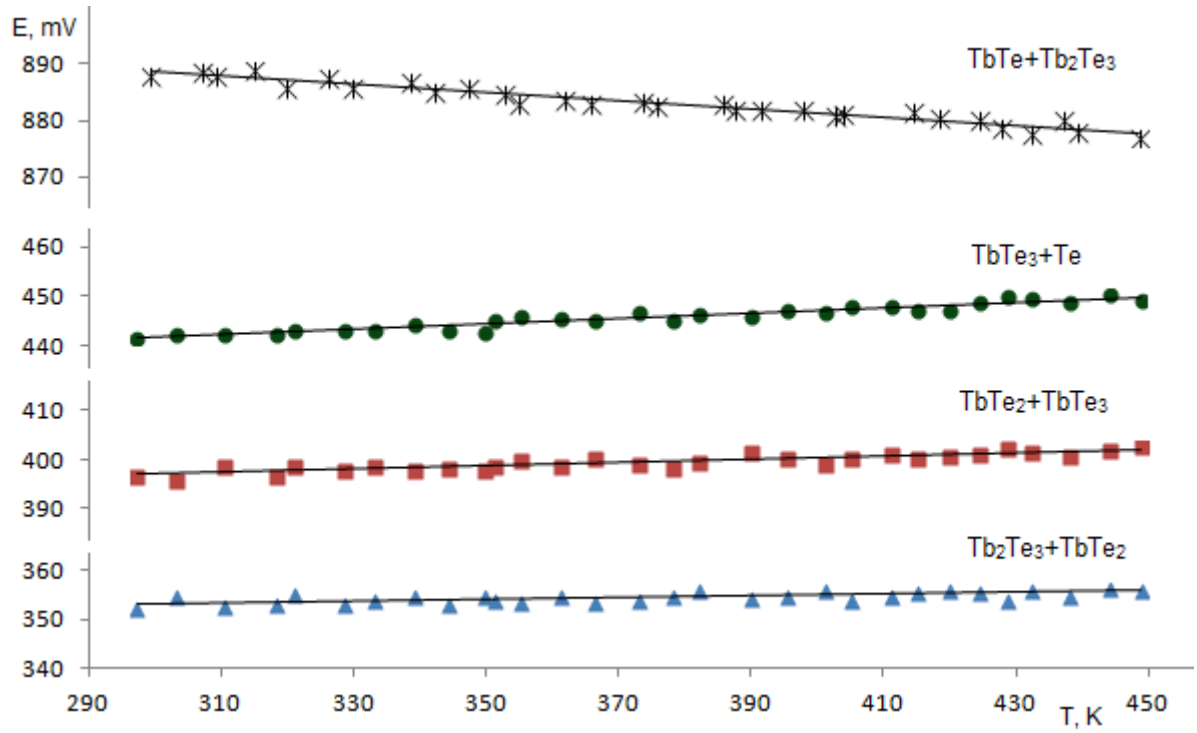

Fig. 2. Temperature dependencies of EMF for alloys of the TbTe+ Tb_2Te_3 (cell of type (1)) and Tb_2Te_3+$TbTe_2$, $TbTe_2$+$TbTe_3$, $TbTe_3$+Te (cell of type (2)) phase regions of the Tb-Te system

Table 1. Relations between EMF and the temperature for type (1)* and (2) cells in some phase regions of the Tb-Te system in the temperature range of 300–450 K

№	Phase region	E, mV $= a + bT \pm 2[S_E^2/n + S_b^2(T-\overline{T})]^{1/2}$
1	$TbTe_3$+Te	$348.29 + 0.01664T \pm 2\left[\frac{0.67}{30} + 1.13\cdot10^{-5}(T-375.62)\right]^{1/2}$
2	$TbTe_2$+$TbTe_3$	$386.99 + 0.03379T \pm 2\left[\frac{0.62}{30} + 1.05\cdot10^{-5}(T-375.62)\right]^{1/2}$
3	Tb_2Te_3+$TbTe_2$	$425.19 + 0.05492T \pm 2\left[\frac{0.53}{30} + 8.9\cdot10^{-6}(T-375.62)\right]^{1/2}$
4	*TbTe+Tb_2Te_3	$910.32 - 0.07214T \pm 2\left[\frac{0.69}{30} + 1.18\cdot10^{-5}(T-374.89)\right]^{1/2}$

where a and b – empirical constants; n – is the number of pairs of T and E values; S_E – the error variance of the EMF measurements; $\overline{T}$ – the average of the absolute temperature; t – the Student's t-test. At the confidence level of 95 % and $n = 30$, the Student's t-test ⩽ 2.

From the obtained equations (Table 1) according to the relations [20, 21]:

$$\Delta\overline{G}_i = -zFE, \quad (4)$$

$$\Delta\overline{S}_i = zF\left(\frac{\partial E}{\partial T}\right)_P = zFb, \quad (5)$$

$$\Delta\overline{H}_i = -zF\left[E - T\left(\frac{\partial E}{\partial T}\right)_P\right] = -zFa. \quad (6)$$

the partial molar Gibbs free energy, enthalpy, and entropy of TbTe in two-phase alloys Tb_2Te_3+$TbTe_2$, $TbTe_2$+$TbTe_3$, and $TbTe_3$+Te (Table 2) and terbium in alloys TbTe+Tb_2Te_3 (Table 3) were calculated.

The values given in Table 2 represent the difference between the corresponding partial molar functions of terbium for the right and left electrodes of the type (2) cell. For example,

Table 2. Relative partial molar functions of TbTe in the alloys of the Tb-Te system at 298 K

Фазовая область	$-\Delta\bar{G}_{TbTe}$	$-\Delta\bar{H}_{TbTe}$	$\Delta\bar{S}_{TbTe}$ J/(mol·K)
	кJ/mol		
$TbTe_3$+Te	127.82±0.15	123.08±0.65	15.90±1.72
$TbTe_2$+$TbTe_3$	114.94±0.17	112.02±0.71	9.78±1.87
Tb_2Te_3+$TbTe_3$	102.26±0.17	100.82±0.74	4.82±1.95

Table 3. Relative partial molar functions of terbium in the alloys of the Tb-Te system at 298 K

Phase region	$-\Delta\bar{G}_{Tb}$	$-\Delta\bar{H}_{Tb}$	$\Delta\bar{S}_{Tb}$ J/(mol·K)
	кJ/mol		
$TbTe_3$	385.10±0.33	386.58±1.40	−4.96±3.71
$TbTe_2$	372.22±0.35	375.52±1.46	−11.07±3.86
Tb_2Te_3	359.54±0.35	364.32±1.49	−16.03±3.94
TbTe	257.28±0.18	263.50±0.75	−20.88±1.99

$$\Delta\bar{G}_{TbTe}(TbTe_{1+x}) = \Delta\bar{G}_{Tb}\ (TbTe_{1+x}) - \Delta\bar{G}_{Tb}(TbTe)\,. \quad (7)$$

and

$$\Delta\bar{G}_{Tb}(TbTe_{1+x}) = \Delta\bar{G}_{TbTe}(TbTe_{1+x}) + \Delta\bar{G}_{Tb}(TbTe)\,. \quad (8)$$

The partial molar functions of terbium in $TbTe_{1+x}$ alloys (right electrodes of type (2) cell) were calculated using the relation (8) and are presented in Table 3. 3.

The phase compositions of alloys (Table 3) of indicated two-phase region show that the partial molar functions of terbium in them are the thermodynamic characteristics of the following potential formation reactions (the state of substances is crystalline):

Tb + 3Te = $TbTe_3$
Tb + 2$TbTe_3$ = 3$TbTe_2$
Tb + 3$TbTe_2$ = 2Tb_2Te_3
Tb + Tb_2Te_3 = 3TbTe

Therefore, the standard thermodynamic functions of the formation of terbium tellurides can be calculated using the relations

$$\Delta Z^0(TbTe_3) = \Delta\bar{Z}_{Tb},$$

$$\Delta Z^0(TbTe_2) = \frac{1}{3}\Delta\bar{Z}_{Tb} + \frac{2}{3}\Delta Z^0(TbTe_3),$$

$$\Delta Z^0(Tb_2Te_3) = 0.5\Delta\bar{Z}_{Tb} + 1.5\Delta Z^0(TbTe_2),$$

$$\Delta Z^0(TbTe) = \frac{1}{3}\Delta\bar{Z}_{Tb} + \frac{1}{3}\Delta Z^0(Tb_2Te_3),$$

where $Z \equiv G, H, S$, while the standard entropies were calculated as

$$S^0(TbTe_3) = [\Delta\bar{S}_{Tb} + S^0(Tb)] + 3S^0(Te),$$

$$S^0(TbTe_2) = \frac{1}{3}[\Delta\bar{S}_{Tb} + S^0(Tb)] + \frac{2}{3}S^0(TbTe_3),$$

$$S^0(Tb_2Te_3) = 0.5[\Delta\bar{S}_{Tb} + S^0(Tb)] + 1.5S^0(TbTe_2),$$

$$S^0(TbTe) = \frac{1}{3}[\Delta\bar{S}_{Tb} + S^0(Tb)] + \frac{1}{3}S^0(Tb_2Te_3).$$

For the thermodynamic calculations, in addition to our experimental data (Table 3), we used the literature data [28] on the standard entropies of elemental terbium (73.51±0.42 кJ/mol) and tellurium (49.50±0.21 кJ/mol). The results are presented in Table 4. In all cases, the standard uncertainties were calculated by accumulation of errors method.

Table 4 shows the estimated data for the TbTe and Tb_2Te_3 compounds given in [17, 18].

4. Conclusions

We have presented the results of a comprehensive study of solid-phase equilibria in the Tb-Te system and the thermodynamic properties of terbium tellurides by EMF and XRD methods. The compounds TbTe, Tb_2Te_3, $TbTe_2$, and $TbTe_3$ were revealed in the system based on the experimental data. The partial thermodynamic functions of TbTe and Tb in alloys have been determined based on EMF measurements of types (1) and (2) concentration cells in the 300–450 K temperature range. The standard thermodynamic functions of formation and the standard entropies of the

Table 4. Standard integral thermodynamic functions of terbium tellurides

Compound	$-\Delta_f G^0$(298 K)	$-\Delta_f H^0$(298 K)	ΔS^0(298 K)	S^0(298 K)
	кJ/mol		J/(mol·K)	
$TbTe_3$	385.1±0.3	386.6±1.4	−5.0±3.7	194.9±4.8
$TbTe_2$	380.8±0.4	382.9±1.5	−7.0±3.8	165.6±4.6
Tb_2Te_3	750.98±0.7	756.5±3.0	−18.5±7.8	277.0±9.3
	–	795±125 [17]		264±21 [17]
	803.5	818 [19]		247.6 [19]
TbTe	336.1±0.3	340.0±1.3	−13.13.3	109.9±3.9
		314±63 [17]		97±10 [17]

TbTe, Tb_2Te_3, $TbTe_2$, and $TbTe_3$ compounds were calculated by the combination of these data.

Acknowledgement

The work has been carried out within the framework of the international joint research laboratory "Advanced Materials for Spintronics and Quantum Computing" (AMSQC) established between the Institute of Catalysis and Inorganic Chemistry of ANAS (Azerbaijan) and Donostia International Physics Center (Basque Country, Spain) and partially supported by the Science Development Foundation under the President of the Republic of Azerbaijan, grant EİF/MQM/Elm-Tehsil-1-2016-1(26)-71/01/4-M-33.

Conflict of interests

The authors declare that they have no known competing financial interests or personal relationships that could have influenced the work reported in this paper.

References

1. Jha A. R. *Rare earth materials: properties and applications*. United States. CRC Press. 2014. 371 p. DOI: https://doi.org/10.1201/b17045

2. Balaram V. Rare earth elements: A review of applications, occurrence, exploration, analysis, recycling, and environmental impact. *Geoscience Frontiers*. 2019;10(4): 1285–1290. DOI: https://doi.org/10.1016/j.gsf.2018.12.005

3. *Yarembash E. I., Eliseev A. A.* Khal'kogenidy redkozemel'nykh elementov [*Chalcogenides* of *rare earth* elements). Moscow: Nauka Publ.; 1975. 258p. (In Russ.)

4. Y-Sc., La-Lu. *Gmelin Handbock of Inorganic Chemistry*. In: Hartmut Bergmann (Ed.), Rare Earth Elements, 8th Edition, Springer-Verlag Heidelberg GmbH. Berlin; 1987.

5. Muthuselvam I. P., Nehru R., Babu K. R., Saranya K., Kaul S. N., Chen S-M, Chen W-T, Liu Y., Guo G-Y, Xiu F., Sankar R. Gd_2Te_3 an antiferromagnetic semimetal. *J. Condens. Matter Phys.* 2019;31(28): 285802-5. DOI: https://doi.org/10.1088/1361-648X/ab1570

6. Huang H., Zhu J.-J. The electrochemical applications of rare earth-based nanomaterials. *Analyst.* 2019;144(23): 6789–6811. DOI: https://doi.org/10.1039/C9AN01562K

7. Saint-Paul M., Monceau P. Survey of the thermodynamic properties of the charge density wave systems. *Adv. Cond. Matter Phys*. 2019: 1–5 DOI: https://doi.org/10.1155/2019/2138264

8. Cheikh D., Hogan B. E., Vo T., Allmen P. V., Lee K., Smiadak D. M., Zevalkink A., Dunn B. S., Fleurial J-P., Bux S. L. Praseodymium telluride: A high temperature, high- ZT thermoelectric material. *Joule*. 2018; 2(4): 698–709. DOI: https://doi.org/10.1016/j.joule.2018.01.013

9. Patil S. J., Lokhande A. C., Lee D. W, Kim J. H., Lokhande C. D. Chemical synthesis and supercapacitive properties of lanthanum telluride thin film. *Journal of Colloid and Interface Science*. 2017; 490: 147–153. DOI: https://doi.org/10.1016/j.jcis.2016.11.020

10. Zhou X. Z., Zhng K. H. L, Xiog J., Park J-H, Dickerson J-H., He W. Size- and dimentionality dependent optical, mahnetic and magneto-optical properties of binary europium-based nanocrystals: EuX (X=O, S, Se, Te). *Nanotechnology*. 2016;27**(**19): 192001-5. DOI: https://doi.org/10.1088/0957-4484/27/19/192001

11. Okamoto H. *Desk handbook phase diagram for binary alloys*. ASM International. 2000. 900 p.

12. Babanly M. B., Mashadiyeva L. F., Babanly D. M., Imamaliyeva S. Z., Tagiyev D. B., Yusibov Y. A.. Some issues of complex studies of phase equilibria and thermodynamic properties in ternary chalcogenide systems involving Emf measurements. *Russian Journal of Inorganic Chemistry*. 2019;64(13): 1649–1672. DOI: https://doi.org/10.1134/s0036023619130035

13. Imamaliyeva S. Z., Babanly D. M., Tagiev D. B., Babanly M. B. Physicochemical aspects of development of multicomponent chalcogenide phases having the Tl_5Te_3 structure. A review. *Russian Journal of Inorganic Chemistry*2018;63(13): 1703–1724 DOI: https://doi.org/10.1134/s0036023618130041

14. Massalski T. B. Binary alloys phase diagrams, second edition. ASM International, Materials Park. Ohio; 1990. 3835 p. DOI: https://doi.org/10.1002/adma.19910031215

15. *Diagrammi sostoyaniya dvoynikh metallicheskikh system* [Diagrams of Binary Metallic Systems] *Handbook* in 3 vols. Lyakishev N.P. (Ed.) Moscow: Mashinostroenie Publ.; 1996, 1997, 2001. (In Russ.)

16. Eliseev A. A., Orlova I. G., Martynova L. F., Pechennikov A. V., Chechernikov V. I. Paramagnetism of some terbium chalcogenides. *Inorganic Materials*. 1987;23: 1833–1835.

17. Mills K. C. *Thermodynamic data for inorganic sulphides, selenides, and tellurides*. London: Butterworth; 1974. 854 p.

18. Vassiliev V. P., Lysenko V. A. Gaune-Escard M. Relationship of thermodynamic data with periodic law. *Pure and Applied Chemistry*. 2019;91(6): 879–884. DOI: https://doi.org/10.1515/pac-2018-0717

19. Vassiliev V. P., Lysenko V. A. New approach for the study of thermodynamic properties of lanthanide compounds. *Electrochimica Acta*. 2016;222: 1770–1775. DOI: https://doi.org/10.1016/j.electacta.2016.11.075

20. Morachevsky A. G., Voronin G. F., Geyderich V. A., Kutsenok I. B. *Elektrokhimicheskie metody issledovaniya v termodinamike metallicheskikh system*. [Electrochemical methods of investigation in hermodynamics of metal systems]. Moscow: Akademkniga Publ.; 2003. 334 p. Available at: https://elibrary.ru/item.asp?id=19603291 (In Russ.)

21. Babanly M. B., Yusibov Y. A. *Elektrokhimicheskie metody v termodinamike neorganicheskikh sistem* [Electrochemical methods in thermodynamics of inorganic systems]. Baku: BSU Publ.; 2011. 306 p.

22. Imamaliyeva S. Z., Mehdiyeva I. F., Taghiyev D. B. et al. Thermodynamic investigations of the erbium tellurides by EMF method. *Physics and Chemistry of Solid State*. 2020;21(2): 312–318. DOI: https://doi.org/10.15330/pcss.21.2.312-318

23. Hasanova G. S., Aghazade A. I., Yusibov Yu. A., Babanly M. B. Thermodynamic investigation of the Bi_2Se_3-Bi_2Te_3 system by the EMF method. *Kondensirovannye sredy i mezhfaznye granitsy = Condensed Matter and Interphases*. 2020;22(3): 310–319. DOI: https://doi.org/10.17308/kcmf.2020.22/2961

24. Imamaliyeva S. Z., Babanly D. M., Gasanly T. M., et al.: Thermodynamic properties of Tl_9GdTe_6 and $TlGdTe_2$. *Russian Journal of Physical Chemistry A*. 2018;92(11): 2111–2116. DOI: https://doi.org/10.1134/s0036024418110158

25. Mansimova S. H., Orujlu E. N., Sultanova S. G., Babanly M. B. Thermodynamic properties of $Pb_6Sb_6Se_{17}$. *Kondensirovannye sredy i mezhfaznye granitsy = Condensed Matter and Interphases*. 2017;19(4): 536–541. https://doi.org/10.17308/kcmf.2017.19/234

26. Imamaliyeva S. Z., Gasanly T. M., Mahmudova M. A. Thermodynamic properties of GdTe compound. *Physics*. 2017;22: 19–21. Available at: http://physics.gov.az/Dom/2017/AJP_Fizika_04_2017_en.pdf

27. Imamaliyeva S. Z., Musayeva S. S., Babanly D. M., Jafarov Y. I., Tagiyev D. B., Babanly M. B. Determination of the thermodynamic functions of bismuth chalcoiodides by EMF method with morpholinium formate as electrolyte. *Thermochim. Acta*. 2019; 679: 178319–17825. DOI: https://doi.org/10.1016/j.tca.2019.178319

28. *Baza dannykh termicheskikh konstant veshchestv. Elektronnaya versiya pod. red. V. S. Yungmana. 2006* [Database of thermal constants of substances. Electronic version V. S. Yungman (ed.). 2006]. Available at: http://www.chem.msu.ru/cgi-bin/tkv.pl?show=welcome.html/welcome.html

Information about the authors

Samira Z. Imamaliyeva, PhD in Chemistry, Assistance Professor, Institute of Catalysis and Inorganic Chemistry, Azerbaijan National Academy of Sciences, Baku, Azerbaijan; e-mail: samira9597a@gmail.com. ORCID iD: https://orcid.org/0000-0001-8193-2122.

Dunya M. Babanly, DSc in Chemistry, Assistance Professor, Institute of Catalysis and Inorganic Chemistry, Azerbaijan National Academy of Sciences, Azerbaijan State Oil and Industry University, Baku, Azerbaijan; e-mail: dunya.babanly@ufaz.az. ORCID iD: https://orcid.org/0000-0002-8330-7854.

Vladimir P. Zlomanov, DSc in Chemistry, Professor, Lomonosov Moscow State University, Moscow, Russian Federation; e-mail: zlomanov1@mail.ru ORCID iD: https://orcid.org/0000-0002-0327-4715.

Dilgam B. Taghiyev, Academician of the Azerbaijan National Academy of Sciences, Director of the Institute of Catalysis and Inorganic Chemistry, Azerbaijan National Academy of Sciences, Baku, Azerbaijan; e-mail: dtagiyev@rambler.ru ORCID iD: https://orcid.org/0000-0002-8312-2980.

Mahammad B. Babanly, DSc in Chemistry, Professor, Corresponding Member of the Azerbaijan National Academy of Sciences, Deputy-director of the Institute of Catalysis and Inorganic Chemistry, Azerbaijan National Academy of Sciences, Baku State University, Baku, Azerbaijan; e-mail: babanlymb@gmail.com. ORCID iD: https://orcid.org/0000-0001-5962-3710 .

All authors have read and approved the final manuscript.

Translated by Valentina Mittova
Edited and proofread by Simon Cox

Condensed Matter and Interphases
(Kondensirovannye sredy i mezhfaznye granitsy)

Original articles

DOI: https://doi.org/10.17308/kcmf.2020.22/3117
Received 27 Novermber 2020
Accepted 15 December 2020
Published online 25 December 2020

ISSN 1606-867X
eISSN 2687-0711

New Thallium Tellurides with Rare Earth Elements

© 2020 S. Z. Imamaliyeva✉

Institute of Catalysis and Inorganic Chemistry of the Azerbaijan National Academy of Sciences,
113 H. Javid ave., Baku AZ-1143, Azerbaijan

Abstract

Compounds of the Tl_4LnTe_3 (Ln-Nd, Sm, Tb, Er, Tm) composition were synthesized by the direct interaction of stoichiometric amounts of thallium telluride Tl_2Te elementary rare earth elements (REE) and tellurium in evacuated (10^{-2} Pa) quartz ampoules. The samples obtained were identified by differential thermal and X-ray phase analyses. Based on the data from the heating thermograms, it was shown that these compounds melt with decomposition by peritectic reactions. Analysis of powder diffraction patterns showed that they were completely indexed in a tetragonal lattice of the Tl_5Te_3 type (space group *I*4/*mcm*). Using the Le Bail refinement, the crystal lattice parameters of the synthesized compounds were calculated. It was found that when the thallium atoms located in the centres of the octahedra were substituted by REE atoms, there occurred a sharp decrease in the a parameter and an increase in the c parameter. This was due to the fact that the substitution of thallium atoms with REE cations led to the strengthening of chemical bonds with tellurium atoms. This was accompanied by some distortion of octahedra and an increase in the c parameter. A correlation between the parameters of the crystal lattices and the atomic number of the lanthanide was revealed: during the transition from neodymium to thulium, there was an almost linear decrease in both parameters of the crystal lattice, which was apparently associated with lanthanide contraction. The obtained new compounds complement the extensive class of ternary compounds - structural analogues of Tl_5Te_3 and are of interest as potential thermoelectric and magnetic materials.

Keywords: thallium tellurides – REE, structural analogues of Tl_5Te_3, differential thermal analysis, X-ray phase analysis, crystal structure.

Funding: The work has been carried out within the framework of the international joint research laboratory "Advanced Materials for Spintronics and Quantum Computing" (AMSQC) established between the Institute of Catalysis and Inorganic Chemistry of ANAS (Azerbaijan) and Donostia International Physics Center (Basque Country, Spain) and partially supported by the Science Development Foundation under the President of the Republic of Azerbaijan, a grant EİF/MQM/Elm-Tehsil-1-2016-1(26)-71/01/4-M-33.

For citation: Imamaliyeva S. Z. New thallium tellurides with rare earth elements. *Kondensirovannye sredy i mezhfaznye granitsy = Condensed Matter and Interphases*. 2020; 22 (4): 460–465. DOI: https://doi.org/10.17308/kcmf.2020.22/3117

Для цитирования: Имамалиева С. З. Новые теллуриды таллия с редкоземельными элементами. *Конденсированные среды и межфазные границы*. 2020; 22(4): 460–465. DOI: https://doi.org/10.17308/kcmf.2020.22/3117

✉ Samira Zakir Imamalieva, e-mail: samira9597a@gmail.com

1. Introduction

One of the rational ways to develop new functional materials is the search for complex structural analogues of already known compounds with the same properties and to optimize their characteristics by directional alloying [1–5].

Subtelluride Tl_5Te_3 is one of the most suitable matrix compounds for the preparation of new ternary compounds – structural analogues and multicomponent phases. According to the phase diagram of the Tl-Te system [6, 7], this compound melts congruently at 725 K and is a variable composition phase with a wide range of homogeneity (34.5÷38 at% Te). Due to the peculiarities of the crystal structure [8, 9], Tl_5Te_3 has a number of ternary cation- and anion-substituted structural analogies.

In studies [10, 11] a new class of compounds – thallium tellurides of REE type Tl_9LnTe_6, which are ternary structural analogues of Tl_5Te_3 was obtained. These compounds complement the extensive class of ternary compounds with general formulas Tl_9AX_6 and Tl_4BX_3 (A – Sb, Bi, Au, In; B – Sn, Pb, Mo, Cu; X – Se, Te) [13–19]. The described compounds are thermoelectric with anomalously low thermal conductivity [20–23], and some of them exhibit optical [24–26] and magnetic [27, 28] properties, as well as the properties of topological insulators [29–31].

As was shown above, Tl_5Te_3 crystallizes in a tetragonal structure of the Cr_5B_3 type (Sp.Gr. *I4/mcm*) (Fig. 1a) [8, 9]. The crystal structure of Tl_5Te_3 was described in detail in studies [5, 8, 9, 32]. In the crystal lattice of Tl_5Te_3, thallium atoms occupy two different positions and exhibit oxidation states +1 and +3. Some of the thallium atoms (Tl2) are located in octahedral voids, and others (Tl1) are located in the voids of the anionic tellurium cage. Replacement of half of the thallium atoms located at the centres of octahedra (Tl2) with B^{+3} cations led to the formation of compounds of the Tl_9BTe_6 type, and their complete replacement by A^{+2} cations led to the formation of compounds of the Tl_4ATe_3 type.

It is known that lanthanides exhibit oxidation states +2 and +3. In compounds of the Tl_9LnTe_6 type, lanthanides exhibit an oxidation state of +3. Considering the existence of compounds of the $Tl_4A^{IV}X_3$ type, we assumed the possibility of the formation of compounds with the composition Tl_4LnTe_3, in which the REE will exhibit an oxidation state of +2. In the study [12], for the first time we synthesized and identified Tl_4GdTe_3 and Tl_4DyTe_3 compounds - representatives of the specified class, their isostructurality with Tl_5Te_3 was confirmed and the parameters of their crystal lattices were calculated.

In this study, we continued our research in the field of REE thallium chalcogenides and report on the synthesis of some new compounds of the Tl_4LnTe_3 type.

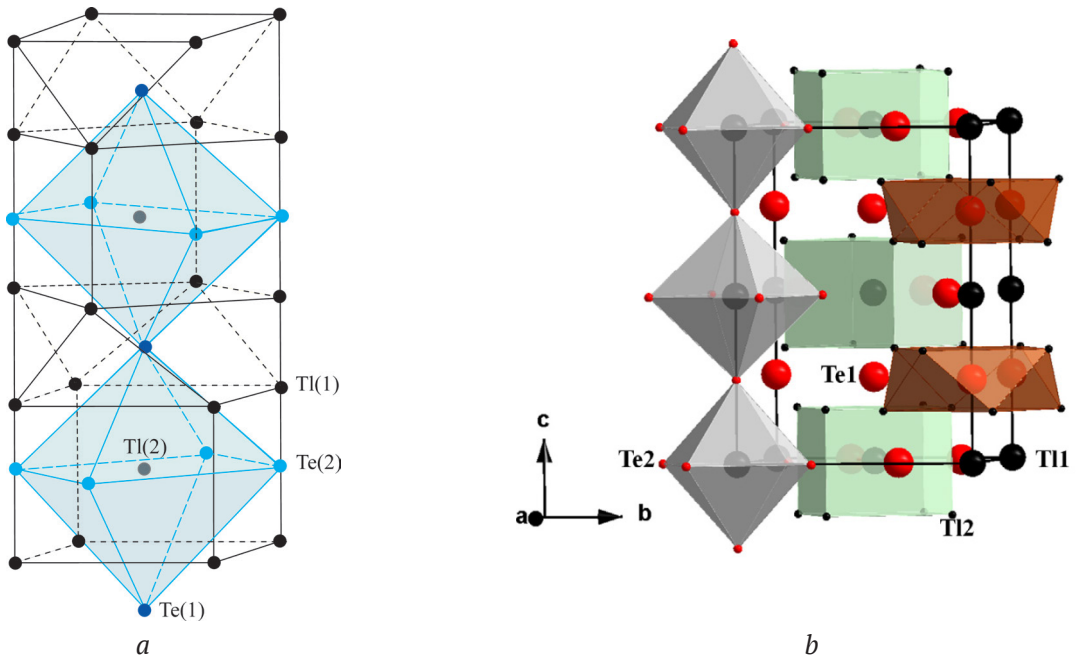

a *b*

Fig. 1. Crystal structure of Tl_5Te_3. Main structural element (a) [5], projected onto a plane *b, c* (b) [28]

2. Experimental

2.1. Materials and synthesis

High-purity elements purchased from Alfa Aesar were used for the studies: thallium (catalogue number 7440-28-0), tellurium (13494-80-9), neodymium (7440-00-8), samarium (7440-19-9), terbium (7440-27-9), erbium (7440-52-0), thulium (7440-30-4).

Thallium was stored in water in order to prevent oxidation in air, therefore it was dried immediately before use. Due to the toxicity of thallium and its compounds, protective gloves were used during performed work.

Considering the previous experience in the synthesis of Tl_9LnTe_6 and Tl_4LnTe_3 compounds [31–34], namely, the incongruent nature of their melting and the refractoriness of the REE, Tl_4LnTe_3 compounds were synthesized by a ceramic method using a special technique. In the synthesis, not elementary components, but stoichiometric amounts of thallium telluride Tl_2Te, lanthanide, and tellurium were used since lanthanides with thallium form thermodynamic stable compounds that prevent further synthesis of ternary compounds. Fusion was performed in the evacuated (10^{-2} Pa) quartz ampoules. After fusion at 1000 K, to bring the alloys to a state as close as possible to equilibrium, the cast non-homogenized ingots were ground into powder in an agate mortar, thoroughly mixed, pressed into a cylindrical tablet, and annealed at 700 K for 1000 h.

In order to prevent the interaction of lanthanides with the inner walls of the quartz ampoule, the synthesis of the compounds was carried out in graphitized ampoules. Graphitization was performed by the thermal decomposition of toluene.

The single-phase of the synthesized compounds was monitored by DTA and XRD methods.

2.2. Methods

The studies were carried out by the methods of differential thermal (DTA) and X-ray phase diffraction analyses (XRD). Heating curves were recorded using differential scanning calorimeter DSC NETZSCH 404 F1 Pegasus system and multichannel DTA device based on an electronic TC-08 Thermocouple Data Logger in the temperature range from room temperature to ~ 1300 K. Powder diffraction patterns of the initial compounds and intermediate alloys were recorded on a diffractometer D2 Phaser with CuK_α-radiation within an angle range of $2\theta = 10 \div 70°$. The crystal lattice parameters of the initial compounds and intermediate alloys were determined by the indexing of powder diffraction patterns using the Topas 4.2 software by the *Le Bail method*.

3. Results

A comparison of powder diffraction patterns of synthesized samples of composition Tl_4LnTe_3 with Tl_5Te_3 and its typical triple analogue Tl_4PbTe_3 showed that they all have qualitatively the same diffraction pattern (Fig. 2). All reflection lines were fully indexed in the Tl_5Te_3 structure type (Sp.Gr. *I4/mcm*).

The parameters of the tetragonal lattices of Tl_4LnTe_3that were determined using the computer program Topas V4.2 using the Le Bail refinement are shown in the Table. The Table also contains data for other members of this class of compounds. Data in the Table demonstrate that the substitution of thallium (Tl2) atoms located at the centres of tellurium octahedra (Fig. 1) with REE atoms led to a sharp decrease in parameter *a* and an increase in parameter *c*. Probably, this was due to the fact that such a substitution led to the strengthening of chemical bonds between the REE and Te atoms (2) and a decrease in the corresponding interatomic distances, determining the value of parameter *a*. As a result, some distortion of tellurium octahedra occurred, which led to an increase in parameter *c*.

The dependences of the crystal lattice parameters of Tl_4LnTe_3 compounds from the atomic number of the lanthanide is shown in Fig. 3. As can be seen, there is a clear correlation: during the transition from neodymium to thulium, there is an almost linear decrease in both crystal lattice parameters, which is probably associated with a decrease in the crystallographic radius of REE due to lanthanide contraction [33].

The thermogram of heating each of the synthesized compounds in the temperature range from room temperature to 1300 K contained one clear endothermic effect at 760–775 K (Table). Taking into account the difficulty of homogenizing the samples obtained by fusion and the complex picture on the DTA cooling curves, these effects cannot be attributed to the congruent melting point. Probably, these compounds melt with decomposition by peritectic reactions, and their complete transition to a liquid state occurs at temperatures above 1300 K.

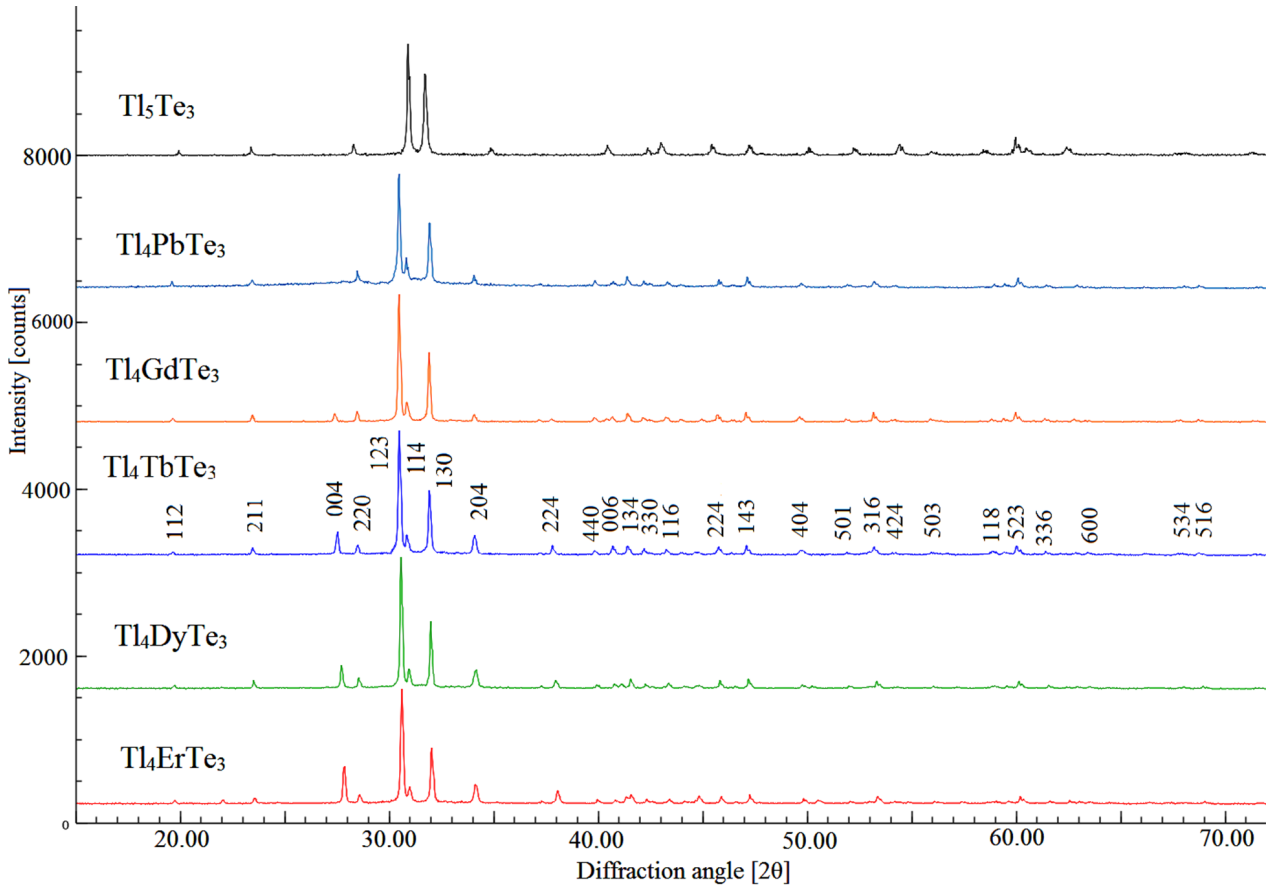

Fig. 2. Powder diffraction patterns of some compounds of the Tl_4LnTe_3 type

Table. Crystallographic parameters of Tl_5Te_3 and its ternary structural analogues of the $Tl_4A^{IV}Te_3$ type

Phase	Tetragonal lattice parameters, Sp.Gr. *I4/mcm*, Z = 4		Melting points	Source
	a, Å	*c*, Å		
Tl_5Te_3	8.930	12.598	725	[8]
Tl_4SnTe_3	8.820	13.010	823	[15]
Tl_4PbTe_3	8.841	13.056	893	[15]
Tl_4CuTe_3	8.929	12.603	–	[17]
Tl_4MoTe_3	8.930	12.575	–	[18]
Tl_4NdTe_3	8.8885(7)	13.0952(12)	775	present study
Tl_4SmTe_3	8.8752(6)	13.0784(11)	772	present study
Tl_4GdTe_3	8.8766(7)	13.0756(13)	770	[12]
Tl_4TbTe_3	8.8652(7)	13.0653(12)	768	present study
Tl_4DyTe_3	8.8588(7)	13.0524(16)	767	[12]
Tl_4ErTe_3	8.8421(6)	13.0334(11)	760	present study
Tl_4TmTe_3	8.8354(7)	13.015(15)	760	present study

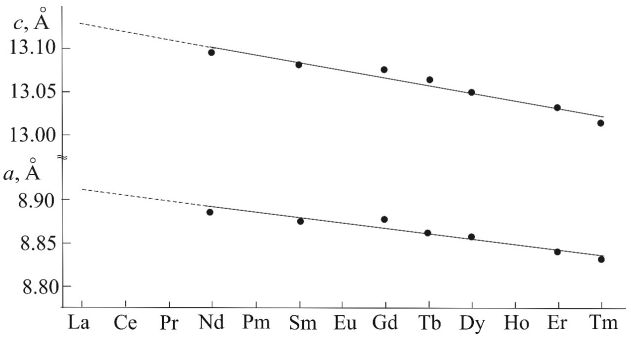

Fig. 3. Correlation between crystal lattice parameters of the Tl_4LnTe_3 type compounds and the atomic number of the lanthanide

4. Conclusion

In this study, we reported the synthesis of new ternary compounds of the Tl_4LnTe_3 (Ln-Nd, Sm, Tb, Er, Tm) type, which are structural analogues of Tl_5Te_3. Powder diffraction patterns of all synthesized compounds were completely indexed in the tetragonal structure (Sp.Gr. *I*4/*mcm*), the parameters of their crystal lattices were calculated. According to DTA data, it was found that the synthesized compounds melt with decomposition by peritectic reactions. A comparison of the results obtained with the literature data was carried out. A correlation between the parameters of the crystal lattice and the atomic number of the lanthanide was revealed. The obtained new compounds complement a wide class of compounds, which are structural analogues of Tl_5Te_3, and are of interest as potential thermoelectric and magnetic materials.

Acknowledgments

The author expresses her gratitude to the Corresponding Member of the Azerbaijan National Academy of Sciences, Professor Mahammad Babanly and Associate Professor Vagif Gasymov for their help with X-ray analysis and useful discussions.

The work has been carried out within the framework of the international joint research laboratory "Advanced Materials for Spintronics and Quantum Computing" (AMSQC) established between the Institute of Catalysis and Inorganic Chemistry of ANAS (Azerbaijan) and Donostia International Physics Center (Basque Country, Spain) and partially supported by the Science Development Foundation under the President of the Republic of Azerbaijan, a grant EİF/MQM/Elm-Tehsil-1-2016-1(26)-71/01/4-M-33.

Conflict of interests

The author declares that she has no known competing financial interests or personal relationships that could have appeared to influence the work reported in this paper.

References

1. Berger L. I., Prochukhan V. D. *Troinye almazopodobnye poluprovodniki* [Ternary diamond-like semiconductors]. Moscow: Metallurgiya; 1968. 151 p. (In Russ.)

2. Villars P, Prince A. Okamoto H. *Handbook of ternary alloy phase diagrams (10 volume set)*. Materials Park, OH: ASM International; 1995. 15000 p.

3. Tomashyk V. N. *Multinary Alloys Based on III-V Semiconductors*. CRC Press; 2018. 262 p. DOI: https://doi.org/10.1201/9780429055348

4. Babanly M. B., Chulkov E. V., Aliev Z. S. et al. Phase diagrams in materials science of topological insulators based on metal chalkogenides. *Russian Journal of Inorganic Chemistry*. 2017;62(13): 1703–1729. DOI: https://doi.org/10.1134/S0036023617130034

5. Imamaliyeva S. Z., Babanly D. M., Tagiev D. B., Babanly M. B. Physicochemical aspects of development of multicomponent chalcogenide phases having the Tl_5Te_3 structure. A Review. *Russian Journal of Inorganic Chemistry*. 2018;63(13): 1703–1724 DOI: https://doi.org/10.1134/s0036023618130041

6. Asadov M. M., Babanly M. B., Kuliev A. A. Phase equilibria in the system Tl–Te. *Izvestiya Akademii Nauk SSSR, Neorganicheskie Materialy*. 1977;13(8): 1407–1410.

7. Okamoto H. Te-Tl (Tellurium-Thallium). *Journal of Phase Equilibria*. 2001;21(5): 501. DOI: https://doi.org/10.1361/105497100770339833

8. Schewe I., Böttcher P., Schnering H. G. The crystal structure of Tl_5Te_3 and its relationship to the Cr_5B_3. *Zeitschrift für Kristallographie*. 1989;188(3-4): 287–298. DOI: https://doi.org/10.1524/zkri.1989.188.3-4.287

9. Böttcher P., Doert Th., Druska Ch., Brandmöller S. Investigation on compounds with Cr_5B_3 and In_5Bi_3 structure types. *Journal of Alloys and Compounds*. 1997;246(1-2): 209–215. DOI: https://doi.org/10.1016/S0925-8388(96)02455-3

10. Imamalieva S. Z., Sadygov F. M., Babanly M. B. New thallium neodymium tellurides. *Inorganic Materials*. 2008;44(9): 935–938. DOI: https://doi.org/10.1134/s0020168508090070

11. Babanly M. B., Imamalieva S. Z., Babanly D. M., Sadygov F. M. Tl_9LnTe_6 (Ln-Ce, Sm, Gd) novel structural Tl_5Te_3 analogues. *Azerbaijan Chemical Journal*. 2009(1): 122–125. (In Russ., abstract in Eng.)

12. Imamaliyeva S. Z., Tl_4GdTe_3 and Tl_4DyTe_3 – novel structural Tl_5Te_3 analogues. *Physics and Chemistry of Solid State*. 2020;21(3): 492–495. DOI: https://doi.org/10.15330/pcss.21.3.492-495

13. Wacker K. Die kristalstrukturen von Tl_9SbSe_6 und Tl_9SbTe_6. *Z. Kristallogr. Supple*. 1991;3: 281.

14. Doert T., Böttcher P. Crystal structure of bismuthnonathalliumhexatelluride $BiTl_9Te_6$. *Zeitschrift*

für Kristallographie - Crystalline Materials. 1994;209(1): 95. DOI: https://doi.org/10.1524/zkri.1994.209.1.95

15. Bradtmöller S., Böttcher P. Darstellung und kristallostructur von $SnTl_4Te_3$ und $PbTl_4Te_3$. *Zeitschrift for anorganische und allgemeine Chemie*. 1993;619(7): 1155–1160. DOI: https://doi.org/10.1002/zaac.19936190702

16. Voroshilov Yu. V., Gurzan M. I., Kish Z. Z., Lada L. V. Fazovye ravnovesiya v sisteme Tl-Pb-Te i kristallicheskaya struktura soedinenii tipa $Tl_4B^{IV}X_3$ i $Tl_9B^VX_6$ [Phase equilibria in the Tl-Pb-Te system and the crystal structure of $Tl_4B^{IV}X_3$ and $Tl_9B^VX_6$ compounds]. *Izvestiya Akademii nauk SSSR. Neorganicheskie materialy*. 1988;24: 1479–1484. (In Russ.)

17. Bradtmöller S., Böttcher P. Crystal structure of copper tetrathallium tritelluride, $CuTl_4Te_3$. $CuTl_4Te_3$. *Zeitschrift für Kristallographie - Crystalline Materials*. 1994;209(1): 97. DOI: https://doi.org/10.1524/zkri.1994.209.1.97

18. Bradtmöller S., Böttcher P. Crystal structure of molybdenum tetrathallium tritelluride, $MoTl_4Te_3$. *Zeitschrift für Kristallographie – Crystalline Materials*. 1994;209(1): 75. DOI: https://doi.org/10.1524/zkri.1994.209.1.75

19. Babanly M. B., Imamalieva S. Z., Sadygov F. M. New thallium tellurides with indium and aurum. *Chemical Problems (Kimya Problemləri)*. 2009; 171–174. (In Russ., abstract in Eng.)

20. Guo Q., Chan M., Kuropatwa B. A., Kleinke H. Enhanced thermoelectric properties of variants of Tl_9SbTe_6 and Tl_9BiTe_6. *Chemistry of Materials*. 2013;25(20): 4097–4104. DOI: https://doi.org/10.1021/cm402593f

21. Guo Q., Assoud A., Kleinke H. Improved bulk materials with thermoelectric figure-of-merit greater than 1: $Tl_{10-x}Sn_xTe_6$ and $Tl_{10-x}Pb_xTe_6$. *Advanced Energy Materials*. 2014;4(14): 1400348-8. DOI: https://doi.org/10.1002/aenm.201400348

22. Bangarigadu-Sanasy S., Sankar C. R., Schlender P., Kleinke H. Thermoelectric properties of $Tl_{10-x}Ln_xTe_6$, with Ln = Ce, Pr, Nd, Sm, Gd, Tb, Dy, Ho and Er, and $0.25<x<1.32$. *Journal of Alloys and Compounds*. 2013;549: 126–134. DOI: https://doi.org/10.1016/j.jallcom.2012.09.023

23. Shi Y., Sturm C., Kleinke H. Chalcogenides as thermoelectric materials. *Journal of Solid State Chemistry*. 2019; 270: 273–279. DOI: https://doi.org/10.1016/j.jssc.2018.10.049

24. Piasecki M., Brik M. G., Barchiy I. E., Ozga K., Kityk I. V., El-Naggar A. M., Albassam A. A., Malakhovskaya T. A., Lakshminarayana G. Band structure, electronic and optical features of Tl_4SnX_3 (X= S, Te) ternary compounds for optoelectronic applications. *Journal of Alloys and Compounds*. 2017;710: 600–607. DOI: https://doi.org/10.1016/j.jallcom.2017.03.280

25. Reshak A. H., Alahmed Z. A., Barchij I. E., Sabov M. Yu., Plucinski K. J., Kityk I. V., Fedorchuk A. O. The influence of replacing Se by Te on electronic structure and optical properties of Tl_4PbX_3 (X = Se or Te): experimental and theoretical investigations. *RSC Advances*. 2015;5(124): 102173–102181. DOI: https://doi.org/10.1039/C5RA20956K

26. Malakhovskay-Rosokha T. A., Filep M. J., Sabov M. Y., Barchiy I. E., Fedorchuk A. O. Plucinski K. J. IR operation by third harmonic generation of Tl_4PbTe_3 and Tl_4SnS_3 single crystals. *Journal of Materials Science: Materials in Electronics*. 2013;24(7): 2410–2413. DOI: https://doi.org/10.1007/s10854-013-1110-9

27. Isaeva A., Schoenemann R., Doert T. Syntheses, crystal structure and magnetic properties of Tl_9RETe_6 (RE = Ce, Sm, Gd). *Crystals*. 2020;10(4): 277–11. DOI: https://doi.org/10.3390/cryst10040277

28. Bangarigadu-Sanasy S., Sankar C. R., Dube P. A., Greedan J. E., Kleinke H. Magnetic properties of Tl_9LnTe_6, Ln = Ce, Pr, Tb and Sm. *Journal of Alloys and Compounds*. 2014;589: 389–392. DOI: https://doi.org/10.1016/j.jallcom.2013.11.229

29. Arpino K. E., Wasser B. D., and McQueen T. M. Superconducting dome and crossover to an insulating state in $[Tl_4]Tl_{1-x}Sn_xTe_3$. *APL Materials*. 2015;3(4): 041507. DOI: https://doi.org/10.1063/1.4913392

30. Arpino K. E., Wallace D. C., Nie Y. F., Birol T., King P. D. C., Chatterjee S., Uchida M., Koohpayeh S. M., Wen J.-J., Page K., Fennie C. J., Shen K. M., McQueen T. M. Evidence for topologically protected surface states and a superconducting phase in $[Tl_4](Tl_{1-x}Sn_x)Te_3$ using photoemission, specific heat, and magnetization measurements, and density functional theory. *Physical Review Letters*. 2014;112(1): 017002-5. DOI: https://doi.org/10.1103/physrevlett.112.017002

31. Niu C., Dai Y., Huang B. et al. Natural three-dimensional topological insulators in Tl_4PbTe_3 and Tl_4SnTe_3. *Frühjahrstagung der Deutschen Physikalischen Gesellschaft*. Dresden, Germany, 30 Mar 2014 – 4 Apr 2014.

32. Imamalieva S. Z. Phase diagrams in the development of thallium-REE tellurides with Tl_5Te_3 structure and multicomponent phases based on them. Overview. *Kondensirovannye sredy i mezhfaznye granitsy = Condensed Matter and Interphases*. 2018;20(3): 332–347. DOI: https://doi.org/10.17308/kcmf.2018.20/570

33. Jia Y.Q. Crystal radii and effective ionic radii of the rare earth ions. *Journal of Solid State Chemistry*. 1991;95(1): 184-187. DOI: https://doi.org/10.1016/0022-4596(91)90388-X

Information about the author

Samira Zakir Imamaliyeva, PhD in Chemistry, Associate Professor, Institute of Catalysis and Inorganic Chemistry of the Azerbaijan National Academy of Sciences, Baku, Azerbaijan; e-mail: samira9597a@gmail.com. ORCID iD: https://orcid.org/0000-0001-8193-2122.

The author has read and approved the final manuscript.

Translated by Valentina Mittova
Edited and proofread by Simon Cox

Condensed Matter and Interphases
(Kondensirovannye sredy i mezhfaznye granitsy)

Original articles

DOI: https://doi.org/10.17308/kcmf.2020.22/3076
Received 29 September 2020
Accepted 15 November 2020
Published online: 25 December 2020

ISSN 1606-867X
eISSN 2687-0711

Synthesis and Physicochemical Properties of $Mn_xFe_{3-x}O_4$ Solid Solutions

© 2020 A. S. Korsakova[a], D. A. Kotsikau[b], Yu. S. Haiduk[b]✉, V. V. Pankov[b]

[a]*Research Institute for Physical Chemical Problems of the Belarusian State University, 14 Leningradskaya str., Minsk 220006, Belarus*

[b]*Belarusian State University, 4 Nezavisimosty prosp., Minsk 220030, Belarus*

Abstract

Ferrimagnetic nanoparticles are used in biotechnology (as drug carriers, biosensors, elements of diagnostic sets, contrast agents for magnetic resonance imaging), catalysis, electronics, and for the production of magnetic fluids and magnetorheological suspensions, etc. The use of magnetic nanoparticles requires enhanced magnetic characteristics, in particular, high saturation magnetisation.

The aim of our study was to obtain single-phased magnetic nanoparticles of $Mn_xFe_{3-x}O_4$ solid solutions at room temperature. We also studied the dependence of the changes in their structure, morphology, and magnetic properties on the degree of substitution in order to determine the range of the compounds with the highest magnetisation value.

A number of powders of Mn-substituted magnetite $Mn_xFe_{3-x}O_4$ (x = 0 – 1.8) were synthesized by means of co-precipitation from aqueous solutions of salts. The structural and micro-structural features and magnetic properties of the powders were studied using magnetic analysis, X-ray diffraction, transmission electron microscopy, and IR spectroscopy.

The X-ray phase analysis and IR spectroscopy confirm the formation of single-phase compounds with cubic spinel structures. The maximum increase in saturation magnetization as compared to non-substituted magnetite was observed for $Mn_{0.3}Fe_{2.7}O_4$ (M_s = 68 A·m^2·kg^{-1} at 300 K and M_s = 85 A·m^2·kg^{-1} at 5 K). This is associated with the changes in the cation distribution between the tetrahedral and octahedral cites.

A method to control the magnetic properties of magnetite by the partial replacement of iron ions in the magnetite structure with manganese has been proposed in the paper. The study demonstrated that it is possible to change the magnetisation and coercivity of powders by changing the degree of substitution. The maximum magnetisation corresponds to the powder $Mn_{0.3}Fe_{2.7}O_4$. The nanoparticles obtained by the proposed method have a comparatively high specific magnetisation and a uniform size distribution. Therefore the developed materials can be used for the production of magnetorheological fluids and creation of magnetically controlled capsules for targeted drug delivery and disease diagnostics in biology and medicine (magnetic resonance imaging).

Keywords: solid solution, magnetic nanoparticles, spinel, specific magnetization.

For citation: Korsakova A. S., Kotsikau D. A., Haiduk Yu. S., Pankov V. V. Synthesis and physicochemical properties of $Mn_xFe_{3-x}O_4$solid solutions. *Kondensirovannye sredy i mezhfaznye granitsy = Condensed Matter and Interphases*. 2020;22(4): 466–472. DOI: https://doi.org/10.17308/kcmf.2020.22/3076

Для цитирования: Корсакова А. С., Котиков Д. А., Гайдук Ю. С., Паньков В. В. Синтез и физико-химические свойства твердых растворов $Mn_xFe_{3-x}O_4$. *Конденсированные среды и межфазные границы*. 2020;22(4): 466–472. DOI: https://doi.org/10.17308/kcmf.2020.22/3076

✉ Yulyan S. Haiduk, e-mail: j_hajduk@bk.ru (corresponding author)

1. Introduction

The synthesis of nanomaterials has been the focus of many studies lately. Of particular interest are magnetite (Fe_3O_4) and maghemite (γ-Fe_2O_3) magnetic nanoparticles (MNP) [1]. They are used in biotechnology (as drug carriers, biosensors, elements of diagnostic sets, and contrast agents for magnetic resonance imaging), catalysis, electronics, production of magnetic fluids and magnetorheological suspensions, etc. [2, 3]. The magnetic properties of nanoobjects are known to be weaker than those of bulk materials. Thus, their application requires high magnetic characteristics, in particular high saturation magnetisation values. In this regard, magnetite was chosen as one of the best candidates. Moreover, the magnetisation of magnetite may increase due to its ferrous ions being substituted by some transition metals ions. For instance, the magnetic moment of bivalent manganese ions is 5 μB. So, when they replace the magnetite ferrous ions, the magnetic moment of the solid solution may be increased.

At present, there are various methods to obtain oxide nanoparticles [1, 4–9]. The simplest and the most convenient method is the co-precipitation method. It is a well-stidied approach thatallows carrying on the synthesis without heating or using an inert atmosphere. Due to its high sensitivity to various parameters (type of the precipitant, the concentrations of the reagents, pH of the reaction medium, etc.) the method can be used to obtain nanoparticles of various size and properties [1]. It is also quite simple, inexpensive, and practical, and therefore is of great use for large-scale production.

The aim of our study was to obtain single-phased magnetic nanoparticles of $Mn_xFe_{3-x}O_4$ solid solutions at room temperature. We also studied the dependence of the changes in their structure, morphology, and magnetic properties on the degree of substitution in order to determine the compounds with the highest magnetisation values.

2. Experimental

$Mn_xFe_{3-x}O_4$ solid solutions (x = 0; 0.3; 0.6; 0.8; 1.0; 1.2; 1.4; 1.8) were synthesised at room temperature by combined hydrolysis of aqueous solutions of inorganic salts of the corresponding metals. The starting materials ($MnCl_2{\cdot}4H_2O$, $Fe(NO_3)_3{\cdot}9H_2O$, and $FeSO_4{\cdot}7H_2O$) were taken in the stoichiometric proportions (Fe^{3+}: Fe^{2+} = 2: 1 mol.). For some samples, the stoichiometric proportions of the cations Fe^{3+} and Fe^{2+} were altered by 5 % compared to the total number of Fe^{3+} and Fe^{2+}cations. The precipitant was chosen to be NaOH. The amount of the precipitant was 10% larger than the stoichiometric amount. The excess amount of the precipitant was selected specifically so that after mixing the solutions the pH of the reaction mixture was ~ 11. The sample with x = 0.3, which had the highest specific saturation magnetisation, was subjected to thermal treatment in air for 2 h at 300 °C followed by vibromilling (30 min). This was done in order to use the sample to produce a magnetorheological suspension.

The XRD spectra of the powders were registered using a DRON 3.0 diffractometer ($Co_{K\alpha}$-radiation, 1.78897 Å) within angle range of 2θ = 6–80°. The phase composition of the substance was determined by comparing the characteristics of each peak (their diffraction angles and intensity) with the reference values for magnetites Fe_3O_4 (JCPDS 88–0315, a = 8.3752 Å) and $MnFe_2O_4$ (JCPDS 74–2403, a = 8.511 Å). Scherrer's equation was used to calculate the average size of the particles based on the XRD patterns.

The microstructure of the samples was studied using transmission electron microscopes LEO 1420 and HitachiH-800 with an accelerating voltage of 200 keV.

The IR spectra of the samples were registered using an AVATAR 330 (Thermo Nicolet) spectrometer in the region ν = 4000–400 cm^{-1}. The spectra were registered by means of diffuse reflection using a Smart Diffuse Reflectance accessory.

The magnetic characteristics were studied using a Cryogen Free Measurement System from Cryogenic Ltd, where hysteresis loops were recorded at 5 and 300 K, and B_{max} = 8 T.

3. Results and discussion

The spinel structure of a magnetite doped with manganese can be either cubic or tetragonal depending on the degree of substitution. Non-substituted magnetite (x = 0) has a cubic structure, while Mn_3O_4 has a tetragonal lattice [10].

During the transformation from Fe_3O_4 to Mn_3O_4 the degree of inversion of the crystal structure alters, with the magnetite being an inverse spinel and Mn_3O_4 being a normal spinel [7]. This transformation is caused by a different distribution of cations between the sites as suggested in [11]. For $Mn_xFe_{3-x}O_4$, the cation distribution can be generally presented as follows:

$$\left(Mn^{2+}_{x-i}\,Fe^{3+}_{\gamma}\right)_A\left[Mn^{2+}_{i}\,Fe^{2+}_{\gamma-x}\,Fe^{3+}_{2-\gamma}\right]_B O_4, \qquad (1)$$

where x is the degree of substitution in $Mn_xFe_{3-x}O_4$ solid solution (the total number of Mn^{2+}ions); i is the ratio of Mn^{2+} ions in the octahedral sites; and γ is the degree of inversion of the crystal lattice.

It is known that for the stoichiometric manganese ferrite $MnFe_2O_4$ $\gamma = 0.2$, with 80 % of Mn^{2+} ions occupying tetrahedral positions [11].

The XRD patterns of $Mn_xFe_{3x}O_4$ solid solution powders presented in Fig. 1 are similar and have broad peaks. All the synthesised $Mn_xFe_{3-x}O_4$ compounds have a cubic spinel structure, which is characteristic of pure magnetite. The presence of the broad diffraction reflections may result from the low degree of crystallinity of the structure. $Mn_xFe_{3-x}O_4$ with $x > 1.0$ was synthesised using a different method (the stoichiometric proportions of the cations Fe^{3+} and Fe^{2+} were altered by 5 %) to prevent the formation of the α-Fe_2O_3 phase in the samples with high concentrations of manganese ($x > 1.0$)

Despite the low intensity of the peaks, the X-ray diffraction pattern of the sample with x = 1.8 showed a peak at $2\theta = 41.2$, which was assumed to correspond to the diffraction reflection of the spinel with the maximum intensity index (311). The X-ray amorphous state of this compound may indicate a significant deformation of the crystal lattice of the spinel caused by a large number of manganese ions [12]. In other words, it may indicate a gradual structural transformation of the cubic spinel. This study demonstrated that an increase in the degree of substitution is predictably followed by an increase both in unit cell parameters and in its volume. The ionic radius of Mn^{2+} is larger than the one typical of Fe^{2+} and Fe^{3+} regardless of the coordination environment. Therefore, the introduction of manganese ions into the crystal lattice inevitably

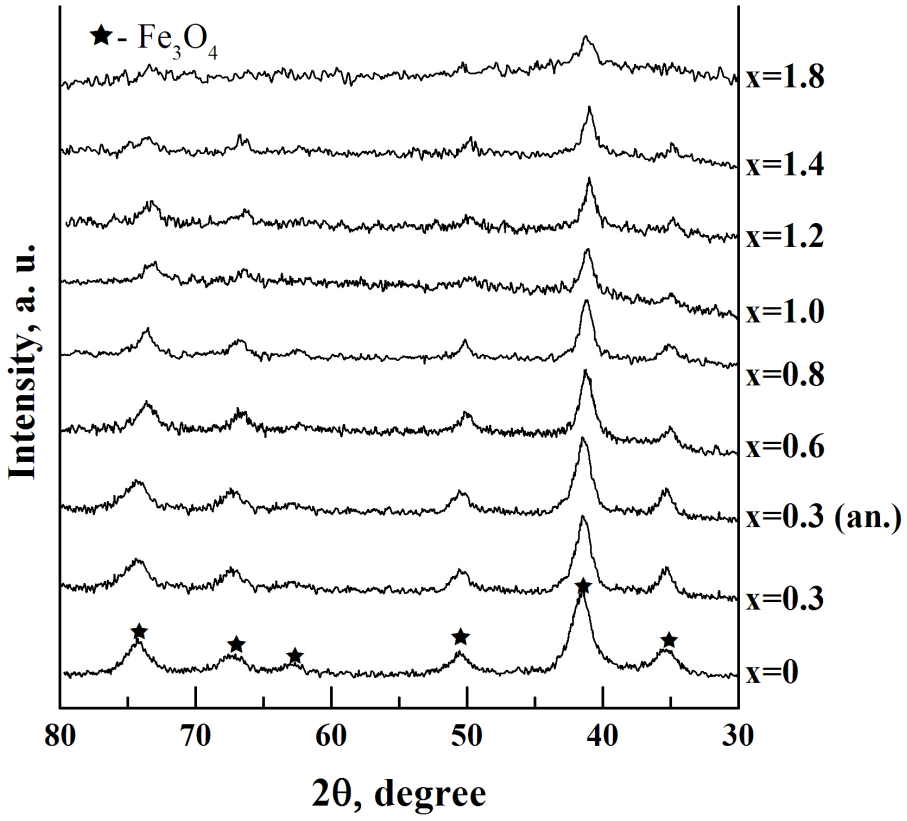

Fig. 1. XRD spectra of $Mn_xFe_{3-x}O_4$ powders ($0 < x < 1.8$)

results in an increase in the unit cell parameters and volume. For the same reason, the peaks with the corresponding Miller indices shift toward the region of narrow angles, when the concentration of manganese in the sample increases.

The calculated lattice constants of the powders with higher concentrations of manganese are smaller than those described in the available literature. The difference can be accounted for by the fact that during the growth of the nanoparticles in alkaline medium and in the presence of atmospheric oxygen, the ageing of the Fe_3O_4 magnetite to γ-Fe_2O_3 maghemite with smaller lattice constant (JCPDS 39–1346, a = 8.3515 Å) proceeds smoothly [13, 14].

The average size of the crystallites increases nonlinearly with an increase in the degree of substitution. The difference in the size may indicate a difference in the speed of $Mn(OH)_2$ and $Fe(OH)_2$ hydrolysis as well as strong competition between them during the formation of nanoparticles of various compositions.

The dislocation densities and the number of micro-stress sites in solid solutions decrease nonlinearly and in a similar way. Micro-stress plays a key role in the development of crystals. They prevent the growth of crystals and thus determine the size if the formed particles [15]. The comparison of the curves showing the alterations in the particle size and micro-stress demonstrates that they are mirror reflections of each other.

Fig. 2 presents TEM microphotographs of some of the samples obtained by the co-precipitation. In each case, nearly spherical nanoparticles were formed. The average size particles of $Mn_{0.3}Fe_{2.7}O_4$ was 9 nm, $Mn_{0.8}Fe_{2.2}O_4$– 11 nm, and $MnFe_2O_4$– 15 nm. The obtained results comply with the average crystallite size calculated using the X-ray diffraction patterns of the corresponding samples. The diameter of the nanoparticles increases with the growth of the concentration of manganese in the $Mn_xFe_{3-x}O_4$ solid solution. For the sample annealed at 300 °C (Fig. 2c), we observed the obvious faceting of the nanoparticles accompanied by an increase in the crystallinity, while the size of the nanoparticles was similar to that of the nanoparticles that had not been annealed.

For the spinel structures, the characteristic IR spectra lines indicating the presence of structural changes correspond to the vibrations of M–O and M–O–H bonds. The ion environment of Fe^{3+} was altered by introducing divalent ions with large radii into the magnetite crystal lattice. This resulted in the distortion of the symmetry of the coordination environment of Fe^{3+} or changes in the force constant of the Fe–O bond. Therefore, the IR spectra (Fig. 3) demonstrate the splitting or distortion of the lines of characteristic vibrations of the Fe–O bond. When manganese and iron ions are evenly distributed within the crystal lattice of the spinel, one can usually observe the shift of the absorption peaks of characteristic vibrations only. The additional peaks indicate the presence of a different phase.

The results of the IR spectroscopy presented in Fig. 3 confirm the formation of the spinel structure for all the compounds.

The characteristic frequencies ν_1 (≈ 560 cm^{-1}) and ν_2 (≈ 430 cm^{-1}) corresponding to the stretching vibrations of Me–O in tetrahedral and octahedral

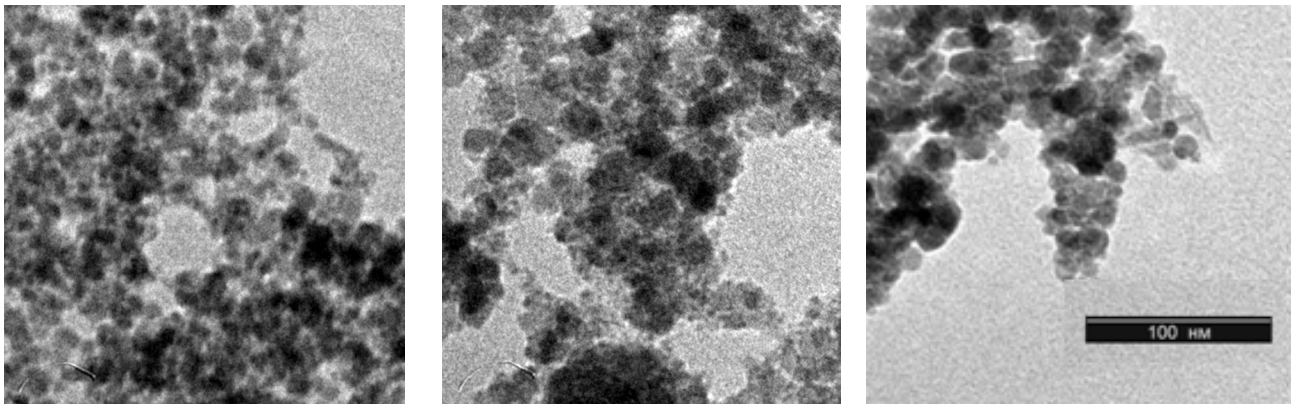

a *b* *c*

Fig. 2. TEM images of the $Mn_xFe_{3-x}O_4$ powder: a) x = 0.3; b) x = 1.0; c) x = 0.3 (annealed at 300 °C, 2 h)

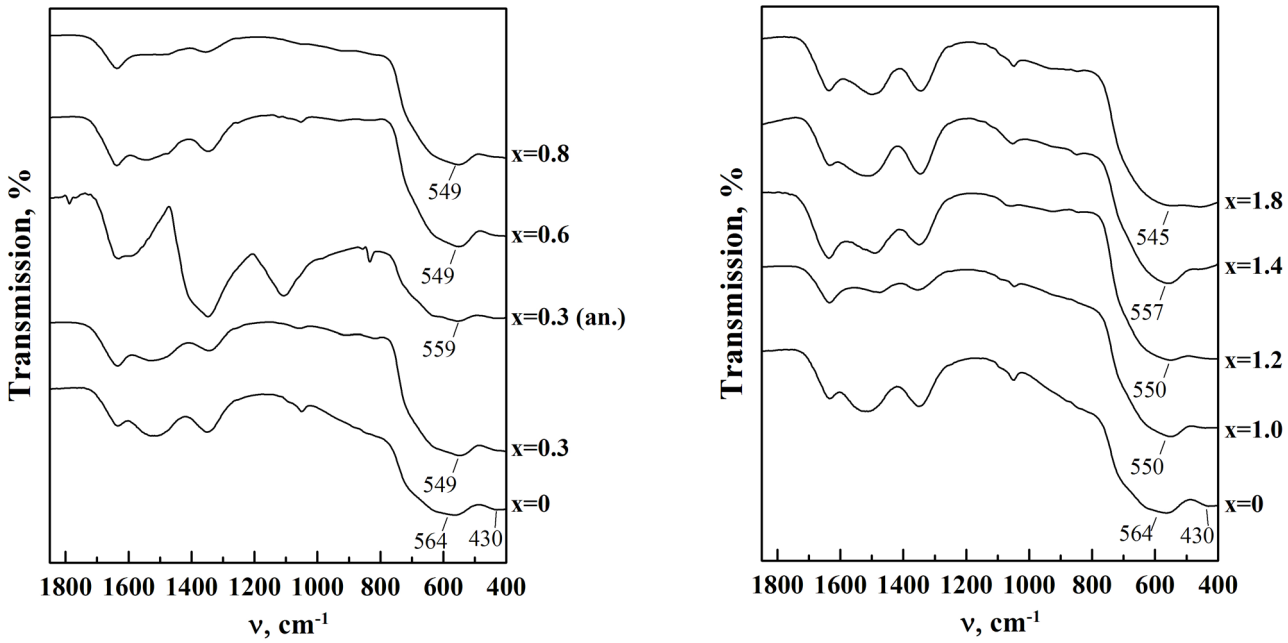

Fig. 3. Fragments of IR spectra of $Mn_xFe_{3-x}O_4$ solid solutions ($0 < x < 1.8$), (an.) – the powder after annealing at 300 °C for 2 h

sites shift towards lower frequencies after the introduction of Mn^{2+}cations. This is caused by the presence of combined vibrational bands of the Fe–O bonds in octahedral positions with Mn^{2+} ions in the immediate coordination environment Fe–O–Mn. This results in the increase in the length of the bond ($l_{Mn\text{-}O} > l_{Fe\text{-}O}$) and alters the force constant.

For samples with a high manganese content ($x > 1.2$), as well as for a sample with $x = 0.3$ (an.), a low-intensity band at 848.57 cm^{-1} was found, characteristic of the individual oxide α-Fe_2O_3. X-ray diffraction analysis did not reveal this phase in the samples.

The magnetic properties of the $Mn_xFe_{3-x}O_4$ nanoparticles were analysed using the experimental data on their specific magnetisation and coercivity in the temperature range of 5–300 K. The magnetisation and demagnetisation curves were similar at room temperature, which proves the absence of hysteresis and coercive force, and indicates a superparamagnetic state of the nanoparti-

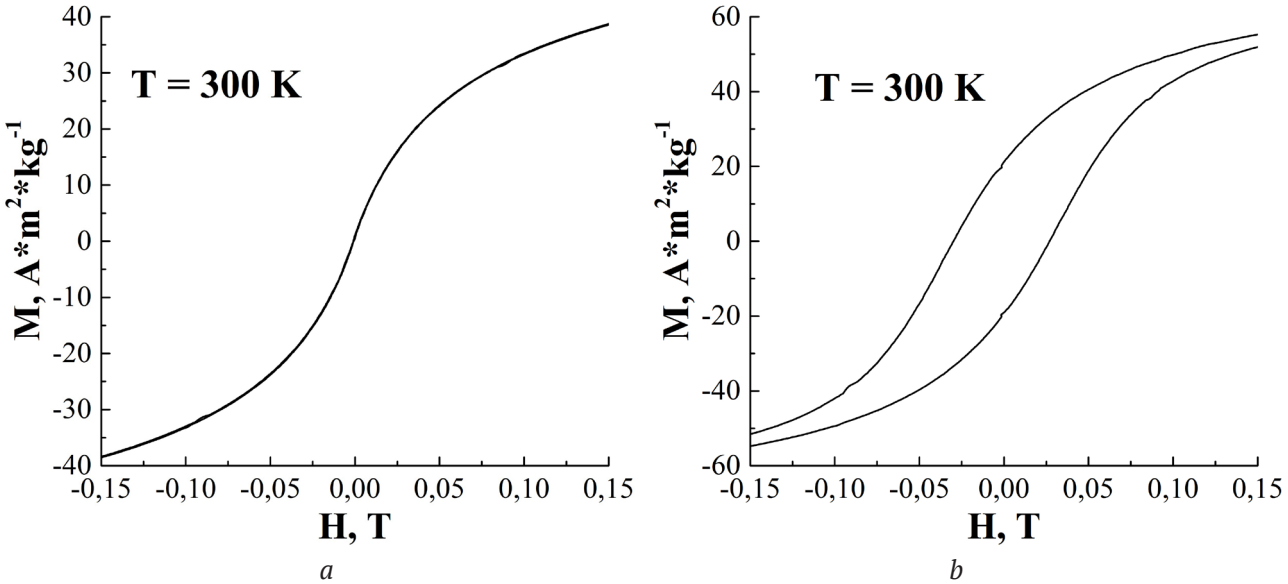

Fig. 4. Curves of specific saturation magnetisation for the $Mn_{0.3}Fe_{2.7}O_4$ sample at 300 K and the $Mn_{0.3}Fe_{2.7}O_4$ sample (annealed at 300 °C, 2 h) at 300 K

cles (Fig. 4a). At the same time, $Mn_{0.3}Fe_{2.7}O_4$ sample annealed at 300 °C for 2 hours had a coercivitye of ~ 120 Oe (Fig. 4b). Therefore, thermal treatment results in further crystallisation and an increase in the anisotropy constant.

The magnetic properties of the $Mn_xFe_{3-x}O_4$ solid solutions depend directly on the distribution of cations within the spinel structure [7]. The distribution is of combined nature, i.e. manganese ions occupy both tetrahedral and octahedral sites of the crystal lattice. Thus, for the manganese ferrite the distribution is $(Mn_{0.8}Fe_{0.2})$ $[Mn_{0.2}Fe_{1.8}]O_4$.

The saturation magnetisation changes nonlinearly with an increase in the concentration of manganese in $Mn_xFe_{3-x}O_4$. The magnetisation grows at first following the increase in the portion of manganese in the solid solution. It reaches its maximum for $Mn_{0.3}Fe_{2.7}O_4$ compound and then decreases (Fig. 5).

The dependence occurs because the magnetic moment of the Mn^{2+} ion (5 μB) with five unpaired electrons is higher than that of the Fe^{2+} ion (4 μB). Therefore, when Fe^{2+} ions are replaced with Mn^{2+} ions in the octahedral sub-lattice, the magnetisation should grow. The saturation magnetisation is mainly determined by the superexchange interaction between the ions of A and B sub-lattices, which can be described using the formula

$$\mu_{theor} = \mu_B - \mu_A, \quad (2)$$

where μ_A and μ_B are the magnetic moments of the cations of A and B voids respectively.

If the number of manganese ions in $Mn_xFe_{3-x}O_4$ increases further, the ions being oxidised to Mn^{3+} actively begin to occupy the B voids of the crystal lattice. Since Fe^{3+} = (5 μB) and Mn^{3+} = (4 μB), the super-exchange interaction between the ions in sub-lattices A and B decreases, which in turn leads to a decrease in the saturation magnetisation of $Mn_xFe_{3-x}O_4$.

4. Conclusions

The study allowed us to determine the conditions for the synthesis of single-phase magnetite nanoparticles doped with manganese at room temperature and under atmospheric pressure. The concentrations at which solid solutions of iron and manganese oxides have the structure of a cubic spinel lie within the range

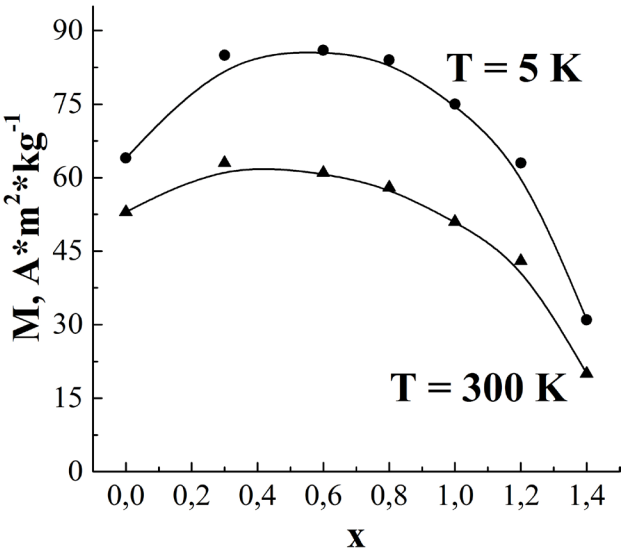

Fig. 5. Specific magnetisation of $Mn_xFe_{3-x}O_4$ solid solutions depending on the compound

$0 < x < 1.8$.

The alteration in the saturation magnetisation caused by an increase in the concentration of manganese oxide in the solid solution is nonlinear. The maximum saturation magnetisation (68 А·м²·kg⁻¹ at 300 K and 85 А·м²·kg⁻¹ at 5 K) was observed in $Mn_{0.3}Fe_{2.7}O_4$. The smallest nanoparticles (9 nm) are observed in $Mn_{0.3}Fe_{2.7}O_4$.

The synthesised nanoparticles can be used as contrast agents for MRI diagnostics and as components of magnetorheological fluids, as well as to obtain magnetorheological fluids and produce magnetically controlled capsules for targeted drug delivery.

Conflict of interest

The authors declare that they have no known competing financial interests or personal relationships that could have influenced the work reported in this paper.

References

1. Gubin C. G., Koksharov Yu. A., Khomutov G. B., Yurkov G. Yu. Magnetic nanoparticles: preparation, structure and properties. *Russian Chemical Reviews* 2005;74(6): 539–574. Available at: https://www.elibrary.ru/item.asp?id=9085819

2. Skumryev V., Stoyanov S., Zhang Y., Hadjipanayis G., Givord D., Nogués J. Beating the superparamagnetic limit with exchange bias. *Nature.* 2003;423(6943): 850–853. DOI: https://doi.org/10.1038/nature01687

3. Joseph A., Mathew S. Ferrofluids: synthetic strategies, stabilization, physicochemical features,

characterization, and applications. *ChemPlusChem*. 2014;79(10): 1382–1420. DOI: https://doi.org/10.1002/cplu.201402202

4. Mathew D. S., Juang R.-S. An overview of the structure and magnetism of spinel ferrite nanoparticles and their synthesis in microemulsions. *Chemical Engineering Journal*. 2007:129(1–3): 51–65. DOI: https://doi.org/10.1016/j.cej.2006.11.001

5. Rewatkar K. G. Magnetic nanoparticles: synthesis and properties. *Solid State Phenomena*. 2016:241: 177–201. DOI: https://doi.org/10.4028/www.scientific.net/ssp.241.177

6. Tartaj P., Morales M. P., Veintemillas-Verdaguer S., Gonzalez-Carre´no T., Serna C. J. The preparation of magnetic nanoparticles for applications in biomedicine. *Journal of Physics D: Applied Physics*. 2003:36(13): 182–197. DOI: https://doi.org/10.1088/0022-3727/36/13/202

7. West A. *Khimiya tverdogo tela. Teoriya i prilozheniya [Solid State Chemistry and Its Applications]*. In 2 parts Part 1. Transl. from English. Moscow, Mir, 1988 558 p.

8. *Spravochnik khimika: V 6 t. 2-e izd. Obshchiye svedeniya. Stroyeniye veshchestva. Svoystva vazhneyshikh veshchestv. Laboratornaya tekhnika* [Chemist's Handbook: In 6 volumes, 2nd ed. General information. The structure of matter. Properties of the most important substances. Laboratory equipment]. B. P. Nikolskiy (ed.) Moscow – Leningrad: Goskhimizdat Publ.; 1963. V. 1. 1071 p. (In Russ.)

9. Zhuravlev G. I. *Khimiya i tekhnologiya ferritov* [Ferrite chemistry and technology]. Leningrad: Khimiya Publ.; 1970. p. 192. (In Russ.)

10. Mason B. Mineralogical aspects of the system FeO-Fe_2O_3-MnO-Mn_2O_3. *Geologiska Föreningen i Stockholm Förhandlingar*. 1943;65(2): 97–180. DOI: https://doi.org/10.1080/11035894309447142

11. Guillemet-Fritsch S., Navrotsky A., Tailhades Ph., Coradin H., Wang M. Thermochemistry of iron manganese oxide spinels. *Journal of Solid State Chemistry*. 2005;178(1):106–113. DOI: https://doi.org/10.1016/j.jssc.2004.10.031

12. Ortega D. Structure and magnetism in magnetic nanoparticles. In: *Magnetic Nanoparticles: From Fabrication to Clinical Applications*. Boca Raton: CRC Press; 2012. p. 3–72. DOI: https://doi.org/10.1201/b11760-3

13. Kodama T., Ookubo M., Miura S., Kitayama Y. Synthesis and characterization of ultrafine Mn(II)-bearing ferrite of type $Mn_xFe_{3-x}O_4$ by coprecipitation. *Materials Research Bulletin*... 1996:31(12): 1501–1512. DOI: https://doi.org/10.1016/s0025-5408(96)00146-8

14. Al-Rashdi K. S., Widatallah H., Al Ma'Mari F., Cespedes O., Elzain M., Al-Rawas A., Gismelseed A., Yousif A. Structural and mossbauer studies of nanocrystalline Mn^{2+} doped Fe_3O_4 particles. *Hyperfine Interact*. 2018:239(1): 1–11. DOI: https://doi.org/10.1007/s10751-017-1476-9

15. Modaresi N., Afzalzadeh R., Aslibeiki B., Kameli P. Competition between the Impact of cation distribution and crystallite size on properties of $Mn_xFe_{3-x}O_4$ nanoparticles synthesized at room temperature. *Ceramics International*. 2017:43(17): 15381–15391. DOI: https://doi.org/10.1016/j.ceramint.2017.08.079

Information about the authors

Alina S. Korsakova, intern, research fellow, Research Institute for Physical Chemical Problems of the Belarusian State University, Minsk, Republic of Belarus; e-mail: korsakova@bsu.by. ORCID iD: https://orcid.org/0000-0001-8898-4726.

Dzmitry A. Kotsikau, PhD in Chemistry, Associate Professor, Belarusian State University, Minsk, Republic of Belarus; e-mail: kotsikau@bsu.by. ORCID iD: https://orcid.org/0000-0002-3318-7620.

Yulyan S. Haiduk, research fellow, Belarusian State University, Minsk, Republic of Belarus; e-mail: j_hajduk@bk.ru. ORCID iD: https://orcid.org/0000-0003-2737-0434.

Vladimir V. Pankov, DSc in Chemistry, Professor, Head of the Department of Physical Chemistry, Belarusian State University, Minsk, Republic of Belarus; e-mail: pankov@bsu.by. ORCID iD: https://orcid.org/0000-0001-5478-0194.

All authors have read and approved the final manuscript.

Translated by Yulia Dymant
Edited and proofread by Simon Cox

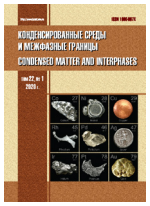

Condensed Matter and Interphases
(Kondensirovannye sredy i mezhfaznye granitsy)

Original articles

DOI: https://doi.org/10.17308/kcmf.2020.22/3059
Received 23 September 2020
Accepted 08 October 2020
Published online 25 December 2020

ISSN 1606-867X
eISSN 2687-0711

Development of Ideas About the Rheological Behaviour of Building Mixtures Taking into Account Fractal-Cluster Processes in Their Structure Formation

© 2020 A. A. Ledenev[a]✉, V. T. Pertsev[b], O. B. Rudakov[b]✉, D. E. Barabash[a]

[a]*Air Force Military Educational and Scientific Centre "Air Force Academy named after Professor N.E. Zhukovsky and Y.A. Gagarin" (Voronezh), 54a St. Bolshevikov ul.,Voronezh 394064, Russian Federation*

[b]*Voronezh State Technical University, 14 Moskovsky pr., Voronezh 394026, Russian Federation*

Abstract

Development of theoretical ideas about the mechanism of the rheological behaviour of building mixtures and the experimental assessment of their rheological properties is a relevant area of physiochemical research of materials. To assess the changes in rheological properties when varying the component composition of building mixtures, it is important to use quantitative indicators characterising the microstructure of the mixtures. Revealing the regularities of the formation of heterogeneous microstructures makes it possible to assess their correlation with the rheological properties of building mixtures at the macro level. The aim of the paper is to discuss the results of the implementation of methodological approaches, theoretical modelling, and experimental assessment of the quantitative indicators of the rheological properties of typical building mixtures.

The experimental research methodology is based on the assessment of the rheological properties of heterogeneous dispersed systems (HDS), taking into account fractal-cluster manifestations in their microheterogeneous component. The experiment was carried out using model HDS containing the components of building mixtures. Their rheological properties were determined by rotational viscometry with different compositions of HDS. The fractal dimension *D* was used for a quantitative assessment of the structural and rheological properties and identification of the patterns of their change depending on the composition of mixtures. The value was determined by mathematical modelling.

We analysed model concepts of the rheological behaviour of building mixtures. It was shown that the existing rheological models of an elastic-viscous-plastic medium did not give a complete description of the processes of formation and destruction of the microstructure of concentrated HDS (building mixtures). We carried out an experimental assessment of the effect of the properties of solid phase particles on the change in the structural and rheological characteristics of HDS, taking into account the fractal-cluster principles of their structure formation.

We specified the ideas about the mechanism of rheological behaviour of building mixtures. They take into consideration the processes of the formation and destruction of fractal-cluster formations in the microstructure of HDS. It was shown that the fractal dimension *D* can be one of the quantitative characteristics of the structural and rheological properties. We determined the correlation between the fractal dimension *D* and other experimental rheological characteristics: the ultimate shear stress and effective viscosity. The obtained results can be used to regulate rheological properties and optimise the technological processes for the manufacture of building materials and products.

Keywords: heterogeneous dispersed systems, rheological properties, building mixtures, modelling, fractal-cluster structures.

For citation: Ledenev A. A., Pertsev V. T., Rudakov O. B., Barabash D. E. Development of ideas about the rheological behaviour of building mixtures taking into account fractal-cluster processes in their structure formation. *Kondensirovannye sredy i mezhfaznye granitsy* = *Condensed Matter and Interphases*. 2020;22(4): 473–480. DOI: https://doi.org/10.17308/kcmf.2020.22/3059

✉ Andrey A. Ledenev, e-mail: ledenoff@mail.ru
✉ Oleg B. Rudakov, e-mail: robi57@mail.ru

Для цитирования: Леденев А. А., Перцев В. Т., Рудаков О. Б., Барабаш Д. Е. Развитие представлений о реологическом поведении строительных смесей с учетом фрактально-кластерных процессов при их структурообразовании. Конденсированные среды и межфазные границы. 2020;22(4): 473–480. DOI: https://doi.org/10.17308/kcmf.2020.22/3059

1. Introduction

When carrying out physiochemical studies of the structures of building materials, it is important to determine their rheological properties. Rheological properties affect the parameters of technological processes in the construction industry. For example, the rheological properties of mortar and concrete mixtures determine the conditions of the mixing, transportation, moulding, and compaction technologies. They ultimately affect the physical and technical characteristics of finished products and structures [1–21].

Currently, in the production of mortars and concretes, the range and component composition of raw materials with increased dispersity and concentration of solids is expanding. We have multicomponent compositions with fine ground mineral additives, surfactants, organomineral additives, nanosized particles, etc. [2–19]. Constructors apply highly mobile and self-sealing mixtures, whose rheological characteristics ensure preservation of the structure during transportation. At the same time, such mixtures remain highly fluid during the moulding process [2, 3, 9–11]. The mixtures under study are multicomponent, multiphase heterogeneous dispersed-granular systems. Due to the complexity of the study of their structure, we used empirical approaches based on varying the formulation and technology factors and assessing the change in rheological properties without taking into account internal forces and interphase interactions. To study the relationship between the structure and the properties, it is advantageous to implement a methodological approach based on modelling the structure as a multilevel hierarchical system. This approach makes it possible to describe the processes and phenomena that occur at various levels of scale and stages of the structure formation of concrete. During the early stage of coagulation structure formation, on the scale of colloidal and microheterogeneous particles, internal forces are manifested at the micro- and meso-levels of the structure of concrete mixtures (10^{-8}–10^{-3} m). In such a system, physiochemical processes of interparticle and interphase interaction are determinant at the interphase boundary and within the "dispersed phase - dispersion medium" phases. The fractal-cluster structures, self-similar at various scale levels, typically form as a result of the manifestation of molecular electrostatic and capillary-film forces [22].

The formation and destruction of aggregated fractal-cluster structures has a significant effect on the manifestation of intra- and interflow interactions, characterised by a change in rheological properties [22]. This predetermines the need for research and design aimed at developing the principles of the rheology of concentrated mixtures. For the systems under consideration, the manifestation of rheological properties depends on the dispersity of solid phase particles, the particle shape and surface roughness, the solids concentration, etc. Revealing the patterns of formation of fractal-cluster structures makes it possible to assess the interrelation between structural changes and the dispersion properties. In this case, a quantitative assessment of the structural and rheological properties plays an important role. It is important to take into account fractal-cluster manifestations and the dependence of their change on the properties of solid phase particles.

It is necessary to implement new scientific and practical approaches to analyse self-organising processes, which are difficult to observe directly. We believe that one such approach is the assessment of the rheological properties of building mixtures taking into account the characteristic fractal-cluster manifestations at the microheterogeneous level. The complex application of the theoretical provisions of the rheology of heterogeneous dispersed systems, fractal geometry, statistical physics, and mathematical modelling becomes an effective methodology to expand our knowledge regarding the processes of formation and destruction of the structure of building materials at the micro-level.

Thus, the aim of the work is to implement methodological approaches to modelling and experimental assessment of the rheological properties of multicomponent building mixtures using quantitative indicators that characterise the processes of structure formation, composition, and properties of mixture components. These

multicomponent mixtures are mineral pastes containing solid phase particles of various nature.

2. Experimental

As we know, classical models of the rheological behaviour of HDS, including multicomponent building mixtures, have been developed for homogeneous models of the continuum mechanics: the Kelvin, Bingham, and Newton models, etc. [23–25].

The rheological behaviour of the systems under consideration can be described by the following equation [1, 22–25]

$$\tau = \tau_0 + \eta \cdot \varepsilon^n, \quad (1)$$

where τ is the shear stress; τ_0 is the ultimate shear stress; η is the effective viscosity; ε^n is the shear velocity gradient; n is the pseudoplasticity index.

We applied experimental methods to model the rheological behaviour of building mixtures. They were based on the determination of the ultimate shear stress τ_0, the effective viscosity η, or a combination of these values [22, 26]. These integral indicators allow indirect assessments of the viscoelastic characteristics of building mixtures. However, they are not sufficient for a full understanding of how the structure of mixed materials is formed and destructed. When dispersions in the form of pastes, suspensions, foams, and gels are exposed to intense external factors, individual structural elements of mixtures, represented by particles and aggregates of the disperse phase of various concentrations and shapes, undergo changes due to reorientation, disaggregation, etc. (Fig. 1) [25].

For the experimental assessment of the rheological properties of mortar and concrete building mixtures is so complex with regards to the methodology due to the heterogeneity of their structures. This can be explained by the combination of coarsely dispersed components, fine and coarse aggregates, as well as microheterogeneous components: a binder and finely dispersed additives. The manifestation of rheological properties is largely associated with the formation of aggregated fractal-cluster systems in the microstructure of mixtures. For the systems under study, the existing theoretical provisions and models do not provide an exhaustive description of the processes of formation and destruction of the microstructure of concentrated watered dispersed systems and mixtures.

Based on the theoretical provisions [27], the model for the manifestation of the rheological properties of watered concentrated HDS is shown in Fig. 2. The model shows that for the values larger than τ_0, the formed structure of the dispersion in the form of a percolation fractal cluster breaks down into individual aggregates, which is accompanied by a decrease in the effective viscosity η (Fig. 2a, p. 1 – p. 2). P. 2 – p. 3 zone in Fig. 2a reflects the destruction of interaggregate bonds, the effective viscosity is minimal η_{min}. With an increase in stresses, the bonds break completely, with the formation of smaller clusters and individual particles. This leads to an increase in internal friction and an increase in viscosity (Fig. 2a, p. 3 – p. 4). A subsequent increase in stresses again leads to a decrease in viscosity because of the discontinuity within the system (Fig. 2a, p. 4 – p. 5). Due to the outlined features of the manifestation of properties in the microheterogeneous component, it is important to obtain a quantitative assessment of the structural and rheological characteristics of mixtures.

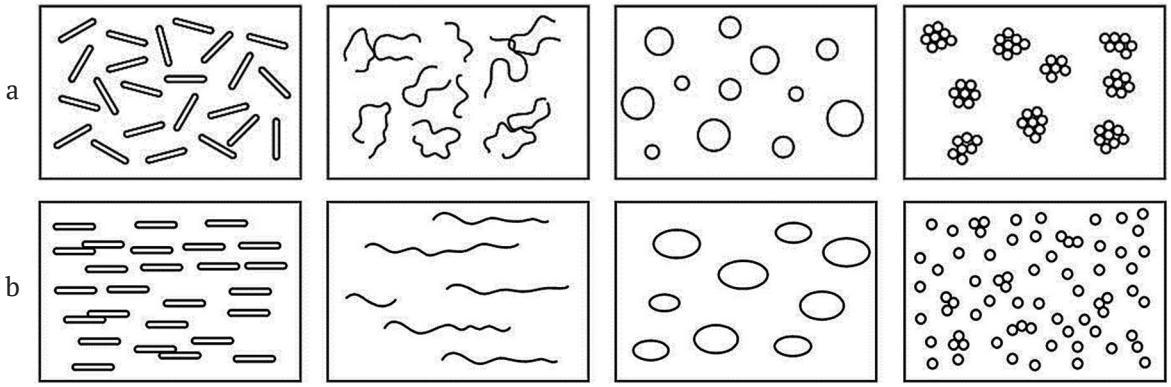

Fig. 1. Schemes of the structure models of dispersed systems without shear (a) and structural changes under shear stress (b)

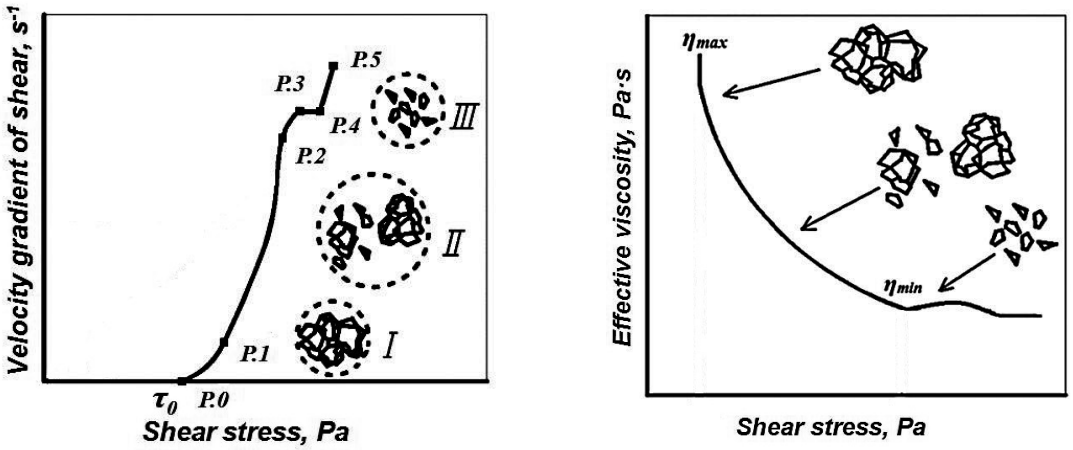

Fig. 2. Models of flow curves of dispersed systems in the form of dependence of the shear velocity gradient (a) and effective viscosity (b) on shear stress

The experiment was carried out on model HDS: mineral pastes containing solid phase particles of various natures, which are used in typical building mixtures. We studied the "cement – water", "sand – water", "limestone – water", and "ash – water" HDS. The dispersity of the solid phase particles was 300, 500, and 700 m^2/kg. Rheological properties were determined using rotational viscometry. We determined the correlations of the shear velocity gradient and effective viscosity with the shear stress by varying the composition of the model HDS.

For a quantitative assessment of structural and rheological properties, taking into account fractal-cluster manifestations, we used the function [28, 29]

$$\frac{\eta(\varphi,\tau)}{\eta_0}=\frac{1-\varphi_A}{(1-\varphi_A/\varphi^*)},\ \varphi_A\approx\varphi\left[1+\left(\frac{\tau_0}{\tau}\right)^{1/2}\right]^{3-D}, \quad (2)$$

where $\eta(\varphi, \tau)$ is the effective viscosity; η_0 is the liquid phase viscosity; φ_A the effective concentration of clusters; τ_0 is the ultimate shear stress; τ is the shear stress; φ is the solid phase concentration; φ^* is the critical concentration of clusters; D is the fractal dimension.

The forming structures were assessed based on the value of the fractal dimension D, which characterises the self-similarity properties of inhomogeneous, disordered objects and systems [22]. In this paper, the value of D was calculated by numerical modelling in the mathematical program Maple [29]. The modelling required solving mathematical equation (2) using the experimental data:

$$\eta = f(\tau), \quad (3)$$

where η is the effective viscosity; τ is the shear stress.

In the process of modelling we built a dependence diagram (Fig. 3). It corresponded to the experimental curve, when equation (2) was solved adequately.

We applied the method of mathematical modelling with the calculation of the fractal dimension D in order to develop ideas about the processes of formation of aggregated fractal structures of watered dispersions. By studying the values of D, we can quantitatively characterise the effect of the properties of solid phase particles on the structural and rheological parameters of dispersed systems.

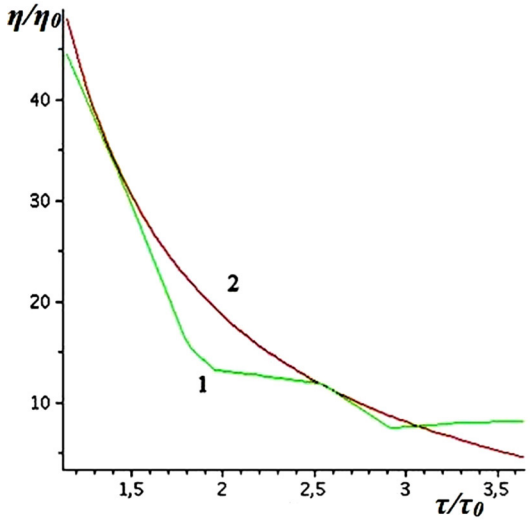

Fig. 3. Fragment of building rheological curves in the Maple program: *1* – experimental curve; *2* – the curve built by solving the mathematical equation

Optical studies of the structure of watered dispersed systems were carried out using a Biolam D-12 (Lomo, Russia), combined with a digital camera (computer-controlled Olympus SP-500 UZ). A red LED was used as a light source for the microscope. The equipment made it possible to obtain an image with a resolution of up to 300 pixels/inch with a clear outline at 10x magnification. The fractal dimension *D* was determined using the aforementioned mathematical model in the Maple program [29].

3. Results and discussion

The experimental results of the study are consistent with the known theoretical concepts of the mechanism of rheological behaviour of concentrated HDS (Fig. 4). The areas with a minimum viscosity (Fig.4a, p. 2 – p. 3) were revealed, an increase in viscosity was observed at high shear stresses p. 3 – p. 4. Then, there was again a decrease in viscosity with the discontinuity of the system at p. 4 – p. 5. From a practical point of view, it is important to note that sometimes the early manifestation of an area with an increase in viscosity (Fig. 4a, p. 3 – p. 4) at high shear stresses during technological processes does not allow the effectuation of an area that reflects the maximum dilution of mixtures.

The noted features of the manifestation of the rheological properties of the studied dispersions result from the hydrodynamic properties of particles. They are caused by the processes of the formation and destruction of the aggregated fractal-cluster structure. This explanation is confirmed by the results of optical studies of the structure of the dispersed system (Fig. 5).

In the course of the analysis and generalisation of experimental data, the impact of the properties of solid phase particles on the change in the structural and rheological characteristics of dispersed systems was estimated. The obtained data (Fig. 4, Table 1) shows that the type and nature of the solid phase particles have a significant effect on the main rheological properties of HDS. The ultimate shear stress τ_0 varies from 26 Pa (for the "limestone-water" system) to 466 Pa (for the "ash-water" system).

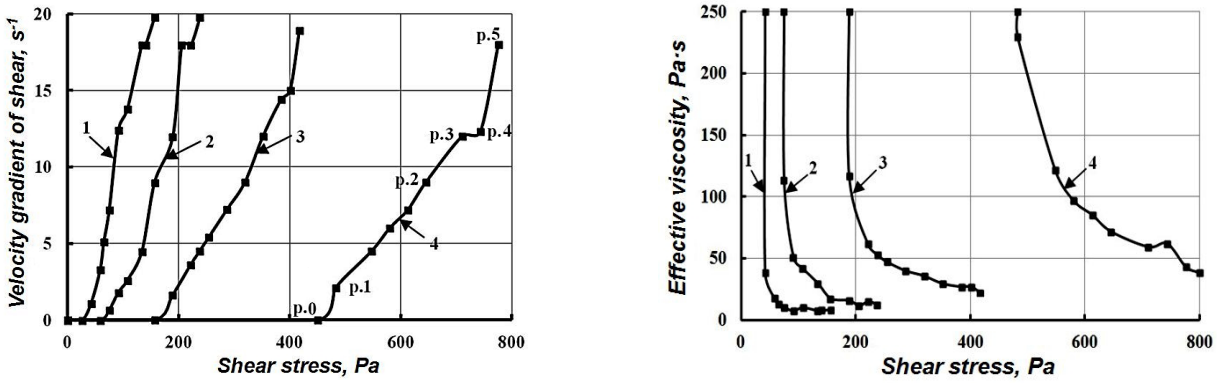

a *b*

Fig. 4. Experimental rheological curves of dispersed systems in the form of dependence of the shear velocity gradient (a) and effective viscosity (b) on shear stress (water/solid ratio is 0.32, dispersity is 500 m^2/kg)

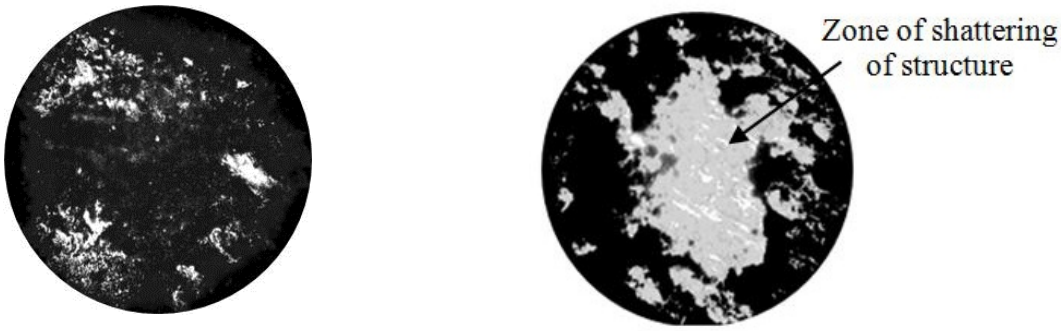

a *b*

Fig. 5. A change in the structure of the "sand-water" dispersed system with shear stress under ×10 magnification (water/solid ratio is 0.32, dispersity is 500 m^2/kg): a) the system without shear; b) the system after shear

The minimum effective viscosity η_{min} for these systems varies from 7 Pa·s to 38 Pa·s.

We determined the dependence between the values of the fractal dimension *D* and the experimental integral characteristics, which are the ultimate shear stress τ_0 and effective viscosity η_{min} (Table 1). It was shown that the fractal dimension *D* decreases in the studied systems when τ_0 and η_{min} increase. It can be assumed that the observed correlations are due to the properties of the solid phase particles. In studies [28–30], it was shown that ash particles have a more developed and rough outer and inner surface, as compared to the other studied particles. This contributes to the formation of a dispersed system with a more branched fractal-cluster structure, where the manifestation of internal forces provides the highest values of τ_0 and η_{min} with the minimum fractal dimension *D* = 2.31.

We assessed the effect of the dispersion of solid phase particles on the change in the structural and rheological properties using the example of the "sand – water" system, with a constant water/solid ratio W/S = 0.28 (Fig. 6, Table 2).

As expected, with an increase in the values of dispersity, an increase in τ_0 and η_{min} is characteristic. If we increase the dispersity of the studied system from 300 to 700 m^2/kg, τ_0 increases from 226 Pa to 389 Pa, and η_{min} increases from 21 Pa·s to 31 Pa·s. These observations can be explained by the manifestation of internal forces and a change in the nature of the forming fractal-cluster structures. This change results in a decrease in the fractal dimension *D*. Thus, the value of *D* shows that with an increase in dispersity in the watery system, a more branched microstructure is formed, with a large number of inter-particle and inter-aggregate contacts. It is

Table 1. Influence of the type of dispersed systems on their structural and rheological characteristics (water/solid ratio of 0.32, dispersity of 500 m^2/kg)

Indicator	Dispersed system			
	"limestone–water"	"sand–water"	"cement–water"	"ash–water"
τ_0, Pa	26	58	156	466
η_{min}, Pa·s	7	11	22	38
D	2.64	2.61	2.57	2.31

Table 2. Influence of the dispersity of solid phase particles on the structural and rheological characteristics of the "sand-water" system (with a water/solid ratio of 0.28)

Показатель	Dispersity, m^2/kg		
	300	500	700
τ_0, Pa	226	258	389
η_{min}, Pa·s	21	23	31
D	2.7	2.65	2.45

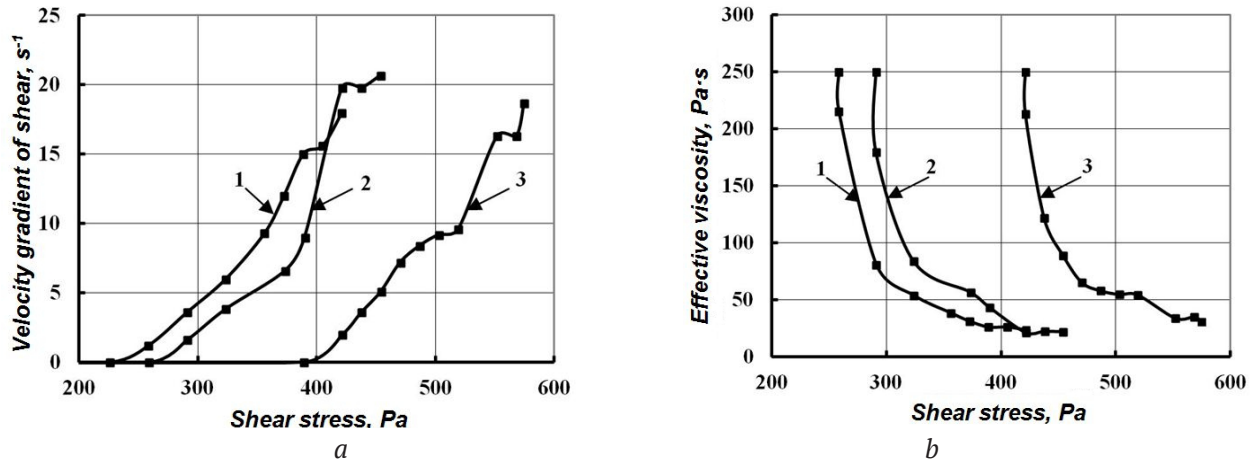

a *b*

Fig. 6. Experimental rheological curves of the "sand-water" dispersed system at water/solid ratio of 0.28 in the form of dependence of the shear velocity gradient (a) and effective viscosity (b) on shear stress

characterised by a higher void content, while the fractal dimension *D* decreases from 2.7 to 2.45.

4. Conclusions

The obtained research results expand the understanding of the mechanism of rheological behaviour of building mixtures, demonstrate the formation and destruction of fractal-cluster formations in the HDS microstructure. It was shown that the fractal dimension *D* can be used as a quantitative characteristic of the processes of structure formation of HDS at the micro level, as well as for additional assessment of their structural and rheological properties. This value can be determined by mathematical modelling using specialised software. We determined the interrelation between the fractal dimension *D* and such experimental rheological characteristics as the ultimate shear stress τ_0 and effective viscosity η. These parameters vary depending on the properties of the solid phase particles of the HDS components, which are the basis of typical building mixtures. The obtained results can be the basis for regulating the rheological properties of building mixtures and optimising the technological processes of mixing, transportation, and moulding.

Conflict of interest

The authors declare that they have no known competing financial interests or personal relationships that could have influenced the work reported in this paper.

References

1. Bazhenov Yu. M. *Tekhnologiya betona* [Concrete technology]. Moscow: ASV Publ., 2007, 528 p. (In Russ.).

2. Kastornykh L. I., Rautkin A. V., Raev A. S. Effect of water-retaining admixtures on some properties of self-compacting concretes. Part 1. Rheological characteristics of cement compositions. *Stroitel'nye Materialy* [Construction Materials Russia]. 2017;750(7): 34–38. DOI: https://doi.org/10.31659/0585-430X-2017-750-7-34-38 (In Russ., abstract in Eng.).

3. Kastornykh L. I., Detochenko I. A., Arinina E. S. Effect of water-retaining admixtures on some properties of self-compacting concretes. Part 2. Rheological characteristics of concrete mixes and strength of self-compacting concretes. *Stroitel'nye Materialy* [Construction Materials Russia]. 2017;11: 22–27. Available at: https://www.elibrary.ru/item.asp?id=30744336 (In Russ., abstract in Eng.).

4. Kalabina D. A., Yakovlev G. I., Drochitka R., Grakhov V. P., Pervushin G. N., Bazhenov K. A., Troshkova V. V. Rheological activation of fluoroanhydrite compositions with polycarboxylate esters. *Stroitel'nye Materialy* [Construction Materials Russia]. 2020;778(1–2): 38–47. DOI: https://doi.org/10.31659/0585-430X-2020-778-1-2-38-47 (In Russ., abstract in Eng.).

5. Kabagire K. D., Diederich P., Yahia A., Chekired M. Experimental assessment of the effect of particle characteristics on rheological properties of model mortar. *Construction and Building Materials*. 2017;151: 615–624. DOI: https://doi.org/10.1016/j.conbuildmat.2017.06.122

6. Kim J. S., Kwon S. H., Jang K. P., Choi M. S. Concrete pumping prediction considering different measurement of the rheological properties. *Construction and Building Materials*. 2018;171: 493–503. DOI: https://doi.org/10.1016/j.conbuildmat.2018.03.194

7. Weng Y., Lu B., Li M., Liu Z., Tan M. J., Qian S. Empirical models to predict rheological properties of fiber reinforced cementitious composites for 3D printing. *Construction and Building Materials*. 2018;189: 676–685. DOI: https://doi.org/10.1016/j.conbuildmat.2018.09.039

8. Li D., Wang D., Ren C., Rui Y. Investigation of rheological properties of fresh cement paste containing ultrafine circulating fluidized bed fly ash. *Construction and Building Materials*. 2018;188: 1007–1013. DOI: https://doi.org/10.1016/j.conbuildmat.2018.07.186

9. Pan G., Li P., Chen L., Li G. A study of the effect of rheological properties of fresh concrete on shotcrete-rebound based on different additive components. *Construction and Building Materials*. 2019;224: 1069-1080. DOI: https://doi.org/10.1016/j.conbuildmat.2019.07.060

10. Zhang S., Qiao W.-G., Chen P.-C., Xi K. Rheological and mechanical properties of microfine-cement-based grouts mixed with microfine fly ash, colloidal nanosilica and superplasticizer. *Construction and Building Materials*. 2019;212: 10–18. DOI: https://doi.org/10.1016/j.conbuildmat.2019.03.314

11. Hedayatinia F., Delnavaz M., Emamzadeh S. S. Rheological properties, compressive strength and life cycle assessment of self-compacting concrete containing natural pumice pozzolan. *Construction and Building Materials*. 2019;206: 122–129. DOI: https://doi.org/10.1016/j.conbuildmat.2019.02.059

12. Kabagire K. D., Yahia A., Chekired M. Toward the prediction of rheological properties of self-consolidating concrete as diphasic material. *Construction and Building Materials*. 2019;195: 600–612. DOI: https://doi.org/10.1016/j.conbuildmat.2018.11.053

13. Sonebi M., Abdalqader A., Fayyad T., Perrot A., Bai Y. Optimisation of rheological parameters, induced bleeding, permeability and mechanical properties of supersulfated cement grouts. *Construction and Building Materials*. 2020;262: 120078. DOI: https://doi.org/10.1016/j.conbuildmat.2020.120078

14. Roussel N. Rheological requirements for printable concretes. *Cement and Concrete Research*. 2018;112: 76–85. DOI: https://doi.org/10.1016/j.cemconres.2018.04.005

15. Feys D., Asghari A. Influence of maximum applied shear rate on the measured rheological properties of flowable cement pastes. *Cement and Concrete Research*. 2019;117: 69–81. DOI: https://doi.org/10.1016/j.cemconres.2018.12.003.

16. Li Z., Cao G. Rheological behaviors and model of fresh concrete in vibrated state. *Cement and Concrete Research*. 2019;120: 217–226. DOI: https://doi.org/10.1016/j.cemconres.2019.03.020

17. Choi B. I., Kim J. H., Shin, T. Y. Rheological model selection and a general model for evaluating the viscosity and microstructure of a highly-concentrated cement suspension. *Cement and Concrete Research*. 2019;123: 105775. DOI: https://doi.org/10.1016/j.cemconres.2019.05.020

18. Khayat K. H., Meng W., Vallurupalli K., Teng L. Rheological properties of ultra-high-performance concrete – An overview. *Cement and Concrete Research*. 2019;124: 105828. DOI: https://doi.org/10.1016/j.cemconres.2019.105828

19. Ley-Hernández A. M., Feys D., Kumar A. How do different testing procedures affect the rheological properties of cement paste? *Cement and Concrete Research*. 2020;137: 106189. DOI: https://doi.org/10.1016/j.cemconres.2020.106189

20. Wyss H. M., Tervoort E. V., Gauckler L. J. Mechanics and microstructures of concentrated particle gels. *Journal of the American Ceramic Society*. 2005;88(9): 2337–2348. DOI: https://doi.org/10.1111/j.1551-2916.2005.00622.x

21. Pertsev V. T., Ledenev A. A., Usachev S. M., Usachev A. M. Evaluation of rheological properties of building mixes with obtaining additional quantitative characteristics. *Kondensirovannye sredy i mezhfaznie granitsy = Condensed Matter and Interphases*. 2016;18(3): 394–401. Available at: https://journals.vsu.ru/kcmf/article/view/148 (In Russ., abstract in Eng.).

22. Alekseeva E. V., Bobryshev A. N., Voronov P. V., Golovinskii P. A., Lakhno A. V., Pertsev V. T. *Strukturno-reologicheskie svoistva dispersno-zernistykh sistem* [Structural and rheological properties of dispersed-granular systems]. Voronezh: VGASU Publ.; 2010. 196 p. (In Russ.).

23. Malkin A. Ya., Isaev A. I. *Reologiya: kontseptsii, metody, prilozheniya* [Rheology: concepts, methods, applications]. St. Petersburg: Professiya Publ.; 2007. 560 p. (In Russ.)

24. Shchukin E. D., Pertsov A. V., Amelina E. A. *Kolloidnaya khimiya* [Colloidal chemistry]. Moscow: Vysshaya shkola Publ.; 2007. 444 p. (In Russ.)

25. Bibik E. E. *Reologiya dispersnykh sistem* [Rheology of disperse systems]. Leningrad: Izd-vo Leningr. un-ta Publ., 1981, 172 p. (In Russ.)

26. Pertsev V. T., Ledenev A. A. Metodologicheskie podkhody k issledovaniyu reologicheskikh svoistv stroitel'nykh smesei [Methodological approaches to research rheological properties of building mixtures]. *Nauchnyi vestnik Voronezhskogo GASU. Seriya: Fiziko-khimicheskie problemy i vysokie tekhnologii stroitel'nogo materialovedeniya*. 2017; 1(14): 71–77. (In Russ.)

27. Mills P., Snabre P. The fractal concept in the rheology of concentrated suspensions. *Progress and Trends in Rheology II*. 1988: 105–108. DOI: doi.org/10.1007/978-3-642-49337-9_26

28. Ledenev A. A., Usachev S. M., Pertsev V. T. Strukturno-reologicheskie svoistva stroitel'nykh smesei [Structural and rheological properties of building mixtures]. *Stroitel'nye Materialy* [Construction Materials Russia]. 2009; 7: 68–70. Available at: https://www.elibrary.ru/item.asp?id=12830653 (In Russ.)

29. Pertsev V. T., Ledenev A. A. *Razrabotka effektivnykh kompleksnykh organomineral'nykh dobavok dlya regulirovaniya reologicheskikh svoistv betonnykh smesei* [Development of effective complex organomineral additives for regulation of rheological properties of concrete mixtures]. Voronezh: Voronezhskii GASU Publ.; 2012. 136 p. (In Russ.)

30. Pertsev V. T., Ledenev A. A., Rudakov O. B. Physical and chemical approaches to the development of effective organomineral additives for concrete. *Kondensirovannye sredy i mezhfaznie granitsy = Condensed Matter and Interphases*. 2018;20(3): 432–442. DOI: https://elibrary.ru/item.asp?id=23233672 (In Russ., Abstract in Eng.)

Information about the authors

Andrey A. Ledenev, PhD in Technical Sciences, senior research fellow, Air Force Military Educational and Scientific Centre "Air Force Academy named after Professor N.E. Zhukovsky and Y.A. Gagarin", Voronezh, Russian Federation; e-mail: ledenoff@mail.ru. ORCID ID: https://ordic.org/0000-0003-2493-8952.

Viktor T. Pertsev, DSc in Technical Sciences, Professor, professor of the Department for Technology of Construction Materials, Products, and Structures, Voronezh State Technical University, Voronezh, Russian Federation; e-mail: perec_v@mail.ru. ORCID ID: https://ordic.org/0000-0002-8882-4930.

Oleg B. Rudakov, DSc in Chemistry, Professor, Head of the Department of Chemistry and Chemical Technology of Materials, Voronezh State Technical University, Voronezh, Russian Federation; e-mail: robi57@mail.ru. ORCID ID: https://orcid.org/0000-0003-2527-2857.

Dmitriy E. Barabash, DSc in Technical Sciences, Professor, Head of the Department of Survey and Design of Airfields, Air Force Military Educational and Scientific Centre "Air Force Academy named after Professor N.E. Zhukovsky and Y.A. Gagarin", Voronezh, Russian Federation; e-mail: barabash60170@yandex.ru. ORCID ID: https://orcid.org/0000-0001-9438-8082.

All authors have read and approved the final manuscript.

Translated by Anastasiia Ananeva
Edited and proofread by Simon Cox

Condensed Matter and Interphases
(Kondensirovannye sredy i mezhfaznye granitsy)

Original articles

DOI: https://doi.org/10.17308/kcmf.2020.22/3118
Received 26 September 2020
Accepted 15 October 2020
Published online 25 December 2020

ISSN 1606-867X
eISSN 2687-0711

Estimation of Diffusion-Kinetic and Thermodynamic Properties of Al-Sm-H Alloys

© 2020 V. O. Lukyanova✉, I. Yu. Gots

Yuri Gagarin State Technical University of Saratov,
77, Politekhnicheskaya str., Saratov 410054, Russian Federation

Abstract

Metal hydride systems for hydrogen storage are now commercially manufactured and the demand for them is constantly growing. Metal hydrides have the following features: a unique combination of properties of metal-hydrogen systems; extremely high volumetric densities of hydrogen atoms in the metal matrix; a wide range of operating pressures and temperatures; the selectivity of the hydrogen absorption process; significant changes in the physical properties of the metal when it is saturated with hydrogen; their catalytic activity, etc. The purpose of our research was to study the effect of the temperature of cathodic polarisation on the diffusion-kinetic, thermodynamic, and physical properties of Al-Sm-H alloys.

In our study we used electrodes of Al-Sm-H alloys obtained electrochemically using cathodic intercalation from a 0.5 M dimethylformamide solution of samarium salicylate at $E_{ср}$ = –2.9 V (relative to the non-aqueous silver chloride electrode) and the temperature of 25 °C for 1 hour. We used the electromotive force method to determine the thermodynamic properties: Gibbs free energy (ΔG), entropy (ΔS), and enthalpy (ΔH). The potentiostatic method was used to calculate the diffusion-kinetic properties: intercalation constants, adsorption, switching current density, and the diffusion coefficient. The microstructural analysis allowed us to determine the effect of the temperature on the changes in the surface morphology.

The study showed that an increase in the temperature results in an increase in ΔG, ΔS, and ΔH, which means that at higher temperatures the degree of the system disorder increases. Nevertheless, the calculated characteristics comply with the existing literature.

Keywords: electromotive force method, rare earth elements, aluminum matrix, hydrogen, potentiostatic method, microstructure, diffusion-kinetic characteristics.

Funding: The study was supported by the Russian Foundation for Basic Research (project No. 20-33-90150).

For citation: Lukyanova V. O., Gots I. Yu. Estimation of diffusion-kinetic and thermodynamic properties of Al-Sm-H alloys. *Kondensirovannye sredy i mezhfaznye granitsy = Condensed Matter and Interphases*. 2020; 22(4): 481–488. DOI: https://doi.org/10.17308/kcmf.2020.22/3118

Для цитирования: Лукьянова В. О., Гоц И. Ю. Оценка диффузионно-кинетических и термодинамических характеристик Al-Sm-H сплавов. *Конденсированные среды и межфазные границы*. 2020; 22(4): 481–488. DOI: https://doi.org/10.17308/kcmf.2020.22/3118

✉ Victoriya O. Lukyanova, e-mail: lukyanova.viky@yandex.ru

1. Introduction

The annual depletion of fossil fuels coupled with global environmental problems makes it necessary to search for alternative energy sources which are renewable and environmentally friendly and will last hundreds of years [1]. Modern science views hydrogen as one of the alternative energy sources [2–9]. Advancement in hydrogen technologies and development of hydrogen fuel cells make it possible to use hydrogen fuel in autonomous energy sources, both mobile and stationary. Compact and safe hydrogen storage is a vital problem which plays a key role in the development of a hydrogen economy.

All of this determines the main application areas of hydrides of intermetallic compounds [10–15], which are the following: stationary hydrogen storage, on-board hydrogen storage and hydrogen transportation, hydride compressors, hydrogen getters, hydrogen separation and purification, separation of hydrogen isotopes, heat pumps, refrigerators, and hydride dispergation.

Metal hydride systems for hydrogen storage are commercially manufactured and the demand for them is growing, slowly but steadily. Metal hydrides have the following features: a unique combination of properties of metal-hydrogen systems; extremely high volumetric densities of hydrogen atoms in the metal matrix; a wide range of operating pressures and temperatures; the selectivity of the hydrogen absorption process; significant changes in the physical properties of the metal when it is saturated with hydrogen; the catalytic activity, etc.

Due to their technological flexibility, high compactness, safety, and energy efficiency, metal-hydride hydrogen storage materials are very promising and can be used in the production of efficient combined systems for hydrogen storage.

Among the most promising materials used in the hydrogen economy are alumohydrides as they have high volumetric and mass density [21–23].

The purpose our research was to study the influence of the temperature of cathodic polarisation on the diffusion-kinetic and physical properties of Al-Sm-H alloys.

2. Experimental

The matrix of the Al-Sm alloy was obtained electrochemically on aluminium foil electrodes (99.99) (GOST 11069-74) using cathodic intercalation [24] from a 0.5 M dimethylformamide (DMF) solution of samarium salicylate at $E_{ср}$ = –2.9 V (relative to the non-aqueous silver chloride electrode) and the temperature of 25 °C for 1 hour. The Al-Sm-H electrodes were obtained using pulse potentiostatic method at $E_{ср}$ = –1.6 V for 30 minutes from the DMF: H_2O solution with the volume ratio (7 : 3) and the temperature of 25 °C. The duration of the initial short pulse was 800 milliseconds.

The diffusion-kinetic properties were determined using the potentiostatic method. Potentiostatic cathodic polarisation was performed at the potential $E_{ср}$ = 1.6 V for half an hour within the temperature range from 303.15 to 333.15 K, using a P-20X potentiostat from Electrochemical Instruments (Russia) together with the software provided by the manufacturer. We used a BT8-2 thermostat from Termex (Russia) to maintain the temperature with a precision of up to ± 0.1 °C.

Hydrogen was intercalated into the AlSm alloy previously obtained on an aluminium electrode. The intercalation characterises the duration of the electrochemical discharge stage accompanied by the formation of the Al-Sm-H interstitial phase. We assume that hydrogen intercalation proceeded according to the reaction (1):

$$\text{Al-Sm}+x\text{H}^+ + xe^- \rightarrow \text{Al-Sm-H}_x. \quad (1)$$

The diffusion-kinetic properties were calculated using the methodology described in [25–27].

The amount of extracted oxygen was determined by integrating the i - t curve minus the electric charge [28]. The electric charge was determined by multiplying the residual current by the extraction time ($t_э$):

$$Q'_{\text{H}} = \int i dt - i_{ф} t_{э}, \quad (2)$$

where Q'_{H} is the electric charge spent on the oxidation of the extracted hydrogen and $i_{ф}$ is the residual current.

The total electric charge (Q_{H}) corresponding to the hydrogen absorbed by a surface unit during the chemical deposition was determined using equation (3):

$$Q_{\text{H}} = Q'_{\text{H}} / S, \quad (3)$$

where S is the area of the working surface of the electrode during the extraction.

The processes occurring during the discharge of the studied electrode were determined based on the changes in the system's thermodynamic properties during reactions (4), (5), and (6):

$$\Delta G(x,T)_p = -E_p \cdot F, \quad (4)$$

$$\Delta S(x,T)_p = F\left(\frac{dE}{dT}\right)_p, \quad (5)$$

$$\Delta H = \Delta G + T \cdot \Delta S. \quad (6)$$

The dependence $i - 1/T$ was used to determine the activation energy according to equation (7):

$$A = -2,3R\left[\frac{a\lg i}{\Delta(1/T)}\right]_\eta = -2,3R\left[\frac{\lg i_2 - \lg i_1}{\frac{1}{T_2} - \frac{1}{T_1}}\right]_\eta. \quad (7)$$

We used an AGPM-6M FULK 401163.001-01 microstructure image analyser to control and visualise the information about the linear dimensions of the microobjects and the shape of the microparticles, as well as to create an archive of microobjects. The porosity was measured using the Mikroshlif software.

3. Results and discussion

The potentiostatic study demonstrated that during the initial stage of the hydride layer formation in the Al-Sm electrode, the dependence i–t (Fig. 1) is presented as a linear plot of $i - 1/\sqrt{t}$ (Fig. 2b). This indicates the presence of the limiting stage of hydrogen diffusion in the Al-Sm alloy at the set potential and temperature.

0.5–10 seconds later, the current drop slows down dramatically (Fig. 2a, b), and the nuclei of a new phase begin to grow. This results in the formation of a continuous hydride layer. About 20 minutes later the current density i on the electrode stops changing with time, and the hydride layer continues growing due to the chemical interaction between the hydrogen and the elements of the Al-Sm alloy (Table 1). The value of the steady-state current i_{st} increases, when the cathodic polarisation potential sweeps to more negative values.

The diffusion-kinetic properties of the electrochemical intercalation of hydrogen into the Al-Sm alloy at various cathodic polarisation potentials were studied using pulse potentiostatic method at E_{cp} = –1.6 V for 30 minutes. The initial pulse was τ = 1 s.

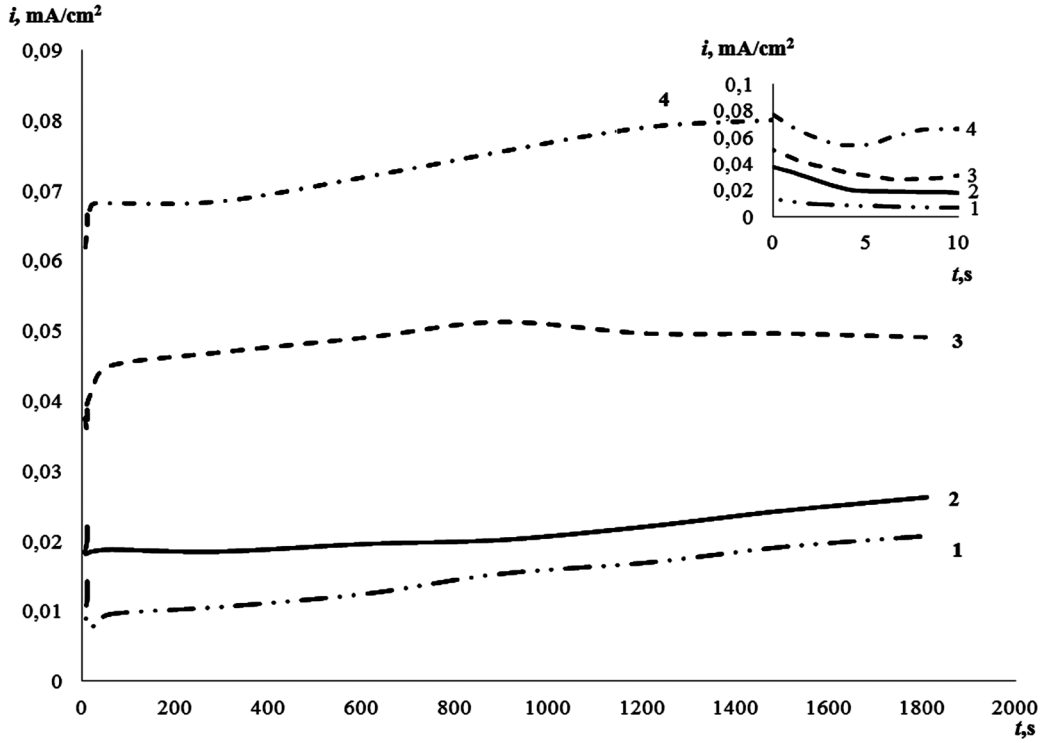

Fig. 1. Influence of the temperature on the i, t curves during hydrogen sorption by the Al-Sm alloy in aqueous organic electrolyte (V_{H_2O} : V_{DMF}) 7 : 3 for 30 minutes at the cathodic polarisation potential -E_{cp}, = 1.6 V and the temperatures: *1* – 303.15; *2* – 313.15; *3* – 323.15; *4* – 333.15 K

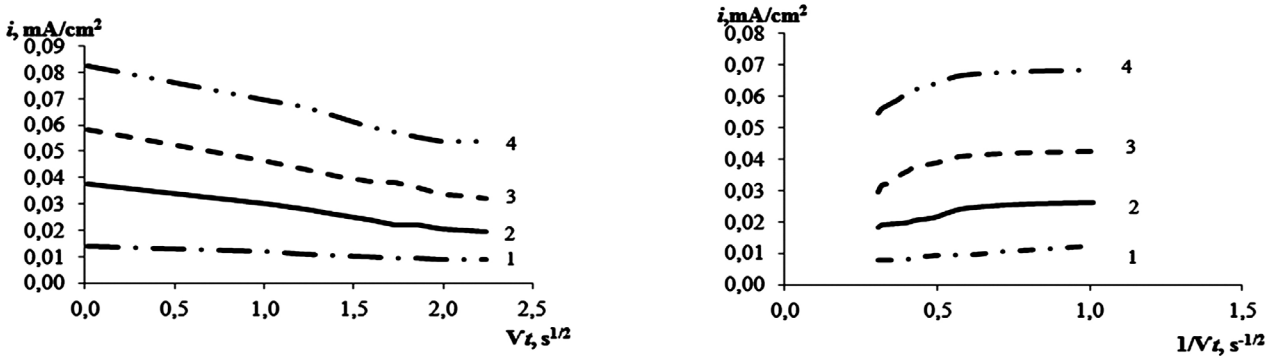

a *b*

Fig. 2. Dependence curves of i-$\sqrt{t}$ (a) and i–$1/\sqrt{t}$ (b) of hydrogen sorption by the Al-Sm alloy in an aqueous-organic electrolyte (V_{H_2O} : V_{DMF}) 7 : 3 for 30 minutes at the cathodic polarisation potential -E_{cp}, = 1.6 V and the temperatures: *1* – 303.15; *2* – 313.15; *3* – 323.15; *4* – 333.15 K

Table 1. Influence of the temperature on the nucleation process on the Al-Sm-H-electrode

Temperature (T), K	Electric charge ($Q \cdot 10^5$), A·s/cm²	Number of nuclei ($N \cdot 10^{-11}$)	Weight of nuclei ($m \cdot 10^{-18}$), g	Radius of nuclei (r), nm
303.15	2.43	10.72	0.21	1.53
313.15	5.46	2.13	2.24	3.43
323.15	7.52	1.19	6.18	4.73
333.15	10.22	0.61	15.52	6.32

The analysis of the dependence of the i–t curves (Fig. 1) of hydrogen intercalation into the Al-Sm alloy in the coordinates i–$\sqrt{t}$ (Fig. 2a), i–$1/\sqrt{t}$ (Fig. 2b) allowed us to calculate the intercalation constant K_{int}, $C_o\sqrt{D}$, the switching current being $i_{(t=0)}$.

The calculated diffusion-kinetic properties are presented in Table 2.

In the binary Al-Sm system, consisting of a hydride-forming metal (aluminium) and a rare-earth metal (REM) catalysing the hydride formation, it is possible to partially substitute some elements with others, since the interaction between metals is accompanied by the formation of intermetallic compounds, which allows for better hydride formation. The desorption of hydrogen from $MAlH_4$ alumohydrides (where M = Li, Na, K, РЗЭ) includes several stages and proceeds by means of chemical decomposition. As a result, 2 wt% hydrogen is released [29]. This changes the rate of the interaction with hydrogen.

According to the results presented in Table 2 the rate of the sorption of hydrogen by the aluminium-samarium matrix increases with the increase in temperature. This is indicated by the diffusion-kinetic properties: the intercalation constants K_{int} and $C_o\sqrt{D}$ increase by about 2.0 times, the adsorption Γ and the current density $i_{(t=0)}$ increase by about 2.1 times, and the diffusion coefficient D increases by 1.27 times.

Table 2. Diffusion-kinetic properties of the Al-Sm alloy

Temperature (T), K	ntercalation constant ($K_{int} \cdot 10^{5)}$ A·cm²/s$^{1/2}$	Diffusion component ($C_H\sqrt{D} \cdot 10^{10)}$, mol/^{2}·cm$^{-1/2}$	Steady-state current density ($i_{(t=0)}$), mA/cm²	Adsorption value ($\Gamma \cdot 10^6$), mol/cm²	Chemical diffusion coefficient of the intercalated particles ($D \cdot 10^{12)}$ cm²/s
303.15	6.444	1.182	0.061	0.842	2.64
313.15	8.527	1.564	0.073	0.961	3.06
323.15	9.882	1.813	0.084	1.283	3.36
333.15	13.011	2.386	0.133	2.351	3.54

The thermodynamic properties of the formed structures were determined using the electromotive force method (EFM) based on the stationary potential values. The thermodynamic properties of hydride formation in the aluminium-samarium alloy are given in Table 3.

According to (4), the activation energy is 39.755 kJ/mol. This means that the process is limited by the discharge stage or by a chemical reaction.

According to Table 2, values of ΔG, ΔS, and ΔH increase following the growth of temperature, which means that at higher temperatures the degree of the system disorder increases. The calculated characteristics comply with the existing literature. The mean values $\Delta G = -34.412$ kJ/mol and $\Delta H = -44.040$ kJ/mol show that the system is thermodynamically stable and can function in a wide range of temperatures.

The data regarding $E_{H2} - T$ presented in Table 3 may indicate the processes taking place in the solid phase of the active substance, as well as the structural transformations in the Al-Sm-H electrode caused by hydrogen intercalation. The conducted experiments demonstrated that all the processes are affected by the temperature. At higher temperatures hydrogen intercalates more deeply.

Taking into account the calculated characteristics, we can say that the temperature coefficient is positive. The correlation between ΔG and ΔH determines the sign of the temperature coefficient and helps to evaluate the thermal effect and the nature of the reaction taking place in the system [28]. It also helps to calculate the change in the entropy, which indicates the degree of order in the system. The change is connected with all the interactions between the system's particles and the structure of the substance [30].

When the coefficient $\Delta E/\Delta T$ is positive, the process is endothermic. By the laws of thermodynamics, the current's energy in this case is stronger than the thermal effect of the reaction, and the processes within the system are characterised by higher energy costs. Hydrogen intercalation results in significant changes in the structure of the formed compounds.

The analysis of the surface images (Fig. 3, Table 4) demonstrated the presence of rounded entities on the surface of all the studied samples. The formation of the surface structure of the samples is most likely determined by the growth and merging of such entities.

It is also possible to use the electrochemical method to determine the concentration of hydrogen absorbed during the cathodic polarisation of the Al-Sm alloy obtained by means of cathodic intercalation.

The analysis of the dependence of the $i-t$ curves in the coordinates $i-\sqrt{t}$ and $i-1/\sqrt{t}$ demonstrated that the sorption of hydrogen by the Al-Sm alloy is connected to two parallel processes: hydrogen intercalation into the Al-Sm alloy previously formed on the aluminium electrode, and the formation of a new Al-Sm-H interstitial phase. The gradient of hydrogen concentration dc/dx is large enough to ensure the diffusion required for the reaction. The formation of hydrides on the Al-Sm electrode by means of cathodic intercalation proceeds in several stages, which differ in their kinetics and the nature of phases. The first stage involves the formation of a hydrogen solid solution in Al-Sm. In this region, a gradual current drop over time is observed. This corresponds to the process being limited by diffusion, since it is extrapolated to the origin of the coordinates. The second stage involves the formation of crystal nuclei of

Table 3. Thermodynamic properties of hydride formation in the Al-Sm-H alloy

Temperature (T), K	Standard electrode potential ($-E_{st.\,(cse)}$), V	Temperature coefficient ($\Delta E/\Delta T \cdot 10^{-4}$), V/K	Average value of the temperature coefficient ($\Delta E/\Delta T \cdot 10^{-4}$), V/K	Standard electrode potential ($-E_{H_2}$), V	Gibbs free energy ($-\Delta G$), kJ/mol	Enthropy (ΔS), kJ/mol K	Enthalpy $-(\Delta H)$, kJ/mol
303.15	0.576	2.8	2. 286	0.353	34.103	27.016	42.284
313.15	0.579	2.9		0.356	34.382	27.981	43.114
323.15	0.582	3.1		0.359	34.644	29.911	47.241
333.15	0.585	3.2		0.362	34.962	30.876	45.551

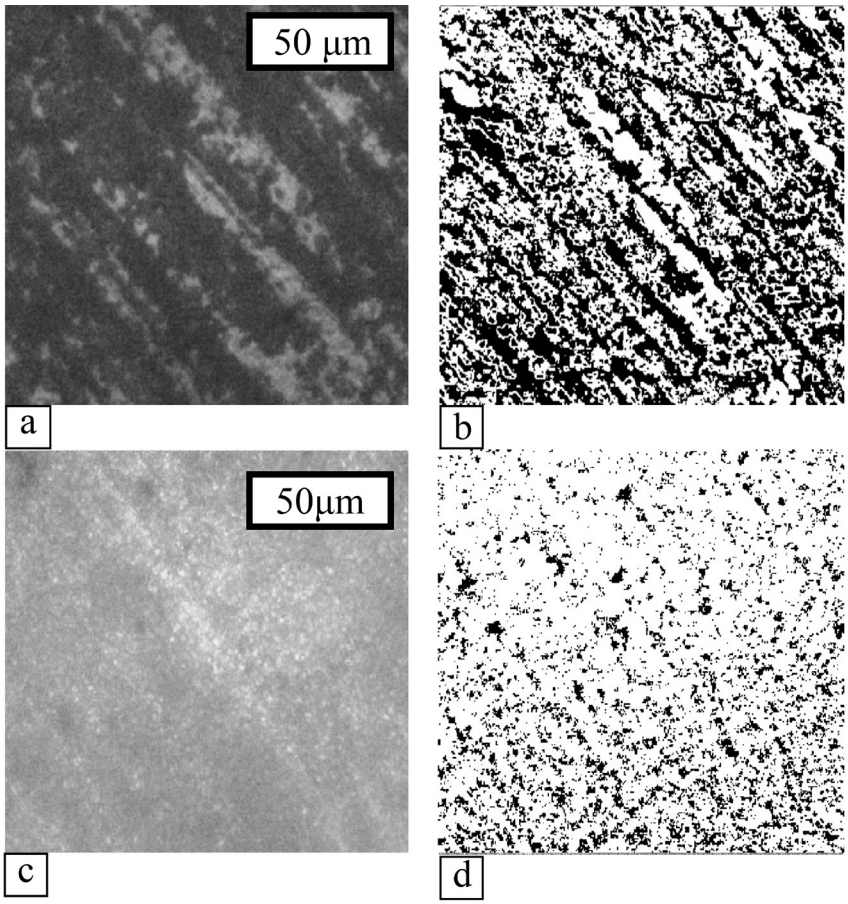

Fig. 3. Microstructure of the Al-Sm-H surface and its presentation as a binary (black and white) image using the Mikroshlif software (at T = 303.15 K (a, b) and T = 313.15 K (c, d)

Table 4. Porosity of the surface layers of the formed alloys of the Al-Sm-H system

No.	1	2	3	4
Temperature, K	303.15	313.15	323.15	333.15
Porosity, %	49	16	17	46

intermetallic compounds of hydrogen with Al and Sm, and their further growth. This results in the formation of a continuous layer of binary hydrides of the corresponding metals. The third stage involves the growth of the hydride layers of the corresponding metals due to chemical interaction of dissolved hydrogen with the Al-Sm alloy. When the formation of the intermetallic compound on the metallic/intermetallic boundary goes slowly, there is a linear dependence between the rate of the process and the potential.

4. Conclusions

The study determined the diffusion-kinetic and thermodynamic properties of the Al-Sm electrode. It demonstrated that an increase in the temperature of the electrolyte results in higher values of the diffusion-kinetic properties, namely the rate constant, the switching current density, the diffusion rate, and the value of hydrogen adsorption.

The analysis of potentiostatic curves in various coordinates demonstrated that the diffusion process is accompanied by the growth of the hydride layer, which occurs due to the chemical interaction between hydrogen and the elements of the Al-Sm alloy. The rate of hydrogen sorption by the aluminium-samarium matrix increases at higher temperatures. This is indicated by the diffusion-kinetic properties: the intercalation constants K_{int} and $C_o\sqrt{D}$ increase by about two times, the adsorption Γ and the current density $i_{(t=0)}$ increase by about 2.1 times, and the diffusion coefficient D increases by 1.27 times. The study

showed that an increase in the temperature results in an increase in ΔG, ΔS, and ΔH, which means that at higher temperatures the degree of the system disorder increases. Nevertheless, the calculated characteristics comply with the existing literature.

The highest dispersion was observed in the samples obtained at the temperature of 313.15 K. At a temperature of 313.5–323.15 K the porosity is minimal. However, at 323.15 K the breakdown points appear which become more prominent at 333.15 K.

Acknowledgements

The study was supported by the Russian Foundation for Basic Research, project No. 20-33-90150.

Conflict of interest

The authors declare that they have no known competing financial interests or personal relationships that could have influenced the work reported in this paper.

References

1. Fateev V. N., Alexeeva O. K., Korobtsev S. V., Seregina E. A., Fateeva T. V., Grigorev A. S., Aliyev A. Sh. Problems of accumulation and storage of hydrogen. *Chemical Problems*. 2018;16(4): 453–483. DOI: https://doi.org/10.32737/2221-8688-2018-4-453-483 (In Russ., abstract in Eng.)

2. Kaur M., Pal K. Review on hydrogen storage materials and methods from an electrochemical viewpoint. *Journal of Energy Storage*. 2019;23: 234–249. DOI: https://doi.org/10.1016/j.est.2019.03.020

3. Kumar D., Muthukumar K. An overview on activation of aluminium-water reaction for enhanced hydrogen production. *Journal of Alloys and Compounds*, 2020;835: 155189. DOI: https://doi.org/10.1016/j.jallcom.2020.155189

4. Litvinov V., Okseniuk I., Shevchenko D., Bobkov V. SIMS study of the surface of lanthanum-based alloys. *Ukrainian Journal of Physics*, 2018;62(10): 845. DOI: https://doi.org/10.15407/ujpe62.10.0845

5. Schneemann A., White J. L., Kang S., Jeong S., Wan L. F., Cho E. S., Heo T. W., Prendergast D., Urban J. J., Wood B. C., Allendorf M. D., Stavila V. Nanostructured metal hydrides for hydrogen storage. *Chemical Reviews*. 2018;118(22): 10775–10839. DOI: https://doi.org/10.1021/acs.chemrev.8b00313

6. Wang Y., Chen X., Zhang H., Xia G., Sun D., Yu X. Heterostructures built in metal hydrides for advanced hydrogen storage reversibility. *Advanced Materials*. 2020;32(31): 2002647. DOI: https://doi.org/10.1002/adma.202002647

7. von Colbe J. B., Ares J. R., Barale J., Baricco M., Buckley C., Capurso G., Gallandate N., Grant D. M., Guzik M. N.; Jacob I., Jensen E. H., Jensen T., Jepsen J., Klassen T., Lototskyy M. V., Manickam K., Montone A., Puszkiel J., Sartori S., Sheppard D. A., Stuart A., Walker G., Webb C. J.,Yang H.,Yartys V., Züttel A., Dornheim M. Application of hydrides in hydrogen storage and compression: Achievements, outlook and perspectives. *International Journal of Hydrogen Energy*. 2019;44(15): 7780–7808. DOI: https://doi.org/10.1016/j.ijhydene.2019.01.104

8. Milanese C., Jensen T. R., Hauback B. C., Pistidda C., Dornheim M., Yang H., Lombardo L., Zuettel A., Filinchuk Y., Ngene P., de Jongh P. E., Buckley C. E., Dematteis E. M., Baricco M. Complex hydrides for energy storage. *International Journal of Hydrogen Energy*. 2019;44(15): 7860–7874. DOI: https://doi.org/10.1016/j.ijhydene.2018.11.208

9. Abe J. O., Popoola A. P. I., Ajenifuja E., Popoola O. M. Hydrogen energy, economy and storage: review and recommendation. *International Journal of Hydrogen Energy*. 2019;44(29): 15072–15086. DOI: https://doi.org/10.1016/j.ijhydene.2019.04.068

10. He T., Cao H., Chen P. Complex hydrides for energy storage, conversion, and utilization. *Advanced Materials*. 2019;31(50): 1902757. DOI: https://doi.org/10.1002/adma.201902757

11. Luo Y., Wang Q., Li J., Xu F., Sun L., Zou Y., Chua H., Li B., Zhang K. Enhanced hydrogen storage/sensing of metal hydrides by nanomodification. *Materials Today Nano*. 2020;9: 100071. DOI: https://doi.org/10.1016/j.mtnano.2019.100071

12. Gambini M., Stilo T., Vellini M. Hydrogen storage systems for fuel cells: Comparison between high and low-temperature metal hydrides. *International Journal of Hydrogen Energy*. 2019;44(29): 15118–15134. DOI: https://doi.org/10.1016/j.ijhydene.2019.04.083

13. Kim, K. C. A review on design strategies for metal hydrides with enhanced reaction thermodynamics for hydrogen storage applications. *International Journal of Energy Research*. 2018;42(4): 1455–1468. DOI: https://doi.org/10.1002/er.3919

14. Oliveira A. C., Pavão A. C. Theoretical study of hydrogen storage in metal hydrides. *Journal of Molecular Modelling*. 2018;24(6): 127. DOI: https://doi.org/10.1007/s00894-018-3661-4

15. Møller K. T., Sheppard D., Ravnsbæk D. B., Buckley C. E., Akiba E., Li H. W., Jensen T. R. Complex metal hydrides for hydrogen, thermal and electrochemical energy storage. *Energies*. 2017;10(10): 1645. DOI: https://doi.org/10.3390/en10101645

16. Huot J., Cuevas F., Deledda S., Edalati K., Filinchuk Y., Grosdidier T., Hauback B.C., Heere M., Jensen T. R., Latroch M., Sartori S. Mechanochemistry of metal hydrides: Recent advances. *Materials*. 2019;12(17): 2778. DOI: https://doi.org/10.3390/ma12172778

17. Tarasov B. P., Fursikov P. V., Volodin A. A., Bocharnikov M. S., Shimkus Y. Y., Kashin A. M., Yartysc V. A., Chidzivad S., Pasupathid S., Lototskyy M. V. Metal hydride hydrogen storage and compression systems for energy storage technologies. *International Journal of Hydrogen Energy*. 2020. DOI: https://doi.org/10.1016/j.ijhydene.2020.07.085

18. Zhao H., Xia J., Yin D., Luo M., Yan C., Du Y. Rare earth incorporated electrode materials for advanced energy storage. *Coordination Chemistry Reviews*. 2019;390: 32–49. DOI: https://doi.org/10.1016/j.ccr.2019.03.011

19. Guzik M. N., Mohtadi R., Sartori S. Lightweight complex metal hydrides for Li-, Na-, and Mg-based batteries. *Journal of Materials Research*. 2019;34(6): 877–904. DOI: https://doi.org/10.1557/jmr.2019.82

20. Edward P. P., Kuznetsov V. L., David W. I. F. (2007). Hydrogen energy. *Philosophical Transactions of the Royal Society A: Mathematical, Physical and Engineering Sciences*. 2007;365(1853): 1043–1056. DOI: https://doi.org/10.1098/rsta.2006.1965

21. Weidenthaler C. Crystal structure evolution of complex metal aluminum hydrides upon hydrogen release. *Journal of Energy Chemistry*. 2020;42: 133–143. DOI: https://doi.org/10.1016/j.jechem.2019.05.026

22. Kunkel N., Wylezich T. Recent advances in rare earth-doped hydrides. *Zeitschrift für Anorganische und Allgemeine Chemie*. 2019;645(3): 137–145. DOI: https://doi.org/10.1002/zaac.201800408

23. Milanese C., Garroni S., Gennari F., Marini A., Klassen T., Dornheim M., Pistidda, C. Solid state hydrogen storage in alanates and alanate-based compounds: A review. *Metals*. 2018;8(8): 567. DOI: https://doi.org/10.3390/met8080567

24. Gots I. Y., Lukyanova V. O. Influence of the introducing rare-earth metal on the strength of the aluminum electrodes. *Perspektivnye Materialy*. 2020;2: 39–47. DOI: https://doi.org/10.30791/1028-978x-2020-2-39-47

25. Krapivnyj N. G. Opredelenie kineticheskih parametrov stadii proniknovenija vodoroda v metally nestacionarnym jelektrohimicheskim metodom [Determination of the kinetic parameters of the stage of hydrogen penetration into metals by a nonstationary electrochemical method] *Electrochemistry*. 1981;17(5): 672–677. (In Russ.)

26. Krapivnyj N. G. Primenenie jelektrohimicheskoj jekstrakcii dlja izuchenija navodorozhivanie metallov [Application of electrochemical extraction to the study of the hydrogenation of metals]. *Electrochemistry,* 1982;18 (9): 1174–1178. (In Russ.)

27. Pridatko K. I., Churikov A. V., Volgin M. A. Determination of lithium diffusion rate by pulse potentiostatic method. *Electrochemical Energetics*. 2003;3(4): 184–191. (In Russ., abstract in Eng.) Available at: https://energetica.sgu.ru/ru/articles/opredelenie-skorosti-diffuzii-litiya-impulsnym-potenciostaticheskim-metodom

28. Ol'shanskaja L. N., Terina E. M., Nichvolodin A. G. Thermodynamic characteristics of lithium intercalation in C_8CrO_3 electrode modified by addition of graphitizated soot. *Electrochemical Energetics*. 2001;1(4): 49–53. (In Russ., abstract in Eng.) Available at: https://energetica.sgu.ru/ru/articles/termodinamicheskie-harakteristiki-interkalatov-litiya-v-s8cro3-elektrode-modificirovannom

29. Patrikeev Yu.B., Filand Yu.M. Splavy-nakopiteli vodoroda na osnove RZJe dlja jenergopreobrazujushhih ustrojstv [Hydrogen-storage alloys for energy conversion devices]. *Alternativnaya Energetika i Ekologiya = Alternative Energy and Ecology*. 2006;7: 32. (in Russ.) Available at: https://elibrary.ru/item.asp?id=9428372

30. Golovin P. V., Medvedeva N. A., Skrjabina N. E. Katodnoe povedenie splavov na osnove titana v reakcii vydelenija vodoroda [Cathodic behavior of titanium-based alloys in the hydrogen evolution reaction]. *Bulletin of the Technological University*. 2012;15(17): 58–61. (In Russ.) Available at: https://elibrary.ru/item.asp?id=18125773

Information about the authors

Victoria O. Lukyanova, postgraduate student, Department of the Materials Chemistry and Chemical Technology, Yuri Gagarin State Technical University of Saratov, Saratov, Russian Federation; e-mail: lukyanova.viky@yandex.ru. ORCID iD: https://orcid.org/0000-0003-4656-3573.

Irina Yu. Gots, PhD in Chemistry, Associate Professor, Department of Materials Science and Biomedical Engineering, Yuri Gagarin State Technical University of Saratov, Saratov, Russian Federation; e-mail: gozt2001@mail.ru. https://orcid.org/0000-0001-5839-301X.

All authors have read and approved the final manuscript.

Translated by Yulia Dymant
Edited and proofread by Simon Cox

Condensed Matter and Interphases
(Kondensirovannye sredy i mezhfaznye granitsy)

Original articles

DOI: https://doi.org/10.17308/kcmf.2020.22/3119
Received 24 August 2020
Accepted 01 September 2020
Published online 25 December 2020

ISSN 1606-867X
eISSN 2687-0711

Structural Rearrangement of *a*-SiO_x:H Films with Pulse Photon Annealing

© 2020 V. A. Terekhov[a], E. I. Terukov[b], Yu. K. Undalov[b], K. A. Barkov[a]✉, I. E. Zanin[a], O. V. Serbin[a], I. N. Trapeznikova[b]

[a]*Voronezh State University,*
1 Universitetskaya pl., Voronezh 394018, Russian Federation

[b]*Ioffe Institute,*
26 Politekhnicheskaya str., Saint Petersburg 194021, Russian Federation

Abstract

Amorphous SiO_x films with silicon nanoclusters are a new interesting material from the standpoint of the physics, technology, and possible practical applications, since such films can exhibit photoluminescence due to size quantization. Moreover, the optical properties of these structures can be controlled by varying the size and the content of silicon nanoclusters in the SiO_x film, as well as by transforming nanoclusters into nanocrystals by means of high-temperature annealing. However, during the annealing of nonstoichiometric silicon oxide, significant changes can occur in the phase composition and the structure of the films. The results of investigations on the crystallization of silicon nanoclusters in a SiO_x matrix have shown that, even a very fast method of annealing using PPA leads to the formation of large silicon crystallites. This also causes the crystallization of at least a part of the oxide phase in the form of silicon hydroxide $H_6O_7Si_2$. Moreover, in films with an initial content of pure silicon nanoclusters ⩽ 50%, during annealing a part of the silicon is spent on the formation of oxide, and part of it is spent on the formation of silicon crystals. While in a film with an initial concentration of silicon nanoclusters ⩾ 53%, on the contrary, upon annealing, there occurs a partial transition of silicon from the oxide phase to the growth of Si crystals.

Keywords: silicon nanoclusters, silicon nanocrystals, silicon suboxides, pulse photon annealing, PPA, ultrasoft X-ray emission spectroscopy, USXES.

Funding: The study was supported by the Russian Foundation for Basic Research, project No. 19-32-90234.

A part of work was carried out with the support of the Ministry of Science and Higher Education of the Russian Federation in the framework of government order No. FZGU-2020-0036.

For citation: Terekhov V. A., Terukov E. I., Undalov Yu. K., Barkov K. A., Zanin I. E., Serbin O. V., Trapeznikova I. N. Structural rearrangement of *a*-SiO_x:H films with pulse photon annealing. *Kondensirovannye sredy i mezhfaznye granitsy = Condensed Matter and Interphases.* 2020; 22(4): 489–495. DOI: https://doi.org/10.17308/kcmf.2020.22/3119

Для цитирования: Терехов В. А., Теруков Е. И., Ундалов Ю. К., Барков К. А., Занин И. Е., Сербин О. В., Трапезникова И. Н. Структурная перестройка пленок *a*-SiO_x:H при импульсном фотонном отжиге. *Конденсированные среды и межфазные границы*. 2020;22(4): 489–495. DOI: https://doi.org/10.17308/kcmf.2020.22/3119

✉ Konstantin. A. Barkov, e-mail: barkov@phys.vsu.ru

1. Introduction

Dielectric SiO_2, Si_3N_4, and Al_2O_3 films with nanoclusters and silicon nanocrystals are of great interest as, due to size quantization, such films can exhibit photo- and electroluminescence. Moreover, if low-temperature processes (such as ion-plasma, plasma-chemical, etc.) are used to create a silicon structure, it is possible to form [1–4] amorphous *a*-SiO_x:H films with nanoclusters (*ncl*-Si), whose size will determine the luminescence region. In case of high-temperature processes at $T \geqslant 1000$ °C, as this occurs during radiation annealing of ion-implanted samples with large doses of silicon [5] or during annealing of non-stoichiometric oxides [5–8]it is possible to form silicon nanocrystals in the dielectric film matrix. The size and concentration of nanocrystals will also determine the luminescent properties of these films [9–11].

It was shown in [1,3,4] that by using the modulated plasma of a DC-magnetron in a chamber containing 80 % Ar + 20 % SiH_4, it is possible to set the number of *ncl*-Si nanoclusters in amorphous *a*-SiO_x:H films over a wide range, and thus it is easy to control the optical properties of the films. Therefore, it can be interesting to transform amorphous *a*-SiO_x films with nanoclusters into films with silicon nanocrystals by high-temperature annealing. However, during the high-temperature annealing of SiO_x films, silicon is reduced from nonstoichiometric oxide [8]. The appearance of excess Si in the *a*-SiO_x + *ncl*-Si film will lead to an increase in the size of the nanocrystals as a result of their coalescence and due to photoluminescence quenching. Therefore, this work proposes to carry out short-term pulse photon annealing of *a*-SiO_x films with silicon nanoclusters to form small-sized silicon nanocrystals (*nc*-Si).

2. Experiment

This work involved studying samples of *a*-SiO_x:H + *ncl*-Si films (400 nm in thickness) of three compositions with a silicon nanoclusters content of about 15, 50, and 53%. The studied films were grown using modulated DC-magnetron plasma at the temperature of Si (100) substrate $Ts = 265$ °C. A mixture of 80% Ar + 20 % SiH_4 with added oxygen ~15.5 mol % was used as a plasma-forming gas [4]. These samples were annealed in vacuum (10^{-5} Torr) using pulsed photon annealing (PPA) [12]. The PPA was performed using the UOLP-1M irradiation system containing three gas discharge xenon lamps with a working wavelength range of $\lambda = 0.2–1.2$ μm and operating in the pulse mode with the duration of the pulses being 10^{-2} s. The samples were annealed from the side of the silicon substrate, since the optical radiation of a xenon lamp passes through the SiO_x layer almost without absorption, and all the energy is absorbed in the silicon substrate. This can lead to the SiO_x film snapping due to the high stresses arising at the SiO_x film – Si substrate interface.

The study of the possibility to form silicon nanocrystals was carried out by X-ray diffraction (XRD) using a PANalytical Empyrean B.V. diffractometer with monochromatic Cu $K_{\alpha 1}$ radiation (Centre for Collective Use of Scientific Equipment of VSU). In addition, to simultaneously control both crystalline and amorphous phases based on silicon, the films were analysed by Ultrasoft X-ray Emission Spectroscopy (USXES) using a RSM-500 spectrometer [13, 14]. In this case, the film was irradiated with fast electrons (energy of 3 keV, which corresponds to an analysis depth of 60 nm[15]), and the characteristic Si $L_{2,3}$ X-ray radiation arising from electron transitions from the valence band to a vacancy at the Si *2p* core level was analysed. As a result, we obtain information about the energy distribution of valence electrons throughout the valence band. Thus, USXES allows detecting the presence of Si-Si or Si-O bonds, regardless of the ordering degree of the film's atomic structure [13–16].

3. Results and discussion

3.1. XRD investigations

Fig. 1 shows the diffraction patterns of *a*-SiO_x:H films annealed using PPA with two doses of 140 J/cm^2 + 180 J/cm^2. Annealing at 140 J/cm^2 did not lead to crystallization of particles in the film. Additional annealing at 180 J/cm^2 led to the appearance of two reflections of the crystalline phases at $2\theta = 23.94^o$ and 28.9^o. The reflection at 28.9^o corresponds to *d*-spacing with $d = 3.13$ Å, and at 23.94^o to *d*-spacing with $d = 3.71$ Å. A search in the international database of crystallographic data [17] showed that the plane with $d = 3.13$ Å can be easily attributed to crystalline silicon and the appearance of this reflection is associated with

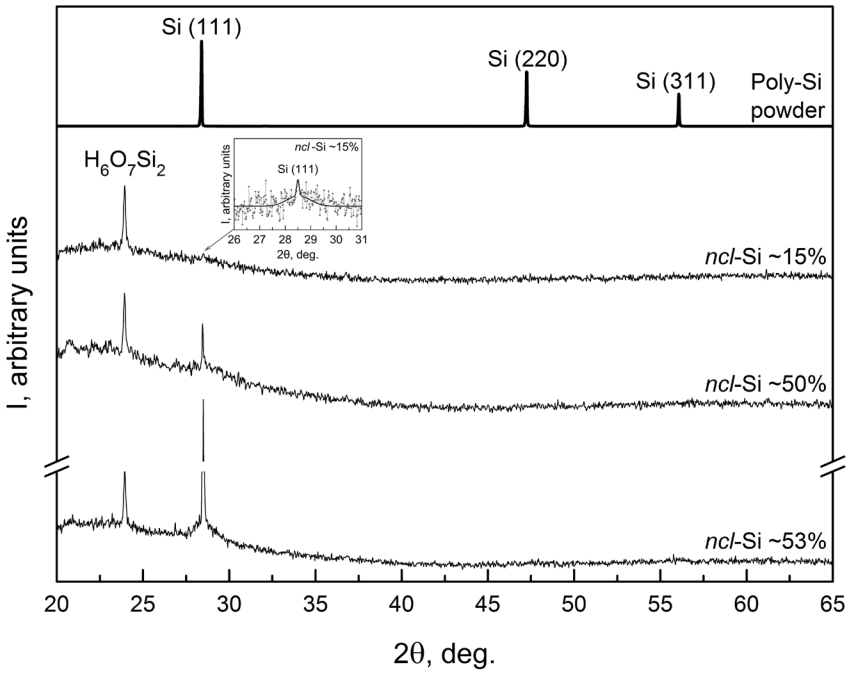

Fig. 1. XRD patterns of poly-Si powder and *a*-SiO_x:H samples with a *ncl*-Si content of about 15 %, 50 %, and 53 % after PPA 140+180 J/cm^2

the crystallization of silicon nanoclusters. While the reflection with d = 3.71 Å can be explained by the formation of the silicon hydroxide $H_6O_7Si_2$ (Fig. 1) [18]. The formation of $H_6O_7Si_2$ hydroxide upon annealing can be explained by the fact that the initial *a*-SiO_x:H films obtained in the magnetron plasma contain a large amount of hydrogen, which when heated easily reacts with SiO_x radicals.

A comparative analysis of the XRD patterns of samples with different silicon nanoclusters contents (from ~ 15 to 53 %) revealed that the changes in the diffraction pattern were of an expected character (Fig. 1). In the film with a content of silicon nanoclusters ~ 15 %, the most intense reflection is due to silicon hydroxide $H_6O_7Si_2$, while the reflection from *c*-Si is rather weak (Fig. 1). In the sample with a nanocluster content of about 50 %, the intensity of the silicon (*c*-Si) reflection Si (111) sharply increased. However, the intensity of the hydroxide reflection remained slightly higher. In the sample with the maximum concentration of silicon clusters (53 %), the *c*-Si reflection became predominant after annealing (Fig. 1). Thus, an increase in the concentration of silicon nanoclusters in the initial SiO_x film upon PPA leads to an increase in the *c*-Si content so that the Si (111) reflection intensity increases by an order of magnitude (Table 1).

However, a sharp increase in the phase of crystalline silicon cannot be explained only by an increase in the concentration of silicon

Table 1. Position and intensity of reflections in XRD patterns of *a*-SiO_x films with different *ncl*-Si content

Sample	Phase assignment	XRD line position 2θ, deg.	*d*-spacing, Å	Intensity, cts	Rel. intensity, %
ncl-Si 15 %	$H_6O_7Si_2$ Si(111)	23.9366 28.4907	3.71461 3.13035	396 45	100.00 11.52
ncl-Si 50 %	$H_6O_7Si_2$ Si(111)	23.9323 28.4663	3.71525 3.13297	282 222	100.00 78.84
ncl-Si 53 %	$H_6O_7Si_2$ Si(111)	23.9406 28.4924	3.71399 3.13016	331 3496	9.47 100.00
Poly-Si powder (reference)	Si(111) Si(220) Si(311)	28,4020 47.2600 56.081	3,1399 1.922 1.6386	23365 14749 8159	100.00 63.12 34.92

nanoclusters in the initial film, since this increase is not large (50 % → 53 %). Therefore, we carried out further studies to estimate the content of not only crystalline, but also amorphous silicon phases in these films by the USXES method [13–16].

3.2. Ultrasoft X-ray Emission Spectroscopy

Fig. 2 shows the X-ray emission Si $L_{2,3}$-spectra of the films before (a) and after (b) PPA, obtained at an analysis depth of 60 nm (experimental spectra are shown by dots, spectra simulated using reference spectra are shown by a solid line). While Fig. 3 shows the reference Si $L_{2,3}$-spectra of the *c*-Si, *a*-Si, $SiO_{1.3}$, $SiO_{1.7}$, and SiO_2. The Si $L_{2,3}$-spectra of $SiO_{1.3}$ and $SiO_{1.7}$ suboxides were obtained in [14]. As can be seen from Fig. 2, the spectra of the initial and annealed films clearly differ in the contribution to the fine structure components due to the presence of Si-O bonds (peaks at 89.5 eV and 94.5 eV), as well as Si-Si bonds (peaks at 92 eV and 89.6 eV) (Fig. 2). In the annealed film with a minimum initial amount of silicon ~ 15 %, the spectrum is close to that of pure SiO_2 (Figs. 2 and 3). A comparison with the spectrum of the initial film (Fig. 2a) indicated a decrease in the intensity in the region of 92 eV, i.e. in the region of the main maximum of the spectrum in *c*-Si, which indicates a decrease in the content of elemental silicon in the film after annealing. In addition, an analysis of the films phase composition by modelling the Si $L_{2,3}$-spectra (Table 2) did not detect crystalline silicon (with a precision of ~ 5 %), which was expected from the shape of the Si $L_{2,3}$-spectrum of annealed SiO_x film (*ncl*-Si ~15 %). At the same time, X-ray diffraction revealed a low amount of Si crystals in the SiO_2 film (Fig. 1). In the sample with a high Si initial content (~ 50 %), if compared to the initial amorphous film (Figs. 2a and 2b), annealing also leads to a decrease in the fine structure intensity due to elemental Si, i.e. to a decrease in the silicon phase content in the composite film.

At the same time, in the film with a maximum content of silicon nanoclusters (~ 53 %), annealing led to changes of different character in the ratio of oxide phases to elemental silicon. Namely, the main maximum (at 92 eV) in the Si $L_{2,3}$-spectrum of annealed film was formed by *c*-Si (Fig. 2a) and the oxide phase content decreased. Phase composition analysis by means of computer simulation of the spectra (the simulated spectra are shown in Fig. 3a and 3b with a solid line) and its results shown in Table 2 confirm our qualitative reasoning.

These results explain the unusual sharp increase in the intensity of silicon reflection after

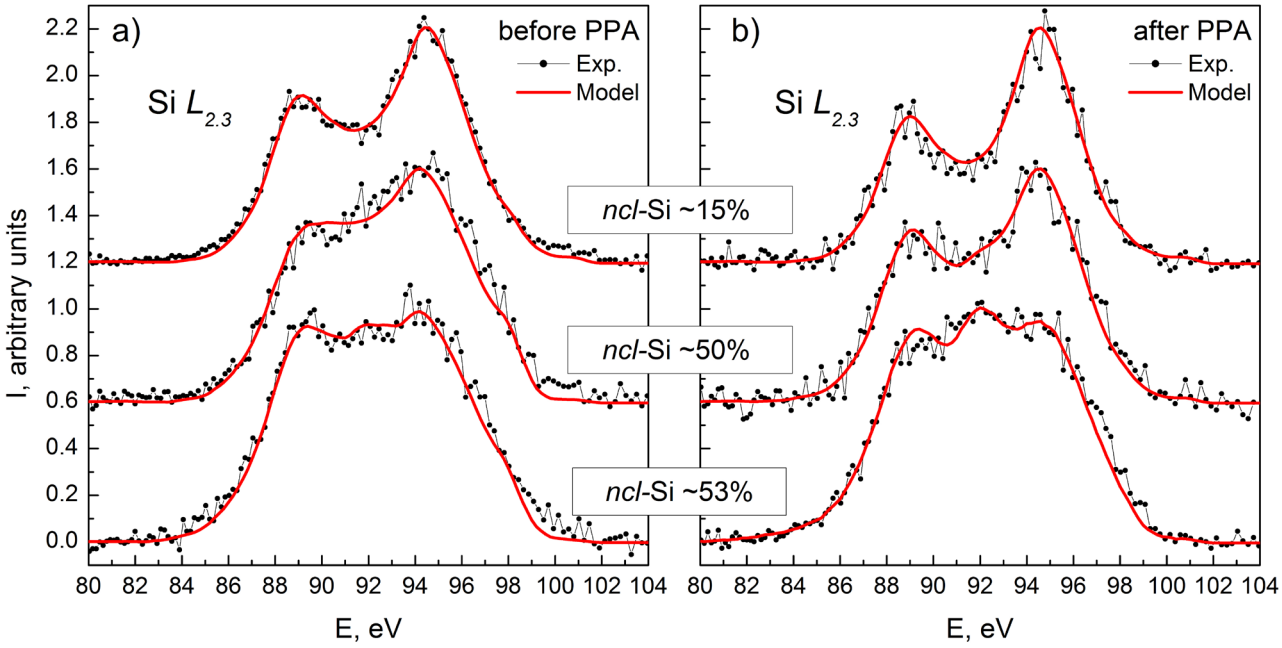

Fig. 2. Ultrasoft X-ray emission Si $L_{2,3}$-spectra of *a*-SiO$_x$:H films with different *ncl*-Si content before PPA (a) [4] and after PPA (b). Experimental spectra are shown by dots, spectra simulated using reference spectra are shown by solid lines

Table 2. Phase composition of SiO_x films with different *ncl*-Si content after PPA by USXES data

Sample	*c*-Si, %	$SiO_{1.7}$, %	SiO_2, %	Error, %
ncl-Si ~15 %	–	30	70	~10
ncl-Si ~50 %	25	15	60	
ncl-Si ~53 %	60	–	40	

annealing of the film with the initial content of *ncl*-Si nanoclusters ~53 %. That is, if the *ncl*-Si content in the films is < 50 %, during annealing some of the silicon is oxidised and does not participate in the formation of silicon crystals. While with an *ncl*-Si content of ⩾ 53 %, when silicon atoms predominate in the structural network, some of the Si atoms are reduced from SiO_x, i.e. SiO_x decomposes $SiO_x \xrightarrow{t^\circ} Si + O_2$ and participates in the formation of silicon crystals [8]. As a result, we observe a sharp increase in the intensity of the silicon reflection in the XRD patterns of SiO_x films with a high initial *ncl*-Si content.

4. Conclusions

Thus, the results of investigations on the silicon nanoclusters crystallization in a SiO_x matrix have shown that even a very fast method of annealing using PPA leads to the formation of large silicon crystallites. This also causes the crystallization of at least a part of the oxide phase in the form of silicon hydroxide $H_6O_7Si_2$. Moreover, in films with an initial content of pure silicon nanoclusters ⩽ 50 %, during annealing part of the silicon is spent on the formation of oxide, and part of it is spent on the formation of silicon crystals. While in a film with an initial concentration of silicon nanoclusters ⩾ 53 %, on the contrary, upon annealing, there occurs a partial transition of silicon from the oxide phase to the growth of Si crystals.

Acknowledgements

The study was supported by the Russian Foundation for Basic Research, project No. 19-32-90234.

A part of work was carried out with the support of the Ministry of Science and Higher Education of the Russian Federation in the framework of government order No. FZGU-2020-0036.

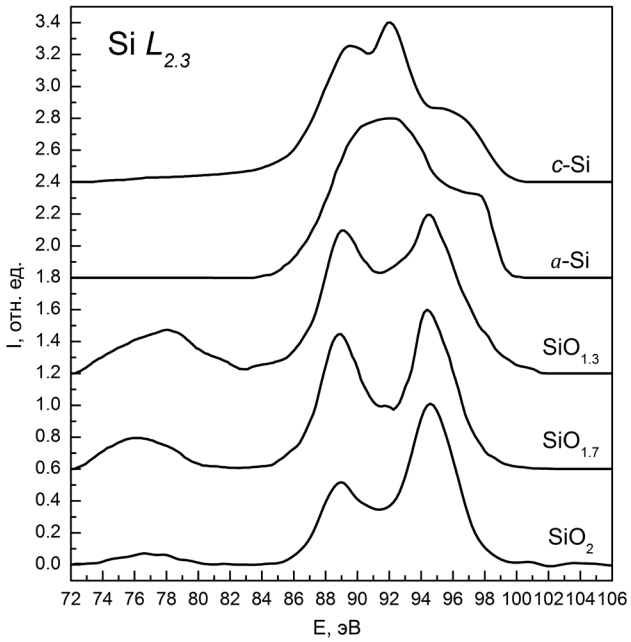

Fig. 3. Ultrasoft X-ray emission Si $L_{2,3}$-spectra of crystalline silicon *c*-Si, amorphous silicon *a*-Si, nonstoichiometric silicon oxide $SiO_{1.3}$ and $SiO_{1.7}$ [14], and silicon dioxide SiO_2

Conflict of interest

The authors declare that they have no known competing financial interests or personal relationships that could have influenced the work reported in this paper.

Reference

1. Undalov Y. K., Terukov E. I., Silicon nanoclusters ncl-Si in a hydrogenated amorphous silicon suboxide matrix a-SiOx:H (0 < x < 2). *Semiconductors*. 2015;49(7): 867–878. DOI: https://doi.org/10.1134/S1063782615070222

2. Kim K. H., Johnson E. V., Kazanskii A. G., Khenkin M. V., Roca P. Unravelling a simple method for the low temperature synthesis of silicon nanocrystals and monolithic nanocrystalline thin films. *Scientific Reports*. 2017;7(1) DOI: https://doi.org/10.1038/srep40553

3. Undalov Y. K., Terukov E. I., Trapeznikova I. N. Formation of ncl-Si in the amorphous matrix a-SiOx:H

located near the anode and on the cathode, using a time-modulated DC plasma with the (SiH_4–Ar–O_2) gas phase (Co_2 = 21.5 mol%). *Semiconductors*. 2019;53(11): 1514–1523. DOI: https://doi.org/10.1134/S1063782619110228

4. Terekhov V. A., Terukov E. I., Undalov Y. K., Parinova E. V., Spirin D. E., Seredin P. V., Minakov D. A., Domashevskaya E. P. Composition and optical properties of amorphous a-SiOx:H films with silicon nanoclusters. *Semiconductors*. 2016;50(2): 212–216. DOI: https://doi.org/10.1134/S1063782616020251

5. Terekhov V. A., Turishchev S. Y., Kashkarov V. M., Domashevskaya E. P., Mikhailov A. N., Tetelbaum D. I. Silicon nanocrystals in SiO_2 matrix obtained by ion implantation under cyclic dose accumulation. *Physica E: Low-dimensional Systems and Nanostructures*. 2007;38(1-2): 16–20. DOI: https://doi.org/10.1016/j.physe.2006.12.030

6. Terekhov V. A., Turishchev S. Y., Pankov K. N., Zanin I. E., Domashevskaya E. P., Tetelbaum D. I., Mikhailov A. N., Belov A. I., Nikolichev D. E., Zubkov S. Y. XANES, USXES and XPS investigations of electron energy and atomic structure peculiarities of the silicon suboxide thin film surface layers containing Si nanocrystals. *Surface and Interface Analysis*. 2010;42(6-7): 891–896. DOI: https://doi.org/10.1002/sia.3338

7. Terekhov V. A., Turishchev S. Y., Pankov K. N., Zanin I. E., Domashevskaya E. P., Tetelbaum, Mikhailov A. N., Belov A. I., Nikolichev D. E. Synchrotron investigations of electronic and atomic-structure peculiarities for silicon-oxide films' surface layers containing silicon nanocrystals. *Journal of Surface Investigation. X-ray, Synchrotron and Neutron Techniques*. 2011;5(5): 958–967. DOI: https://doi.org/10.1134/S102745101110020X

8. Sato K., Izumi T., Iwase M., Show Y., Morisaki H., Yaguchi T., Kamino T. Nucleation and growth of nanocrystalline silicon studied by TEM, XPS and ESR. *Applied Surface Science*. 2003;216 (1-4): 376–381. DOI: https://doi.org/10.1016/S0169-4332(03)00445-8

9. Ledoux G., Gong J., Huisken F., Guillois O., Reynaud C. Photoluminescence of size-separated silicon nanocrystals: Confirmation of quantum confinement. *Applied Physics Letters*. 2002;80(25): 4834–4836. DOI: https://doi.org/10.1063/1.1485302

10. Patrone L., Nelson D., Safarov V. I., Sentis M., Marine W., Giorgio S. Photoluminescence of silicon nanoclusters with reduced size dispersion produced by laser ablation. *Journal of Applied Physics*. 2000;87(8): 3829–3837. DOI: https://doi.org/10.1063/1.372421

11. Takeoka S., Fujii M., Hayashi S. Size-dependent photoluminescence from surface-oxidized Si nanocrystals in a weak confinement regime. *Physical Review B*. 2000;62(24): 16820–16825. DOI: https://doi.org/10.1103/PhysRevB.62.16820

12. Ievlev V. M. Activation of solid-phase processes by radiation of gas-discharge lamps, *Russian Chemical Reviews*. 2013;82(9): 815–834. DOI: https://doi.org/10.1070/rc2013v082n09abeh004357

13. Zimkina T. M., Fomichev V. A. *Ultrasoft X-Ray spectroscopy*. Leningrad: Leningrad State University Publ.; 1971. 132 p. (in Russ.)

14. Wiech G., Feldhütter H. O., Šimůnek A. Electronic structure of amorphous SiOx:H alloy films studied by X-ray emission spectroscopy: Si K, Si L, and O K emission bands. *Physical Review B*. 1993;47(12): 6981–6989. DOI: https://doi.org/10.1103/PhysRevB.47.6981

15. Domashevskaya E. P., Peshkov Y. A., Terekhov V. A., Yurakov Y. A., Barkov K. A., Phase composition of the buried silicon interlayers in the amorphous multilayer nanostructures [(Co45Fe45Zr10)/a-Si:H]41 and [(Co45Fe45Zr10)35(Al_2O_3)65/a-Si:H]41. *Surface and Interface Analysis*. 2018;50(12-13): 1265–1270. DOI: https://doi.org/10.1002/sia.6515

16. Terekhov V. A., Kashkarov V. M., Manukovskii E. Yu., Schukarev A. V., Domashevskaya E. P. Determination of the phase composition of surface layers of porous silicon by ultrasoft X-ray spectroscopy and X-ray photoelectron spectroscopy techniques. *Journal of Electron Spectroscopy and Related Phenomena*. 2001;114–116: 895–900. DOI: https://doi.org/10.1016/S0368-2048(00)00393-5

17. JCPDS-International Centre for Diffraction Data ICDD PDF-2, (n.d.) card No 01-077-2110.

18. JCPDS-International Centre for Diffraction Data ICDD PDF-2, (n.d.) card No 00-050-0438.

Information about the authors

Vladimir A. Terekhov, DSc in Physics and Mathematics, Professor at the Department of Solid State and Nanostructure Physics, Voronezh State University, Voronezh, Russian Federation; e-mail: ftt@phys.vsu.ru. ORCID iD: https://orcid.org/0000-0002-0668-4138.

Evgeny I. Terukov, DSc in Technical Sciences, Head of the Laboratory of Physical and Chemical Properties of Semiconductors, Ioffe Institute of the Russian Academy of Sciences, Saint Petersburg, Russian Federation; e-mail: Eug.Terukov@mail.ioffe.ru. ORCID iD: https://orcid.org/0000-0002-4818-4924.

Yury K. Undalov, PhD in Technical Sciences, Senior Researcher at the Laboratory of Physical and Chemical Properties of Semiconductors, Ioffe Institute of the Russian Academy of Sciences, Saint Petersburg, Russian Federation; e-mail: undalov@mail.ioffe.ru.

Konstantin A. Barkov, PhD student, Head of the Laboratory, Department of Solid State and Nanostructure Physics, Voronezh State University, Voronezh, Russian Federation; e-mail: barkov@phys.

vsu.ru ORCID iD: https://orcid.org/0000-0001-8290-1088.

Igor E. Zanin, PhD in Physics and Mathematics, Assistant Professor at the Department of General Physics, Voronezh State University, Voronezh, Russian Federation; e-mail: iezan@mail.ru

Oleg V. Serbin, PhD in Physics and Mathematics, Assistant Professor of the Department of Materials Science and the Industry of Nanosystems, Voronezh State University, Voronezh, Russian Federation; e-mail: deanery@chem.vsu.ru. ORCID iD: https://orcid.org/0000-0002-2407-1183.

Irina N. Trapeznikova, DSc in Physics and Mathematics, Professor, Ioffe Institute of the Russian Academy of Sciences, Saint Petersburg, Russian Federation; e-mail: trapez@mail.ioffe.ru. ORCID iD: https://orcid.org/0000-0002-2244-8370.

All authors have read and approved the final manuscript.

Translated by Irina Charychanskaya
Edited and proofread by Simon Cox

Condensed Matter and Interphases
(Kondensirovannye sredy i mezhfaznye granitsy)

Original article

DOI: https://doi.org/10.17308/kcmf.2020.22/3120
Received 30 October 2020
Accepted 15 November 2020
Published online 25 December 2020

ISSN 1606-867X
eISSN 2687-0711

The Synthesis of Nanophosphors $YP_xV_{1-x}O_4$ by Spray Pyrolysis and Microwave Methods

© 2020 E. V. Tomina[a, b]✉, D. A. Lastochkin[a], S. A. Maltsev[a]

[a]*Voronezh State University,*
1 Universitetskaya pl., Voronezh 394018, Russian Federation

[b]*Voronezh State University of Forestry and Technologies named after G. F. Morozov,*
ul. Timiryazeva, 8, Voronezh 394087, Russian Federation

Abstract

Due to rare earth doping, phosphates and vanadates are the leading materials for the synthesis of phosphors due to their thermal stability, low sintering temperature, and chemical stability. Phosphors in the nanoscale state are of particular interest. The simple, fast, and scalable synthesis of nanophosphors with high chemical homogeneity is a priority task. The purpose of this work was to synthesize powders of mixed yttrium vanadate-phosphate crystals of various compositions by coprecipitation under the action of microwave radiation and spray pyrolysis, as well as to compare the characteristics of the obtained samples.

Samples of $YV_xP_{1-x}O_4$ of different compositions were synthesized by coprecipitation under the action of microwave radiation and spray pyrolysis in different modes. In the case of the synthesis of yttrium vanadate-phosphate $YV_xP_{1-x}O_4$ by spray pyrolysis followed by annealing, according to the X-ray phase analysis data, single-phase nanopowders were formed. The morphological characteristics of the samples were revealed by the methods of transmission electron microscopy and scanning electron microscopy. Depending on the annealing conditions, the samples were either faceted or spherical particles less than 100 nm in size. The composition of the $YV_xP_{1-x}O_4$, samples synthesized by the coprecipitation method under the action of microwave radiation strongly depended on the pH of the precursor solution. The minimum content of impurity phases was reached at pH 9.

Spray pyrolysis allows the synthesis of yttrium vanadate phosphate $YV_xP_{1-x}O_4$ nanopowders of high chemical homogeneity with a particle size of less than 100 nm. The maximum chemical homogeneity of yttrium vanadate-phosphate powders was achieved at pH = 9 during the synthesis of $YV_xP_{1-x}O_4$ by coprecipitation under the action of microwave radiation. However, the particle size dispersion was large, within the range of 2–60 μm.

Keywords: phosphors, microwave synthesis, spray pyrolysis, nanopowders, yttrium vanadate-phosphate.

For citation: Tomina E. V., Lastochkin D. A., Maltsev S. A. The synthesis of nanophosphors $YP_xV_{1-x}O_4$ by spray pyrolysis and microwave methods. *Kondensirovannye sredy i mezhfaznye granitsy = Condensed Matter and Interphases*. 2020;22(4): 496–503. DOI: https://doi.org/10.17308/kcmf.2020.22/0000

Для цитирования: Томина Е. В., Ласточкин Д. А., Мальцев С. А. Синтез нанолюминофоров $YP_xV_{1-x}O_4$ спрей-пиролитическим и микроволновым методами. Конденсированные среды и межфазные границы. 2020;22(4): 496–503. DOI: https://doi.org/10.17308/kcmf.2020.22/3120

✉ Elena V. Tomina, e-mail: tomina-e-v@yandex.ru

1. Introduction

The areas for the application of luminescent materials are diverse: lighting devices, biological markings, plasma panels, and biomedicine [1–4]. Phosphors in the nanoscale state are of particular interest. Phosphates and vanadates are the leading materials for the synthesis of phosphors due to rare earth doping due to their thermal stability, low sintering temperature, chemical stability, and environmental friendliness [5]. Systems of mixed crystals of vanadate-phosphates demonstrate better luminescent properties in comparison with the corresponding vanadates and phosphates [6]. Thus, the quantum yields of europium-doped vanadate phosphate nanoparticles reach 20%, and such mixed crystals can potentially be a red emitting phosphor for PDP [7–9].

Nanophosphors can be synthesized by sol-gel, hydrothermal, and microemulsion methods [10–15]. The use of microwave heating leads to a significant increase in the reaction rate and makes it possible to reduce the synthesis time from several hours or days to several minutes while increasing the purity of the target product [16–18]. The synthesis of nanopowders by aerosol pyrolysis has a number of advantages: high productivity, high purity of the final product, the ability to control morphology and low energy consumption. Aerosol spray pyrolysis (CSP) is in great demand due to its simplicity and low cost [19]. Pyrolytic synthesis products find applications in areas such as catalysis, chromatography, the manufacture of pigments and photoluminescent materials.

The aim of this work was to synthesize mixed crystals of yttrium vanadate phosphate by coprecipitation methods under the action of microwave radiation and spray pyrolysis.

2. Experimental

Vanadium (V) V_2O_5 oxide (AR grade TU 6-09-4093-88), sodium phosphate Na_3PO_4 (AR grade, National product classification code 26 2112 1152 00 GOST 9337-79), yttrium nitrate Y $(NO_3)_3$ (AR grade, CAS 13494-98-9), sodium hydroxide NaOH (AR grade, GOST 432877) served as precursors. For the synthesis of sodium metavanadate, vanadium (V) oxide and sodium hydroxide were mixed in an equivalent ratio, after dissolving them in distilled water. Equivalent amounts of sodium orthophosphate and yttrium nitrate were added to the resulting solution, exposed to microwave radiation (P_{max} source – 800 W, operating frequency – 2450 MHz) three times within 5 min at 800 W. The pH of the solution was maintained in the range from 7 to 9. The synthesized powder was subjected to ultrasonic dispersion (ultrasonic bath VU-09- "Ya-FP" -0) for 10–15 min. After filtration, the powder was dried for two days, ground in a mortar, and annealed in a muffle furnace (SNOL 8.2/1100) at 800 °C for 1–2 h.

For the synthesis of yttrium vanadate phosphate by the spray pyrolysis method, vanadium (V) oxide V_2O_5 was mixed in an equivalent amount with NaOH to obtain sodium metavanadate ($NaVO_3$). Then, with vigorous stirring, a stoichiometric amount of yttrium nitrate crystalline hydrates $Y(NO_3)_3$, sodium phosphate Na_3PO_4 and concentrated nitric acid HNO_3 (GOST 4461-77) were added for the prevention of the hydrolysis of the solution in the dispersant. The synthesis of nanoparticles was carried out in a spray pyrolysis unit (Fig. 1).

The solution was filled in portions into a disperser, which was connected through branch pipes to a compressor and a quartz tube reactor. The dispersant sprayed the solution in the form of an aerosol into the reactor of the MTP-2M furnace, heated to a temperature of 600 °C. The temperature was controlled by an OVEN TRM1-Shch1.U.R thermostat with an error of ± 1 °C. In the furnace, under the influence of temperature, the aerosol pyrolytically decomposed with the formation of yttrium vanadate phosphate. The nanopowder was collected into a glass with distilled water, then filtered, dried in air, and thermally annealed in a muffle furnace (SNOL 8.2/1100) for recrystallization and complete dehydration at 800 °C for 1–2 hours.

The phase composition of the synthesized powders was determined by X-ray diffraction analysis (XPD) using an ARL X'TRA diffractometer (Cu $K_{\alpha 1}$ with λ = 1.540562 Å) in continuous mode. The size of the coherent scattering regions (CSR) according to the X-ray diffraction analysis (XPD) data for the samples of yttrium vanadate phosphate was calculated using the Scherrer formula [20]:

$$D_{hkl} = \frac{kx\lambda}{\beta_{hkl} \times \cos\theta}$$

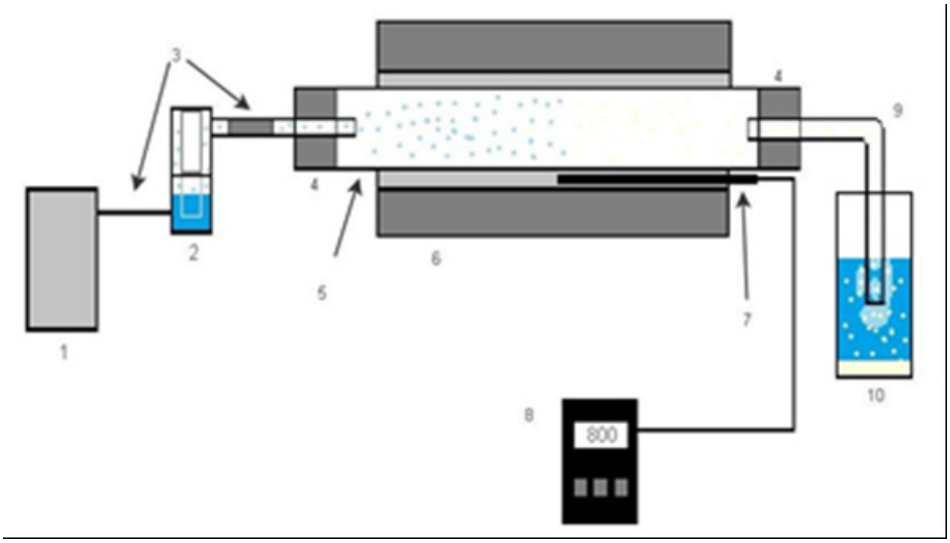

Fig. 1. Installation diagram for the spray pyrolysis: *1* – compressor, *2* – dispersant, *3* – pipes, *4* – rubber stopper, *5* – reactor (quartz tube), *6* – MTP–2M furnace, *7* – thermocouple, *8* – temperature controller, *9* – glass tube with a 90° rotation, *10* – a glass with distilled water for collecting the nanopowder

Where D_{hkl} – average particle size, Å, k – correction factor (for cubic and orthorhombic structure $k = 0.9$), λ - X-ray tube wavelength, θ - the position of the peak maximum, deg., β_{hkl} – intrinsic physical broadening of the diffraction maximum, rad.

The quantitative elemental composition of the synthesized samples was determined by the electron probe X-Ray microanalysis method (EPXMA, scanning electron microscope JEOL-6510LV with a Bruker energy dispersive microanalysis system). The particle size and morphology of the synthesized powders were determined according to transmission electron microscopy (TEM, CarlZeiss Libra-120 transmission electron microscope).

3. Results and discussion

According to the study [6], the stability and high-temperature luminescence properties of doped yttrium vanadates can be improved by a partial replacement of VO_4^{3-}-anions with isostructural anions of PO_4^{3-}. The presence of phosphate anions stabilizes the oxidation state of vanadium +5, which contributes to an increase in the luminescence yield. The doping of the anionic component of yttrium vanadate with smaller anions was accompanied by a decrease in the crystallite size under the same reaction conditions. It seems promising to carry out the synthesis of mixed crystals of yttrium vanadate-phosphate by doping yttrium phosphate with vanadate anions.

The first series of samples of yttrium vanadate phosphates of compositions $YV_{0.1}P_{0.9}O_4$ and $YV_{0.25}P_{0.75}O_4$, synthesized under the action of microwave radiation followed by ultrasonic dispersion, mainly contained the YPO_4 phase. However, reflections of vanadium oxides VO_2 and yttrium Y_2O_3 were revealed on diffractograms of $YV_{0.1}P_{0.9}O_4$ (Fig. 2). Changing the pH of the solution from 7 to 9 decreased the content of impurities in the synthesized powders of yttrium vanadate phosphate (Fig. 3). For $YV_{0.25}P_{0.75}O_4$ samples synthesized at pH 8, vanadium VO_2 and yttrium Y_2O_3 oxides were detected as the main impurity phases (Fig. 2). The reflections of these oxides were not differentiated in the diffractogram with an increase in the pH of the precursor solution from 8 to 9 (Fig. 3).

As a result of the synthesis of yttrium vanadate phosphate of the compositions $YV_{0.1}P_{0.9}O_4$ and $YV_{0.25}P_{0.75}O_4$ by spray pyrolysis without subsequent annealing, samples, containing a mixture of phases: yttrium oxide Y_2O_3, vanadium oxides VO_2, V_2O_5, and sodium vanadates were formed. The high background suggests a rather high degree of amorphism of the samples. The diffraction pattern of $YV_{0.1}P_{0.9}O_4$ sample synthesized by spray pyrolysis and annealed in a muffle furnace at 800 °C for 1 h (Fig. 4a) contained reflections of only yttrium phosphate. The small width of the reflections suggests a high degree of crystallinity of the sample. An increase in the annealing time up to 2 h (Fig.4b) was accompanied by an

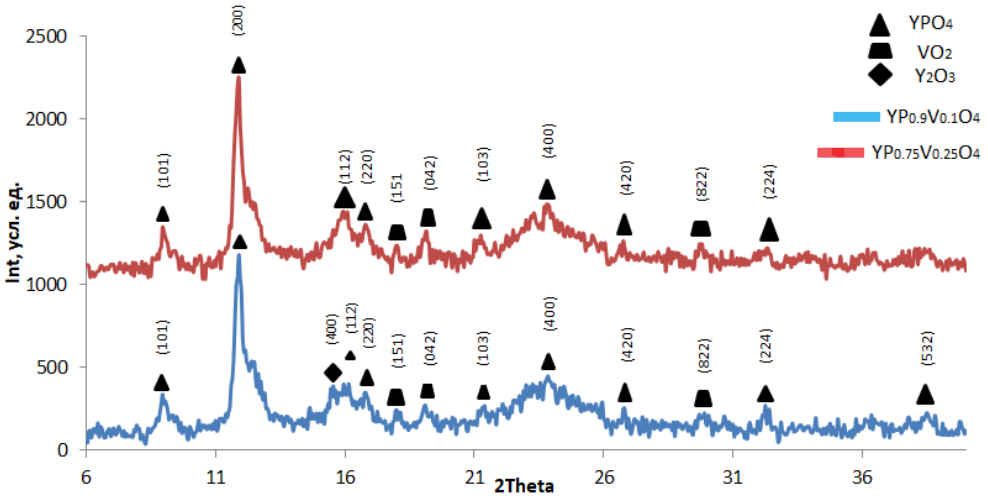

Fig. 2. X-ray diffractograms of the samples, microwave synthesis: a) $YV_{0.1}P_{0.9}O_4$ (pH = 7); b) $YV_{0.25}P_{0.75}O_4$ (pH = 8)

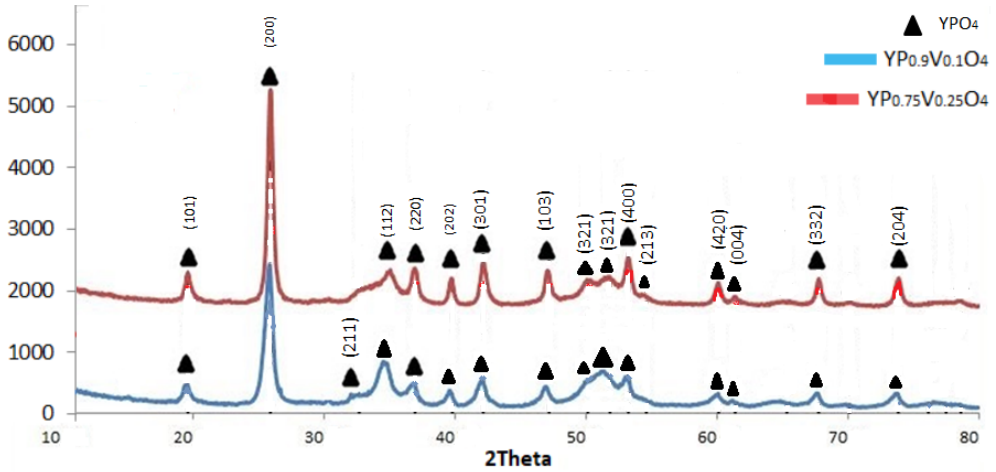

Fig. 3. X-ray diffractograms of $YV_{0.1}P_{0.9}O_4$ samples, microwave synthesis, pH = 9: a) $YV_{0.1}P_{0.9}O_4$; b) $YV_{0.25}P_{0.75}O_4$

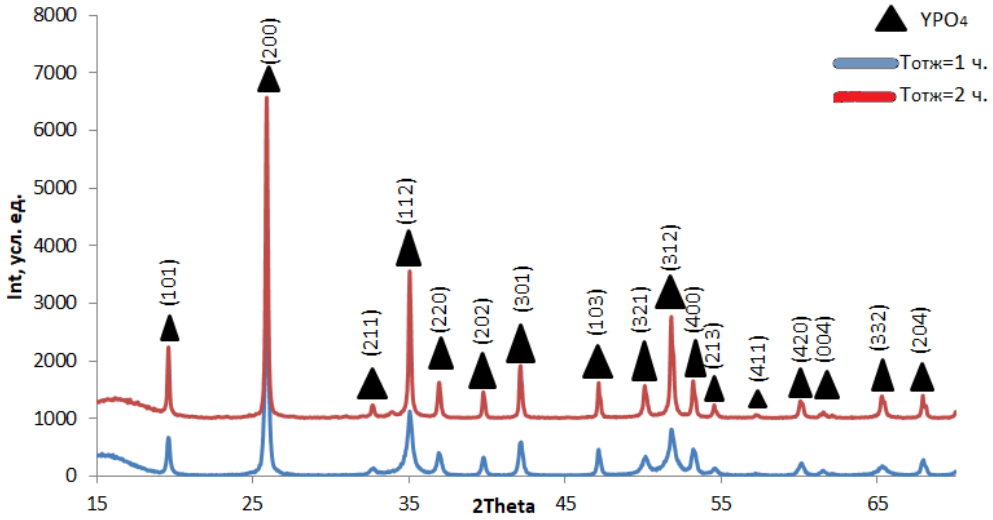

Fig. 4. X-ray diffractograms of $YV_{0.1}P_{0.9}O_4$ samples annealed: for a) 1 h and b) 2 h

increase in the intensity of reflections of YPO_4. The absence of vanadium-containing compounds in the diffractograms indicated the incorporation of vanadium in the form of vanadate ions into the crystal lattice of yttrium phosphate. The average CSR of particles of the $YV_{0.1}P_{0.9}O_4$ sample annealed for 1 h was 50 ± 2 nm (Table 1). Annealing for 2 h led to an increase in CSR up to 93±2 nm.

On the energy dispersive spectrum of the $YV_{0.25}P_{0.75}O_4$ sample synthesized by the coprecipitation method under the influence of microwave radiation at pH 7, only Y, P, and O signals were recorded (Fig. 5a). Apparently, the incorporation of V^{5+} ions into the YPO_4 lattice did not occur in a neutral solution, which was also confirmed by the XRD data regarding the presence of various vanadium oxides as impurities in these samples. An increase in the pH of the precursor solution to 8 allowed recording the vanadium signals in the energy dispersive spectrum (Fig. 5b). However, their intensity was low, the actual composition of the sample with respect to vanadium deviated by almost an order of magnitude from the nominal composition (Table. 2). Obviously, only partial incorporation of the introduced V^{5+} ions into the YPO_4 lattice occurred, the majority of vanadium ions were present in the form of impurity oxides. Only an

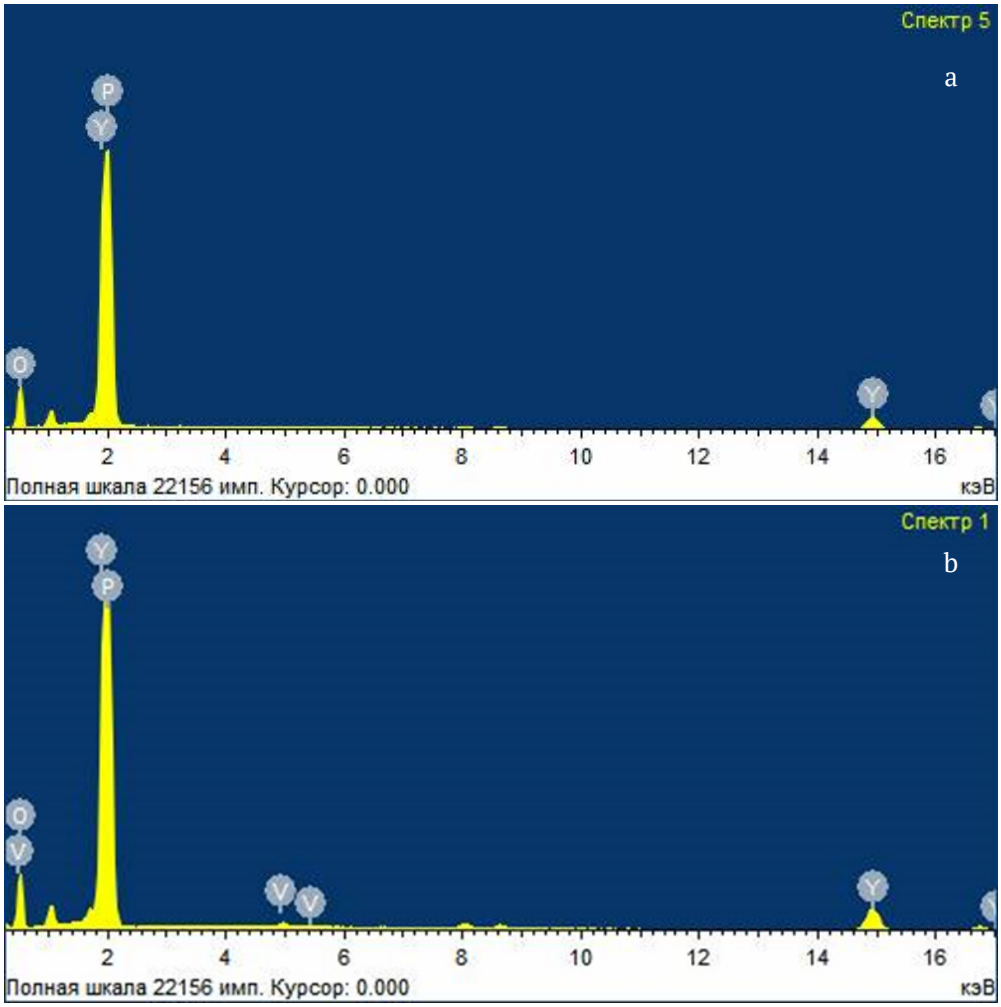

Fig. 5 Energy dispersion spectrum of samples: a) $YV_{0.25}P_{0.75}O_4$ (pH = 7); b) $YV_{0.25}P_{0.75}O_4$ (pH = 8)

Table 1. The radius of coherent scattering region of $YV_{0.1}P_{0.9}O_4$ samples with different annealing times

Sample	D_1	D_2	D_3	D_{cp}
$YV_{0.1}P_{0.9}O_4$ sample (t_{ann} = 1 h)	27±1	41±2	54±3	41±2
$YV_{0.1}P_{0.9}O_4$ sample (t_{ann} = 2 h)	99±2	73±2	106±2	93±2

Table 2. Data on the elemental composition of vanadate phosphates (pH = 7, pH = 8, pH = 9)

Nominal composition of samples	$YV_{0.1}P_{0.9}O_4$, pH = 7	$YV_{0.25}P_{0.75}O_4$, pH = 8	$YV_{0.25}P_{0.75}O_4$, pH = 9
Y (nominal), at%	16.6	16.6	16.6
Y (real), at%	11.94	12.2	16.18
V (nominal), atm. %	1.6	4.16	4.16
V (real), at%	0.1	0.24	5.97
P (nominal), atm. %	15	12.5	12.5
P (real), at%	13.74	13.78	11.42
O (nominal), at%	66.6	66.6	66.6
O (real), at%	74.22	73.77	64.31
Real composition of samples	$YV_{0.008}P_{1.15}O_{6.21}$	$YV_{0.02}P_{1.15}O_{6.17}$	$YV_{0.36}P_{0.68}O_{3.97}$

increase in pH to 9 allowed synthesizing samples, the real composition of which was close to the nominal (Table 2).

Morphologically, samples of yttrium vanadate phosphate synthesized by coprecipitation under the action of microwave radiation at pH = 8 were represented by large formations with an arbitrary shape up to 60 μm and smaller amorphised particles from 2 to 10 μm (Fig. 6).

According to TEM data (Fig. 7), $YV_{0.1}P_{0.9}O_4$ synthesized by spray pyrolysis and annealed at 800 °C for 1 h were faceted, had a size in the range of 25–100 nm, and weakly expressed agglomeration was observed (Fig. 7a). An increase

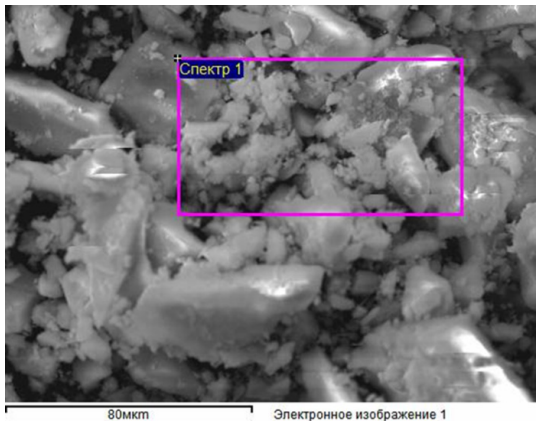

Fig. 6. SEM image of $YV_{0.25}P_{0.75}O_4$ powder synthesized by co-deposition under the action of microwave radiation (pH = 8)

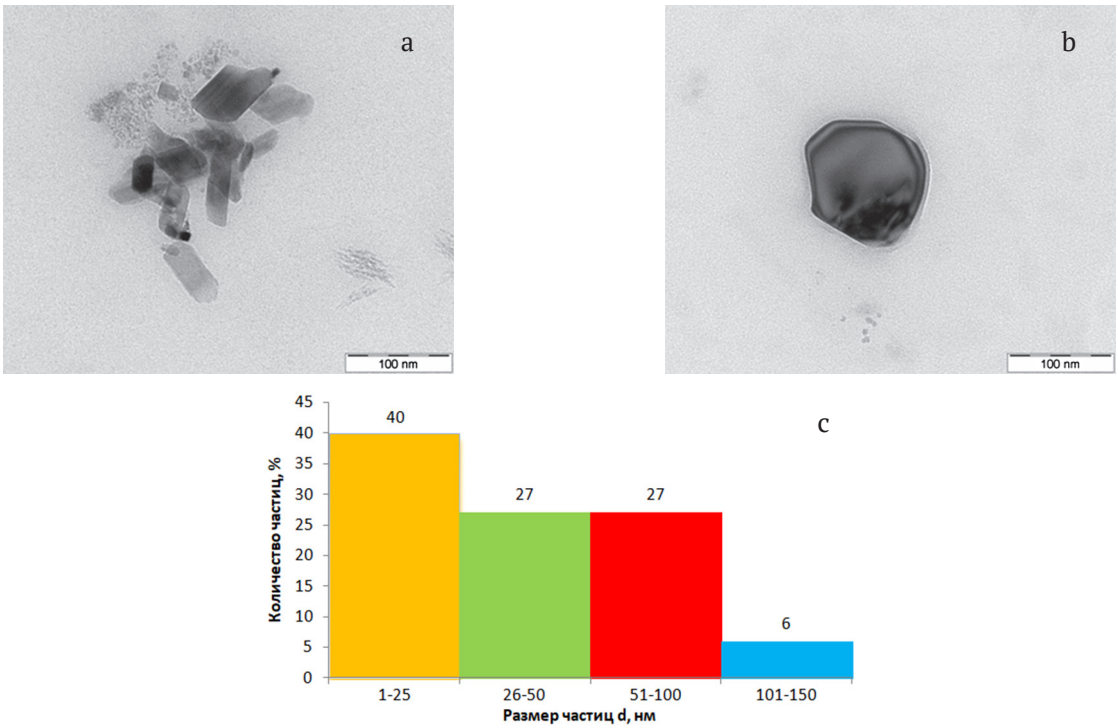

Fig. 7. TEM image of $YV_{0.1}P_{0.9}O_4$ sample in a gelatin layer: a) annealing at 800 °C, 1 h; b) annealing at 800 °C, 2 h; c) histogram of the particle size distribution of $YV_{0.1}P_{0.9}O_4$ sample

in the annealing time to 2 h promoted the formation of larger spherical particles (Fig. 7b).

4. Conclusions

It was established that the spray pyrolysis method with subsequent annealing allowed synthesizing nanopowders of yttrium vanadate phosphate of high chemical homogeneity with a size in the range of 20–100 nm with a low degree of agglomeration. The change of the annealing mode allowed controlling the size and shape of the particles.

The synthesis of $YV_xP_{1-x}O_4$ by the coprecipitation method under the action of microwave radiation due to the high sensitivity to pH of the precursor solution was accompanied by the presence of impurity phases in the samples. The maximum chemical homogeneity of yttrium vanadate phosphate powders was achieved at pH = 9. The particle size dispersion was large and was in the range of 2–80 μm.

References

1. Wu C., Wang Y., Jie W. Hydrothermal synthesis and luminescent properties of $LnPO_4$:Tb (Ln = La, Gd) phosphors under VUV excitation. *Journal of Alloys and Compounds*. 2007;436: 383–386. DOI: https://doi.org/10.1016/j.jallcom.2006.07.056

2. Huang J., Tang L., Chen N., Du G. Broadening the photoluminescence excitation spectral bandwidth of $YVO_4:Eu^{3+}$ nanoparticles via a novel core-shell and hybridization approach. *Materials*. 2019;12: 3830. DOI: https://doi.org/10.3390/ma12233830

3. Wu Y., Zhang Z., Suo H., Zhao X., Guo C. 808 nm light triggered up-conversion optical nano-thermometer $YPO_4:Nd^{3+}/Yb^{3+}/Er^{3+}$ based on FIR technology. *Journal of Luminescence*. 2019;214: 116478. DOI: https://doi.org/10.1016/j.jlumin.2019.116578

4. Xiu Z., Wu Y., Hao X., Li X., Zhang L. Uniform and well-dispersed Y_2O_3:Eu/YVO_4:Eu composite microspheres with high photoluminescence prepared by chemical corrosion approach. *Colloids Surf. A*. 2012;401(5): 68–73. DOI: https://doi.org/10.1016/j.colsurfa.2012.03.021

5. Vats B. G., Gupta S. K., Keskar M., Phatak R., Mukherjee S., Kannan S. The effect of vanadium substitution on photoluminescent properties of $KSrLa(PO_4)_x(VO_4)_{2x}:Eu^{3+}$ phosphors, a new variant of phosphovanadates. *New Journal of Chemistry*. 2016;40(2): 1799–1806. DOI: https://doi.org/10.1039/c5nj02951a

6. Riwotzki K., Haase M. Colloidal YVO_4:Eu and $YP_{0.95}V_{0.05}O_4$:Eu nanoparticles: luminescence and energy transfer processes. *The Journal of Physical Chemistry B*. 2001;105(51): 12709–12713. DOI: https://doi.org/10.1021/jp0113735

7. Wu C.-C., Chen K.-B., Lee C.-S., Chen T.-M., Cheng B.-M. Synthesis and VUV photoluminescence characterization of $(Y,Gd)(V,P)O_4:Eu^{3+}$ as a potential red-emitting PDP phosphor. *Chem. Mater*. 2007;19(13): 3278–3285. DOI: https://doi.org/10.1021/cm061042a

8. Shimomura Y., Kurushima T., Olivia R., Kijima N. Synthesis of $Y(P,V)O_4:Eu^{3+}$ red phosphor by spray pyrolysis without postheating. *The Japan Society of Applied*. 2005;44(3): 1356–1360. DOI: https://doi.org/10.1143/JJAP.44.1356

9. Lai H, Chen B., Xu W., Xie Y., Wang X., Di W. Fine particles $(Y,Gd)P_xV_{1-x}O_4:Eu^{3+}$ phosphor for PDP prepared by coprecipitation reaction. *Materials Letters*. 2006;60(11): 1341–1343. DOI: https://doi.org/10.1016/j.matlet.2005.11.051

10. Singh V., Takami S., Aoki N., Hojo D., Arita T., Adschiri T. Hydrothermal synthesis of luminescent $GdVO_4$:Eu nanoparticles with dispersibility in organic solvents. *Journal of Nanoparticle Research*. 2014;16(5): 2378. DOI: https://doi.org/10.1007/s11051-014-2378-2

11. Song W.-S., Kim Y.-S., Yang H. Hydrothermal synthesis of self-emitting $Y(V,P)O_4$ nanophosphors for fabrication of transparent blue-emitting display device. *Journal of Luminescence*. 2012;132(11): 1278–1284. DOI: https://doi.org/10.1016/j.jlumin.2012.01.015

12. Yu M., Lin J., Fu J., Han Y. Sol–gel fabrication, patterning and photoluminescent properties of $LaPO_4:Ce^{3+}$, Tb^{3+} nanocrystalline thin films. *Chemical Physics Letters*. 2003;5(1-2): 178–183. DOI: https://doi.org/10.1016/S0009-2614(03)00239-2

13. Raoufi D., Raoufi T. The effect of heat treatment on the physical properties of sol–gel derived ZnO thin films. *Applied Surface Science*. 2009;255(11): 5812–5817. DOI: https://doi.org/10.1016/j.apsusc.2009.01.010

14. Shao J., Yan J., Li X., Li S., Hu T. Novel fluorescent label based on $YVO_4:Bi^{3+}$, Eu^{3+} for latent fingerprint detection. *Dyes and Pigments*. 2019;160: 555–562. DOI: https://doi.org/10.1016/j.dyepig.2018.08.033

15. Dolinskaya Yu. A., Kolesnikov I. E., Kurochkin A. V., Man'shina A. A., Mikhailov M. D., Semencha A. V. Sol-Gel synthesis and luminescent properties of YVO_4: Eu nanoparticles. *Glass Physics and Chemistry*. 2013;39(3): 308–310. DOI: https://doi.org/10.1134/s1087659613030061

16. Tomina E. V., Sladkopevtsev B. V., Knurova M. V., Latyshev A.N., Mittova I. Y., Mittova V. O. Microwave synthesis and luminescence properties of $YVO_4:Eu^{3+}$. *Inorganic Materials*. 2016;52(5): 495–498. DOI: https://doi.org/10.1134/S0020168516050174

17. Tomina E. V., Mittova I. J., Burtseva N. A., Sladkopevtsev B. V. *Method for synthesis of yttrium*

orthovanadate-based phosphor: patent for invention No 2548089. The patent holder FGBOU VPO "Voronezh state University" No 2013133382/05; declared 12.11.2013; published. 20.05.2015.

18. Tomina E. V., Kurkin N. A., & Mal'tsev S. A. Microwave synthesis of yttrium orthoferrite doped with nickel. *Kondensirovannye sredy i mezhfaznye granitsy = Condensed Matter and Interphases*. 2019;21(2): 306–312. DOI: https://doi.org/10.17308/kcmf.2019.21/768 (In Russ., abstract in Eng.)

19. Huang J., Gao R., Lu Z., Qian D., Li W., Huang B., He X. Sol–gel preparation and photoluminescence enhancement of Li+ and Eu^{3+} co-doped YPO_4 nanophosphors. *Optical Materials*. 2010;32(9): 857–861. DOI: https://doi.org/10.1016/j.optmat.2009.12.011

20. Brandon D., Kaplan W. D. *Microstructural Characterization of Materials*. John Wiley & Sons Ltd; 1999. 409 p. DOI: https://doi.org/10.1002/9780470727133

Acknowledgements

The research results were partially obtained were obtained using the equipment of Shared Scientific Equipment Centre of Voronezh State University. URL: http://ckp.vsu.ru.

Conflict of interests

The authors declare that they have no known competing financial interests or personal relationships that could have influenced the work reported in this paper.

Information about the authors

Elena V. Tomina, DSc in Chemistry, Associate Professor, Voronezh State University, Voronezh State University of Forestry and Technologies named after G. F. Morozov, Voronezh, Russian Federation; e-mail: tomina-e-v@yandex.ru. ORCID iD: https://orcid.org/0000-0002-5222-0756.

Dmitry A. Lastochkin, 1st year Master's degree student Voronezh State University, Voronezh, Russian Federation; e-mail: lastochkin.d1998@mail.ru

Sergey A. Maltsev, 2nd year Master's degree student, Voronezh State University, Voronezh, Russian Federation; e-mail: sergmaltsev97@mail.ru

All authors have read and approved the final manuscript.

Translated by Valentina Mittova
Edited and proofread by Simon Cox

Condensed Matter and Interphases
(Kondensirovannye sredy i mezhfaznye granitsy)

Short communications

DOI: https://doi.org/10.17308/kcmf.2020.22/3121
Received 01 December 2020
Accepted 15 December 2020
Published online 25 December 2020

ISSN 1606-867X
eISSN 2687-0711

Microwave Synthesis of $CaTiO_3$ Nanoparticles by the Sol-Gel Method

© 2020 V. F. Kostryukov✉, A. E. Igonina

Voronezh State University,
1 Universitetskaya pl., Voronezh 394018, Russian Federation

Abstract

A technique for the microwave-activated synthesis of calcium titanate nanopowder was proposed. The microwave effect used in the synthesis of $CaTiO_3$ samples when using sodium carbonate as a precipitant allowed obtaining a chemically homogeneous nanopowder with a significant reduction of the process time.

Keywords: sol-gel, microwave synthesis, calcium titanate, nanoparticles.

For citation: V. F. Kostryukov, A. E. Igonina. Microwave synthesis of $CaTiO_3$ nanoparticles by the sol-gel method. *Kondensirovannye sredy i mezhfaznye granitsy = Condensed Matter and Interphases*. 2020; 22(4): 504–506. DOI: https://doi.org/10.17308/kcmf.2020.22/3121.

Для цитирования: Кострюков В. Ф., Игонина А. Е. Микроволновый синтез наночастиц $CaTiO_3$ золь-гель методом. *Конденсированные среды и межфазные границы*. 2020; 22(4): 504–506. DOI: https://doi.org/10.17308/kcmf.2020.22/3121.

1. Introduction

In recent years, the development of methods for obtaining and studying the properties of nanoparticles and nanostructured materials of various chemical composition, structure, and morphology became a priority task in materials science.

Oxide compounds with a perovskite structure are widely used in the manufacture of solid oxide fuel cells, catalysts, magnetic materials, chemical sensors, and electrodes [1, 2].

Calcium titanate is known as a promising material with ferroelectric and paraelectric properties; it is used as an active element in piezoelectric transducers, optical modulators, ferroelectric memory devices, capacitors with a high dielectric constant, microwave devices, and photocatalysts [3].

Sol-gel technology has already proved to be efficient methods for the synthesis of powders of various compounds with particles of the nanometre range [4, 5].

✉ Viktor F. Kostryukov, e-mail: vc@cnem.vsu.ru

The aim of this study was to establish the effect of microwave exposure on the synthesis of $CaTiO_3$ nanoparticles by the sol-gel method.

2. Experimental

The following precursors were used in this study: calcium nitrate crystallohydrate $Ca(NO_3)_2 \cdot 5H_2O$ (analytical reagent grade CAS 10035-06-0), titanium chloride $TiCl_4$ (special purity grade TU 6-09-4471-77), sodium carbonate Na_2CO_3 (reagent grade GOST 4201-79).

The synthesis of calcium titanate nanoparticles was carried out in two modes - in the presence and absence of microwave radiation. The rest of the process parameters were kept the same.

During the first stage, the initial solutions were prepared: aqueous solution $Ca(NO_3)_2$ and alcoholic solution $TiCl_4$. Then these solutions were mixed, boiled for a certain time, and cooled to room temperature. This process was accompanied by the formation of TiO_2. During the same stage, in the second series of experiments, microwave exposure was carried out (P_{max} = 700 W, operating frequency

2450 MHz). The boiling time was 5 min in the presence of microwave exposure and 20 min in the absence of microwave exposure.

Sodium carbonate was used as a precipitant in an amount sufficient for the complete precipitation of the components. The gel formed by this method was filtered, dried in air, and then annealed for one hour at a temperature of 750 °C. The following reactions took place:

$$Ca(NO_3)_2 + Na_2CO_3 = CaCO_3 + 2NaNO_3 \quad (1)$$

$$CaCO_3 = CaO + CO_2 \quad (2)$$

$$CaO + TiO_2 = CaTiO_3 \quad (3)$$

For the investigation of the phase composition of the samples, we used the method of X-ray phase analysis, DRON-3 X-ray diffractometer with a Cu anode (λ = 0.71075 nm). The scanning was performed within an angle range of 2θ = 0–80° with a step of 0.1. Phases were identified using [6, 7].

3. Results and discussion

Thee diffraction patterns of the samples synthesized without (a) and in the presence (b) of microwave exposure are shown in Fig. 1.

For the sample obtained without microwave exposure, distinct peaks of unreacted starting substances: titanium and calcium oxides were observed. Reflexes corresponding to the target product – $CaTiO_3$ were also present, but they

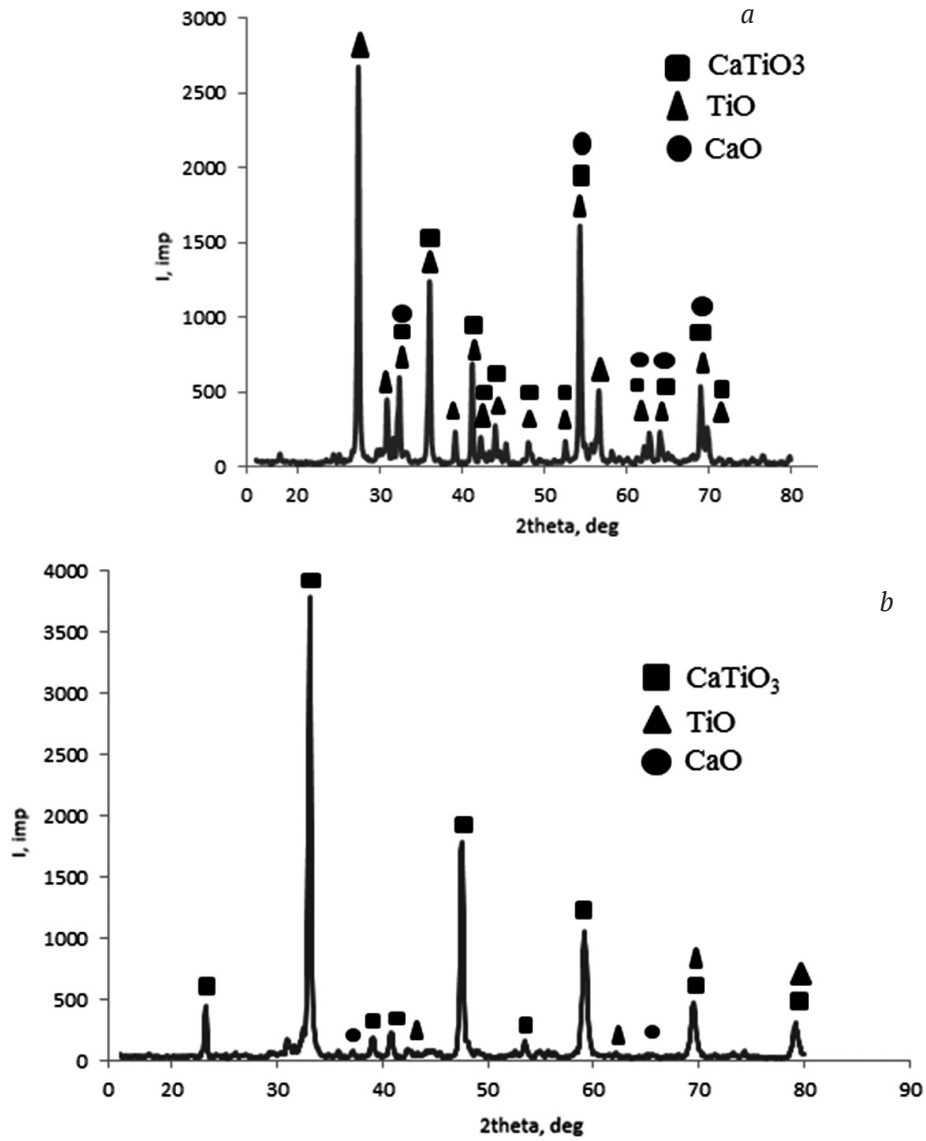

Fig. 1. Diffraction pattern of calcium titanate powder obtained in the absence (a) and presence (b) of microwave exposure

were not so distinct. This means that when the synthesis was carried out in the absence of microwave exposure, it was not possible to achieve the required degree of interaction between the reagents.

The diffractogram for the sample synthesized under the action of microwave radiation (Fig. 1b) was radically different. The peaks corresponding to calcium titanate were predominant and distinct, while the peaks related to the starting substances were present in small amounts and have low intensity, especially for calcium oxide.

4. Conclusion

Thus, the use of microwave exposure in the process of synthesis of nanocrystalline calcium titanate allows solving two problems at once: in the case of microwave synthesis, the powder had not only more homogeneous in composition, with a predominance of the required compound, but also significant intensification of the process, consisting in a decrease in the synthesis time was observed.

Acknowledgements

The results of the research were obtained using the Centre for the Collective Use of Scientific Equipment of Voronezh State University. URL:http://ckp.vsu.ru

Conflict of interests

The authors declare that they have no known competing financial interests or personal relationships that could have influenced the work reported in this paper.

References

1. Zhang Q., Saito F. Effect of Fe_2O_3 crystallite size on its mechanochemical reaction with La_2O_3 to form $LaFeO_3$. *Journal of Materials Science*. 2001;36(9): 2287–2290. DOI: https://doi.org/10.1023/a:1017520806922

2. Bayraktar D., Clemens F., Diethelm S., et al. Production and properties of substituted $LaFeO_3$-perovskite tubular membranes for partial oxidation of methane to syngas. *Journal of the European Ceramic Society*. 2007;27(6): 2455–2461. DOI: https://doi.org/10.1016/j.jeurceramsoc.2006.10.004

3. Reznichenko V. A., Averin V. V., Olyunina T. V. Titanaty. *Nauchnye osnovy, tekhnologiya, proizvodstvo* [Titanates. Scientific foundations, technology, production]. Moscow: Nauka Publ.; 2010. 72 p. (In Russ.)

4. Suzdalev I. P. *Nanotekhnologiya: fiziko-khimiya nanoklasterov, nanostruktur i nanomaterialov* [Nanotechnology: physical chemistry of nanoclusters, nanostructures and nanomaterials]. Moscow: KomKniga Publ.; 2006. 592 p. (In Russ.)

5. Gusev A. I. *Nanomaterialy, nanostruktury, nanotekhnologii* [Nanomaterials, nanostructures, nanotechnology]. Moscow: Fizmatlit Publ.; 2007. 416 p.

6. *International Center for Diffraction Data*.

7. *X-ray diffraction date cards, ASTM*.

Information about the authors

Victor F. Kostryukov, DSc in Chemistry, Associate Professor, Associate Professor at the Department of Materials Science and the Industry of Nanosystems, Voronezh State University, Voronezh, Russian Federation; e-mail: vc@chem.vsu.ru. ORCID iD: https://orcid.org/0000-0001-5753-5653.

Anastasia E. Igonina, student at the Department of Materials Science and thr Industry of Nanosystems, Voronezh State University, Voronezh, Russian Federation; e-mail: nstj.gnn@rambler.ru.

All authors read and approved the final manuscript.

Translated by Valentina Mittova
Edited and proofread by Simon Cox